

1. Report No. SWUTC/16/600451-00053-1		2. Government Accession No.		3. Recipient's Catalog No.	
4. Title and Subtitle Modeling Deformation of Freezing Concrete: Towards the Identification of D-cracking Susceptible Aggregates and Construction of all Concrete LNG Tanks				5. Report Date December 2016	
				6. Performing Organization Code	
7. Author(s) Syeda Farhana Rahman				8. Performing Organization Report No. Report 600451-00053-1	
9. Performing Organization Name and Address Texas A&M Transportation Institute Texas A&M University System College Station, Texas 77843-3135				10. Work Unit No. (TRAIS)	
				11. Contract or Grant No. DTRT12-G-UTC06	
12. Sponsoring Agency Name and Address Southwest Region University Transportation Center Texas A&M Transportation Institute Texas A&M University System College Station, Texas 77843-3135				13. Type of Report and Period Covered	
				14. Sponsoring Agency Code	
15. Supplementary Notes Supported by a grant from the U.S. Department of Transportation, University Transportation Centers Program and general revenues from the State of Texas					
16. Abstract <p>For many decades, degradation of concrete by freezing actions has been a primary interest of research for civil engineers. Past studies mostly relied on expensive and time-consuming experimental or semi-empirical investigations to identify the source of damage that is attributable to substandard aggregates, inadequate entrained air content, highly porous mortar or cement matrix, and use of deicing salts. Theoretical works developed in recent years do not incorporate all these factors in one single model. Very recently, concrete has gained widespread popularity as a cheap alternative to traditional material utilized for containing liquefied natural gas (LNG). Most studies documenting concrete behavior at cryogenic temperatures are obscure. Therefore, poroelastic theory, capable of incorporating aggregate and mortar properties, pore solution characteristics, air void spacing, and environmental exposure has been utilized to model damage triggering stresses and strain in concrete used for two purposes: 1) concrete pavement exposed to freezing and thawing cycles, and 2) concrete walled tanks containing LNG. The solid-liquid phase transformation equilibrium has been redeveloped to demonstrate the effect of pore solution speciation and disjoining pressure on the deformation of freezing concrete.</p> <p>The modeled trends are in good agreement with experimental results obtained from literature. It has been found that the damage initiating tensile stresses, exhibited at the aggregate-matrix boundary for both the air-entrained and non-air-entrained concrete, can be exacerbated by the Mandel-Cryer effect induced by the delayed relaxation of the pore pressure from the aggregate center. The model suggests that high-porosity, low-permeability aggregates are the most vulnerable to D-cracking. Concrete with low-porosity, low-permeability mortar matrix, typical of mortar containing supplementary cementitious materials and/or low water to cement ratio, can withstand freezing deformation even with a spacing factor larger than the recommended value. In addition, thermodynamic analysis shows that the disjoining force favors crystal growth, while the dissolved ions suppress the freezing point but are still capable of building high hydraulic pressure in the pore network. We believe that implementation of these models will help practitioners select appropriate combinations and proportions of concrete mixture constituents to build safe, economic, and durable concrete structures.</p>					
17. Key Words Concrete, Deformation, LNG Tanks, Freeze Thaw Cycles			18. Distribution Statement No restrictions. This document is available to the public through NTIS: National Technical Information Service 5285 Port Royal Road Springfield, Virginia 22161		
19. Security Classif.(of this report) Unclassified		20. Security Classif.(of this page) Unclassified		21. No. of Pages 187	22. Price

MODELING DEFORMATION OF FREEZING CONCRETE: TOWARDS THE  
IDENTIFICATION OF D-CRACKING SUSCEPTIBLE AGGREGATES AND  
CONSTRUCTION OF ALL CONCRETE LNG TANKS

A Dissertation

by

SYEDA FARHANA RAHMAN

Submitted to the Office of Graduate and Professional Studies of  
Texas A&M University  
in partial fulfillment of the requirements for the degree of

DOCTOR OF PHILOSOPHY

Chair of Committee,	Zachary Grasley
Co-Chair of Committee,	Eyad Masad
Committee Members,	Alan Freed
	Dan Zollinger
Head of Department,	Robin Autenrieth

December 2016

Major Subject: Civil Engineering

Copyright 2016 Syeda Farhana Rahman

## ABSTRACT

For many decades, degradation of concrete by freezing actions has been a primary interest of research for civil engineers. Past studies mostly relied on expensive and time-consuming experimental or semi-empirical investigations to identify the source of damage that is attributable to substandard aggregates, inadequate entrained air content, highly porous mortar or cement matrix, and use of deicing salts. Theoretical works developed in recent years do not incorporate all these factors in one single model. Very recently, concrete has gained widespread popularity as a cheap alternative to traditional material utilized for containing liquefied natural gas (LNG). Most studies documenting concrete behavior at cryogenic temperatures are obscure. Therefore, poroelastic theory, capable of incorporating aggregate and mortar properties, pore solution characteristics, air void spacing, and environmental exposure has been utilized to model damage triggering stresses and strain in concrete used for two purposes: 1) concrete pavement exposed to freezing and thawing cycles, and 2) concrete walled tanks containing LNG. The solid-liquid phase transformation equilibrium has been redeveloped to demonstrate the effect of pore solution speciation and disjoining pressure on the deformation of freezing concrete.

The modeled trends are in good agreement with experimental results obtained from literature. It has been found that the damage initiating tensile stresses, exhibited at the aggregate-matrix boundary for both the air-entrained and non-air-entrained concrete, can be exacerbated by the Mandel-Cryer effect induced by the delayed relaxation of the

pore pressure from the aggregate center. The model suggests that high-porosity, low-permeability aggregates are the most vulnerable to D-cracking. Concrete with low-porosity, low-permeability mortar matrix, typical of mortar containing supplementary cementitious materials and/or low water to cement ratio, can withstand freezing deformation even with a spacing factor larger than the recommended value. In addition, thermodynamic analysis shows that the disjoining force favors crystal growth, while the dissolved ions suppress the freezing point but are still capable of building high hydraulic pressure in the pore network. We believe that implementation of these models will help practitioners select appropriate combinations and proportions of concrete mixture constituents to build safe, economic, and durable concrete structures.

## DEDICATION

To my parents, for their selfless support and love

and

to Rezwan, for showing up at the DFW airport and still not realizing the mistake he

made

## ACKNOWLEDGEMENTS

No word is sufficient to express my gratitude to Dr. Grasley for the things he did for me. Thank you Dr. Grasley for believing in me and showing me your support from my very first day at Texas A&M University. Thank you for making sure that I got received financial assistance each and every day. Thank you also for all the recommendations you have given me and helping me get numerous fellowships. Thank you for being my mentor and my advisor, and for guiding me with your creative ideas of solving problems. Without your guidance, this dissertation would not be possible.

I would also like to acknowledge my co-chair Dr. Masad, and the committee members, Dr. Freed and Dr. Zollinger for all their time and support. I want to thank Dr. Epps Martin and Dr. Gharaibeh for helping me with financial support.

I am grateful to all my friends and family for supporting me through each and every step of this journey. I want to especially thank my parents for letting me follow my own path and never forcing me into anything. A special thank you to my mother for supporting me every way possible regardless of going through various hardships. She taught me the value of education and always made sure to give me the best education possible. And, Rezwan, without you and your support I don't think it would be possible for me to finish my PhD. Thank you for helping me improve my English and always encouraging me to do better. And, thank you for putting up with me through all the ups and downs.

I would also like to acknowledge the U.S. Department of Transportation,  
University Transportation Centers Program to the Southwest Region University  
Transportation Center and Qatar National Research Fund project NPRP 4 - 410 -2 – 156  
for their financial support.

## NOMENCLATURE

<b>Abbreviation/ Symbol</b>	<b>Description</b>	<b>Unit</b>
ASTM	American Society for Testing and Material	---
ACI	American Concrete Institute	---
SCM	Supplementary cementitious material	---
CTE	Coefficient of thermal expansion	---
LNG	Liquefied natural gas	---
ITZ	Interfacial transition zone	---
FHWA	Federal Highway Administration	---
Superscript $i$	Individual species	---
Superscript $L$	Mixture of liquid or solution	---
Superscript $C$	Mixture of crystal	---
Superscript $G$	Mixture of gas	---
Superscript $L-H_2O$	Liquid water in the solution mixture	---
Superscript $L-i$	Individual species in the solution mixture	---
Superscript $L-S$	Solute in the solution mixture	---
Superscript $C-H_2O$	Liquid water in the crystal mixture	---
Superscript $C-i$	Individual species in the crystal mixture	---
Superscript $a$	Aggregate	---

Superscript $p$	Cement matrix or mortar	---
Superscript $J$	Phase ( $L$ , $C$ , or $G$ ) present in the pore space	---
Superscript $d$	Disjoining pressure	---
Superscript $p-L$	Pore liquid in the cement or mortar matrix	---
Superscript $a-L$	Pore liquid in the aggregate	---
Subscript $app$	Applied stress/temperature/pressure	---
Subscript $atm$	Atmospheric temperature/pressure	---
$\bar{S}$	Current molar entropy	J/mol/K
$\bar{S}_0$	Molar entropy at the reference state	J/mol/K
$\bar{S}_{0^*}$	Molar entropy of the pure component at the reference	J/mol/K
$\mu$	Molar chemical potential	J/mol
$\theta$	Current temperature	K or °C
$\theta_m$	Melting temperature or reference temperature	K or °C
$\Delta\theta = \theta_m - \theta$	Change in temperature measures with respect to the melting temperature	K or °C
$\bar{V}$	Current molar volume	m <sup>3</sup> /mol
$\bar{V}_0$	Molar volume at the reference state	m <sup>3</sup> /mol
$\bar{V}_{0-n}^C$	Net molar volume of the ice crystal	m <sup>3</sup> /mol
$\Delta\bar{S}$	Change in molar entropy due to fusion	J/mol/K

$x$	Molar fraction of the dissolved species in the liquid mixture	mol/mol
$\bar{N}$	Molar fraction	mol/mol
$N^i$	Current number of moles of species $i$	mol
$N$	Total number of moles of the mixture	mol
$\beta$	Stoichiometric coefficient related to the reaction of crystallization	---
$B = \sum_{i=1}^n \beta^i$	Summation of stoichiometric coefficients other than H <sub>2</sub> O	---
$a$	Activity	---
$\underline{\underline{T}}^i$	partial Cauchy stress tensor of species $I$	MPa
$\underline{\underline{T}}$	Total Cauchy stress tensor	MPa
$\underline{\underline{\varepsilon}}$	Infinitesimal strain tensor	m/m
$\in$	Current infinitesimal volumetric strain	m/m
$\underline{\underline{s}}$	Deviatoric stress tensor	MPa
$\underline{\underline{e}}$	Current infinitesimal deviatoric strain tensor	m/m
$\sigma$	Mean stress	MPa
$\sigma_0$	Mean stress at the reference state	MPa
$\sigma_r$	Principal stress in the radial direction	MPa
$\sigma_t$	Principal stress in the tangential direction	MPa

$\sigma_{x,y,z}$	Principal stresses in the $x$ , $y$ , and $z$ directions	MPa
$\varepsilon_r$	Radial strain	m/m
$\varepsilon_t$	Tangential strain	m/m
$\varepsilon_{kk}$	bulk strain	m/m
$\varepsilon_f$	Free strain	m/m
$p$	Pressure	MPa
$p_0$	Pressure at the reference state	MPa
$\alpha$	Linear coefficient of thermal expansion	$^{\circ}\text{C}^{-1}$
$K$	Bulk modulus	MPa
$G$	Shear modulus	MPa
$K_s$	Bulk modulus of the solid skeleton	MPa
$G_s$	Shear modulus of the solid skeleton	MPa
$\Sigma_m$	Melting entropy	MPa/ $^{\circ}\text{C}$
$\rho$	Density	$\text{kg}/\text{m}^3$
$\nu$	Poisson's ratio	---
$\kappa$	Thermal diffusivity	$\text{m}^2 / \text{s}$
$\wp$	Thermal conductivity	W/m/K
$C_p$	Specific heat capacity	J/kg/K
$k$	Intrinsic permeability	$\text{m}^2$
$\eta$	Viscosity	Pas

$m_w$	Total mass of water currently present in all forms (both liquid and solid)	kg
$R$	Ideal gas constant	J/mol/K
$\phi$	Current porosity of the porous material	---
$\phi_0$	Porosity of the porous material at the reference state	---
$b$	Biot's coefficient	---
$M$	Biot's Modulus	MPa
$S$	Degree of saturation	---
$\varpi$	Coefficient related to the thermal expansion of the pore space	$^{\circ}\text{C}^{-1}$
$R_i$	Radius of the spherical aggregate core	m
$R_o$	Outer radius of the mortar shell	m
$L$	Air void spacing	m
$u$	Deformation	m
$r$	Radial distance	m
$t$	Time	s
$C$	Integration constant	---
$m$	Shape factor relating the pore size distribution	---
$R_*$	Pore radius related to the characteristic cooling	$\mu\text{m}$
$\gamma_{CL}$	water/ice interfacial energy	J/m <sup>2</sup>

$\Lambda(S^L)$	Reduction factor accounting for the change in effective pore volume due to the change in liquid saturation	---
$h_r$	Relative humidity	%
$r_{GL}$	Current circumferentially averaged radius of curvature of the gas-liquid interface	m
$\gamma_{GL}$	Surface energy of the gas-liquid interface	J/m <sup>2</sup>
$\delta$	Thickness of the thin layer of the unfrozen pore solution between the crystal and the pore wall	Å or nm
$F$	Overall Helmholtz free energy	J
$F_{sk}$	Helmholtz free energy of the skeleton	J
$\Sigma_{sk}$	Entropy of the skeleton	MPa/°C

# TABLE OF CONTENTS

	Page
ABSTRACT .....	ii
DEDICATION .....	iv
ACKNOWLEDGEMENTS .....	v
NOMENCLATURE.....	vii
TABLE OF CONTENTS .....	xiii
LIST OF FIGURES.....	xvi
LIST OF TABLES .....	xxi
1 INTRODUCTION.....	1
1.1 Problem statement.....	2
1.1.1 Overly simplistic design .....	2
1.1.2 Inability to predict freezing deformation due to pore solution speciation .....	4
1.1.3 Erroneous modeling due to the omission of disjoining pressure .....	4
1.1.4 Inability to utilize concrete for primary containment of LNG.....	5
1.2 Research scope and objectives.....	6
1.3 Research outline.....	9
2 BACKGROUND INFORMATION.....	13
2.1 Effect of aggregates on frost damage .....	13
2.2 Role of air voids in mitigating frost damage .....	15
2.3 Concrete walled LNG tanks.....	17
3 MODELING FREEZING POROUS MEDIA .....	21
3.1 Liquid solid phase transition.....	21
3.2 Governing equations .....	32
3.3 Poroelasticity .....	33
3.4 Summary .....	36
4 IDENTIFYING D-CRACKING SUSCEPTIBLE AGGREGATES.....	39

4.1	Model.....	39
4.1.1	Elastic material .....	40
4.1.2	Unsaturated poroelastic materials.....	43
4.1.3	Air entrained versus non-air-entrained concrete.....	45
4.2	Damage mechanism.....	48
4.3	Effect of crystal saturation on permeability.....	62
4.4	Results and discussions.....	63
4.4.1	Effect of aggregate pore structure.....	65
4.4.2	Effect of aggregate size.....	68
4.4.3	Effect of paste or mortar pore structure.....	70
4.4.4	Effect of coefficient of thermal expansion (CTE) .....	71
4.4.5	Effect of cooling rate .....	74
4.5	Summary.....	76
5	DETERMINING OPTIMUM AIR VOID PARAMETER.....	78
5.1	Results and discussion .....	79
5.1.1	Effect of air entrainment.....	83
5.1.2	Effect of light weight aggregate on freezing stresses with variable spacing factors .....	86
5.1.3	Effect of SCM and low w/c on freezing stress with variable bubble spacing factor.....	87
5.1.4	Effect of environmental exposure.....	91
5.2	Summary.....	92
6	EVALUATING CONCRETE COMPATIBILITY FOR THE CONSTRUCTION OF LNG TANKS .....	95
6.1	Deformation of fully and partially saturated concrete.....	95
6.2	Concrete tank subjected to cryogenic temperatures .....	98
6.2.1	Pore pressure in the fully saturated concrete .....	100
6.2.2	Pore pressure in the partially saturated concrete .....	102
6.3	Results and discussions.....	102
6.3.1	Effect of cooling rate .....	106
6.3.2	Effect of moisture content.....	111
6.3.3	Effect of cryogenic swelling.....	116
6.4	Summary.....	120
7	PREDICTING SHIFTS IN FREEZING POINT DUE TO LIQUID CONFINEMENT AND PORE SOLUTION SPECIATION .....	121
7.1	Effect of dissolved species.....	121
7.2	Disjoining pressure and its contribution to crystal growth.....	128
7.3	Comparison with literature data.....	132
7.4	Summary.....	136

8	CONCLUSIONS.....	137
8.1	Identifying deleterious aggregates susceptible to frost damage .....	138
8.2	Determining optimum air void spacing specific to a concrete mixture design and environmental exposure.....	140
8.3	Analyzing the effect of pore solution speciation and liquid confinement on the solid-liquid phase transition.....	142
8.4	Evaluating concrete compatibility for the construction of LNG tanks	144
	REFERENCES.....	147
	APPENDIX A .....	158
	APPENDIX B .....	159
	Thermodynamics of partially saturated freezing concrete .....	159

## LIST OF FIGURES

	Page
Figure 1. Flowchart for the performed research tasks.....	12
Figure 2. Geometry of the proposed model representing a coarse aggregate core of radius $R_i$ embedded in a cement paste or mortar matrix shell of outer radius $R_o$ . In case of air-entrained concrete, uniformly distributed air bubbles are considered with a spacing of $L$ . .....	40
Figure 3. Pore liquid pressure (a) and (b), bulk strain (c), and tangential stress (d) distribution in non-air-entrained concrete due to a step change of temperature to $-15^\circ\text{C}$ . Center exhibits over pressurization (b) and subsequent expansion (c) due to the Mandel-Cryer effect. As a result, delayed tensile tangential stress (d) is developed at the contracting aggregate boundary.....	55
Figure 4. Pore liquid pressure (a) and (b), bulk strain (c), and tangential stress (d) distribution in air-entrained concrete due to a step change of temperature to $-15^\circ\text{C}$ . As the drained boundary contracts (c), the center over pressurizes itself (b) and exhibits delayed expansion (c) and subsequently exerts peak tensile tangential stress at the boundary (d). However, with time, as the equilibrium is established and the pore water depressurizes, the air-entrained concrete contracts (c) as opposed to the non-air-entrained concrete (Figure 3 (c)). .....	56
Figure 5. Pore liquid pressure (a) & (b), bulk strain (c), and tangential stress (d) distribution for non-air-entrained concrete for a gradual change of temperature at a rate of $-1^\circ\text{C/hr}$ . Peak tensile stress (short dashed line in (d)) is developed at the aggregate boundary due to the Mandel-Cryer effect induced by over pressurization (long dashed line in (b)) and delayed expansion of the center (long dashed line in (a)).....	60
Figure 6. Pore liquid pressure (a) & (b), bulk strain (c), and tangential stress (d) distribution for air-entrained concrete for a gradual change of temperature at a rate of $-1^\circ\text{C/hr}$ . Peak tensile stress (dotted line and solid line in (d)) is developed at the matrix due to the Mandel-Cryer effect induced by over pressurization (long dashed line in (b)) and delayed expansion of the center (long dashed line in (c)) which is analogous to the behavior of non-air-entrained concrete. For air-entrained concrete, water can reach the escape boundary faster than the non-air-entrained concrete because of the air-void system. Consequently, air-entrained matrix shrinks more than the non-air-	

entrained matrix, and causes tensile stress in the mortar that may initiate cracks in the interfacial transition zone (ITZ) over successive freeze-thaw cycles. ....	61
Figure 7. Effect of unsaturated intrinsic permeability on the tangential stress at the aggregate boundary.....	63
Figure 8. Effect of aggregate pore properties on the peak tensile stress. At a temperature above -5 °C, due to Mandel-Cryer effect, high-porosity, low-permeability aggregates exhibit peak tensile tangential stress at the boundary. Whereas, low-porosity and/or high-permeability aggregates do not show such peak stress because high permeability allows quick pore pressure relaxation to the escape boundary, and low-porosity reduces the impact of the hydraulic pressure.....	67
Figure 9. Effect of aggregate maximum size on the peak tensile stress. Reduction in aggregate size from 0.0254 m (1 inches) to 0.0127 m (0.5 inches) proves beneficial for a high-porosity, low-permeability aggregate and likely reduces damage propensity, which agrees well with the previous empirical findings [11].....	69
Figure 10. Effect of matrix pore properties on the maximum tensile stress in the ITZ for air-entrained concrete. Tensile tangential stress decreases if the matrix pore size increases, and porosity decreases. ....	72
Figure 11. Effect of pore characteristics on liquid saturation. Large pores with uniform pore size distribution reduce the amount of expelled water. The closer $m^p$ is to 1, the more narrow-banded the pore radius distribution. In other words, pore water freezes over a narrow range of temperature when $m^p$ approaches unity.....	73
Figure 12. Effect of different CTE on the peak tensile tangential stress in the ITZ for air-entrained concrete. High difference in the CTE between the aggregate and the matrix may cause high tangential stress in the ITZ, with the stress magnitude progressively increasing as temperature decreases below the melting point.....	74
Figure 13. Effect of cooling rate on the bulk strain of concrete cooled to -50 °C. The higher the cooling rate, the higher the initial swelling. However, at very low temperatures, after which hydraulic pore pressure dissipates completely, constant contraction caused by the thermal contraction (non-air-entrained concrete) is observed that is solely dependent on material properties, and not the cooling rate. In the air-entrained concrete this contraction is more enhanced by the presence of cryo pumps or air voids. ....	76

Figure 14. Modeled pore pressure ( $p^L$ ), bulk strain ( $\varepsilon_{kk}$ ), and tangential stresses ( $\sigma_t$ ) for non-air-entrained concrete (mixture design 1 (MD1)), and air-entrained concrete with 0.8 mm (MD2) and 0.2 mm (MD3) spacing factor. Superscripts $a$ and $p$ denote aggregate and mortar matrix, respectively. $\Delta\theta$ is the change in temperature and measured as $\theta_m - \theta$ . Here, $\theta_m$ is the melting temperature (i.e., 0 °C), and $\theta$ is the current temperature. ....	85
Figure 15. Effect of light weight aggregate and air entrainment on the tangential stresses ( $\sigma_t$ ) for MD4, MD5, and MD6. ....	89
Figure 16. Effect of SCMs and the air void spacing factor on the tangential stresses ( $\sigma_t$ ) developed in the concrete sphere (MD10 –15). Superscripts $a$ and $p$ denote aggregate and mortar matrix, respectively. ....	90
Figure 17. Effect of cooling rate on the average bulk strain ( $\varepsilon_{kk}$ ), pore pressure at the aggregate center ( $p^{a-L}$ ), and peak tangential stresses ( $\sigma_t^p$ ) developed at the matrix outer boundary for the mixture designs, MD7 with cooling rate of 2 °C/h, 5 °C/h, and 10 °C/h. ....	93
Figure 18. Effect of aggregate size and permeability on the average bulk strain ( $\varepsilon_{kk}$ ), pore pressure at the aggregate center ( $p^{a-L}$ ), and peak tangential stresses developed at the matrix outer boundary ( $\sigma_t^p$ ) exposed to a cooling rate of 10 °C/h (MD7, MD8, MD9, & MD10). ....	94
Figure 19. Schematics of freezing mechanisms in partially saturated concrete.....	100
Figure 20. (a) A composite concrete cryogenic tank section. Image courtesy BergerABAM, (b) Boundary conditions pertaining to the primary concrete containment wall shown in (a).....	107
Figure 21. (a) Temperature, (b) pore liquid pressure, (c) liquid saturation, (d) bulk strain, and (e) stresses in the $Y$ and $Z$ directions in a 0.4 m thick concrete (non-air-entrained) wall directly exposed to cryogenic temperature at $x=0\text{m}$ . The concrete wall is simulated as liquid tight and insulated with perlite layer on the reverse side. ....	108
Figure 22. (a) Temperature, (b) pore liquid pressure, (c) liquid saturation, (d) bulk strain, and (e) stresses in the $Y$ and $Z$ directions in a 0.4 m thick concrete (air-entrained) wall directly exposed to cryogenic temperature at $x=0\text{m}$ .	

The concrete wall is liquid tight and insulated with perlite layer on the reverse side. ....	109
Figure 23. Effect of cooling rate on (a) temperature profile, (b) pore liquid pressure, (c) liquid saturation, (d) bulk strain, and (e) stresses for non-air-entrained and air-entrained primary containment concrete wall. Plots with markers (solid and empty triangular, circular and square) represent variables at the reverse side of the wall ( $x=0.4\text{m}$ ). Solid line shows values at the innermost surface directly in contact with the LNG ( $x=0\text{m}$ ). ....	110
Figure 24. Initial humidity and saturation profile for partially saturated concrete. The concrete wall cross-section consists of a fully saturated strip in the middle bounded by unsaturated strips on the boundaries. ....	113
Figure 25. (a) Temperature, (b) pore liquid pressure, (c) liquid saturation, (d) bulk strain, and (e) stresses in the Y and Z directions in a 0.4 m thick partially saturated non-air-entrained concrete wall. ....	114
Figure 26. (a) Spatial mean pore liquid pressure, (b) spatial mean liquid saturation, (c) spatial mean bulk strain, and (d) spatial mean stresses for fully and partially saturated non-air-entrained, and air-entrained primary containment concrete wall. ....	115
Figure 27. Effect of cryo-swelling on the deformation of cryogenic concrete. The wall surface in contact with the cryogenic fluid contracts less than the outer boundary (d) because of the cryo-swelling induced by the thermodynamic equilibrium and the subsequent cryo-suction. ....	119
Figure 28. Effect of salt concentrations in pore solution on the liquid saturation, pore pressure, and strain of a sealed concrete specimen. Depending on the minimum temperature to which concrete is exposed, an optimum salt concentration is possible to achieve that causes maximum strains. ....	125
Figure 29. Change in volume of the pore solution with temperature for varying salt concentrations. ....	126
Figure 30. Effect of salt concentrations in pore solution on the liquid saturation, pore pressure, and strain of a sealed concrete specimen with fine pore structures. ....	127
Figure 31. Effect of porosity on the liquid saturation, disjoining pressure, pore liquid pressure, and strain of concrete specimens. Reduction in porosity can reduce the expansion significantly by reducing the effect of hydraulic pressure. ....	128

Figure 32. Schematics of stress distribution in liquid film due to repulsive force acting within the film.....	131
Figure 33. Effect of disjoining pressure on ice propagation, pore pressure, and strain. Disjoining pressure favors crystal growth and increases the magnitude of the hydraulic pressure and strain. ....	132
Figure 34. Comparison of the modeled results with the experimental data found in [132]. Material properties used for simulation are $\phi_0 = 0.26$ , $K_s = 31.8 \times 10^3 \text{ MPa}$ , $\alpha = 14.5 \times 10^{-6} \text{ }^\circ\text{C}^{-1}$ and $\nu = 0.2$ . ....	134
Figure 35. Comparison of the modeled results with the experimental data found in [132]. Simulation was performed for $\phi_0 = 0.13$ , $K_s = 31.8 \times 10^3 \text{ MPa}$ , $\alpha = 17.7 \times 10^{-6} \text{ }^\circ\text{C}^{-1}$ and $\nu = 0.2$ . ....	135

## LIST OF TABLES

	Page
Table 1. Summary of research objectives and research need.....	9
Table 2. Summary of equations for thermoporoelasticity of freezing porous media.....	38
Table 3. Material properties used for sensitivity analysis where, $\phi_0$ is the porosity, $m$ is the shape factor in the van Genuchten model [27] relating to the pore size distribution, $k$ is the permeability, $\alpha$ is the coefficient of thermal expansion, and $R_*$ is the pore radius related to the characteristic cooling. Superscripts, $a$ and $p$ denote aggregate and matrix, respectively. ....	64
Table 4. Mixture design input parameters and the related material properties. ....	81

## 1 INTRODUCTION

In cold climate regions, the most prevalent form of pavement distress is exhibited due to the cyclic freezing and thawing of saturated concrete. For this reason, concrete frost damage is still the focus of immense research despite the fact that abundant laboratory and field observations and theoretical investigations are present on the subject. Due to the complex pore size distribution and composite nature, as water freezes in concrete and ice progressively invades smaller pores with decreasing temperature, multiple deformation mechanisms take place: high pore pressure builds up due to the difference of density between the liquid water and ice; unfrozen water is expelled from the frozen pores to the nearest low pressure boundary to relieve the excess pressure; crystallization pressure develops due to the interfacial energy effects between different phases; supercooled water from small pores are drawn to the ice crystals in big pores by cryogenic suction; and aggregate, cement paste, ice crystals, as well as the supercooled liquid water contract or expand with different coefficients of thermal expansion [1]. The problem becomes even more complicated when the pore network is saturated with salt solution instead of pure water. Therefore, depending on the constituent materials, pore characteristics, composition of the pore solution, degree of saturation, and the environmental exposure, degradation of concrete by freeze-thaw actions can manifest in several forms; among these D-cracking, popouts, surface cracking, and scaling are the most common signs of frost deterioration.

## 1.1 Problem statement

Concrete pavements in Texas and other states have a severe problem with expansive aggregate induced damage, and require extensive rehabilitation within 10 years of service. As reported in several research projects, expansion of aggregates is often associated with freeze-thaw cycles resulting in D-cracking and popouts [1–3]. While much research [4–7] has already been performed studying freeze-thaw related damage in concrete, the research has primarily focused on empirical or semi-empirical experimental investigations of mechanisms and/or effects on structural capacity. These experiments are expensive, time consuming, and difficult to maintain. Furthermore, past theoretical studies involving freezing concrete were particularly aimed to understand or explain mechanisms of frost action in concrete or cement paste [8–17]. Little work has been done to investigate the role of mechanics and constitutive properties of concrete phases in the formation and growth of damage in concrete due to freezing of aggregates. The limited knowledge related to the understanding and modeling of concrete responses under freezing and thawing cycles led to several issues and challenges.

### *1.1.1 Overly simplistic design*

Entraining air bubbles has been universally recognized as effective and reliable damage mitigation means against freeze-thaw cycles [2-7]. For a protective air-void system, a maximum spacing factor of 0.2 mm (0.008 in) and a minimum specific surface area of  $25 \text{ mm}^2/\text{mm}^3$  ( $600 \text{ in}^2/\text{in}^3$ ) are suggested by ASTM C 457. To attain these values in the field for fresh concrete, a minimum air content of 3% by volume of concrete is specified for all concrete (including high strength/high performance concrete) by ACI

201.2R based on the maximum size of the coarse aggregate. As high mortar fraction is required to coat small aggregates, high air content is prescribed for small aggregates. These threshold values were established based on the historical works of Powers [2-4, 8] and Klieger [9, 10] performed in the 1950s.

Since then, development of new materials has widened the choice for concrete constituents to a great extent and introduced different types of cement, supplementary cementitious materials (SCMs), synthetic aggregates, and a variety of synthetic air-entraining and other chemical admixtures. Consequently, a diverse variety of hardened concrete characteristics is possible, which directly influences the frost damage susceptibility of the concrete pavement. For instance, pore characteristics of both the aggregate and mortar play significant role in the freezing deformation of concrete whose pore network is completely filled with water [11-17]. Low concrete durability can be attributed to the high-porosity, low-permeability aggregates with fine pore structure that cause high internal pressure due to delayed relaxation of excess pore water [11-13]. Big aggregates further exacerbate the problem by increasing the distance that the expelled water has to travel from the frozen capillary pores to the escape boundary (i.e. the air void surface) [14, 17]. Importance of coefficient of thermal expansion (CTE) of the various phases present in concrete is significant since high differences between the CTEs of the different constituents can develop high internal stresses by causing high differential strain [18-20]. Furthermore, deterioration due to freezing deformation is vastly dependent on the freezing environment to which the concrete pavement is exposed [7, 21]. Regardless of these facts, the frost resistance of concrete is commonly

evaluated using the air void parameters alone and does not include the effect of material properties and environmental exposure in specifying freeze-thaw durability of a certain concrete mixture design.

#### *1.1.2 Inability to predict freezing deformation due to pore solution speciation*

Every year millions of tons of deicing salts are used worldwide to provide safe highways as the deicers suppress the freezing point by several degrees and melt the ice on the pavement surface. Naturally, one would expect that since deicers can suppress the pore water freezing, it would at least delay the progression of frost damage. However, the contrary is observed where more expansion and damage are reported for concrete specimens saturated with high concentration of NaCl solution than specimens filled with pure water [22]. Furthermore, these salts can pose severe threat to the concrete structures [13, 20, 23-27]. Foreign species when dissolved in water can transport to the concrete interior and react with the cement paste, aggregate, and rebar and form harmful and expansive compounds. Therefore, the existing theory needs to be modified to account for the presence of dissolved salts and its subsequent effect on the liquid saturation to accurately predict concrete deformation at subzero temperatures.

#### *1.1.3 Erroneous modeling due to the omission of disjoining pressure*

When a spherical crystal nucleates in a pore network, it grows in all directions until it approaches the surface of the pore wall. The crystal-pore wall interfacial energy is so high that it is always favorable to sustain crystal-liquid and liquid-pore wall interfaces in opposition to the direct contact between the crystal and pore wall. Consequently, a thin liquid film fills up the gap between the pore wall and the crystal.

Across this liquid film, a repulsive force, namely disjoining pressure, remains active that allows the crystal to grow and continuously push the pore wall [15, 28]. Due to this repulsive force, the liquid film exhibits higher pressure than the bulk liquid a distance away from the liquid-crystal interface. Mechanical equilibrium would require this extra pore pressure to be alleviated by expelling liquid from the high-pressure zone to a region where pressure is low. However, properties of liquid constrained between two solid surfaces change drastically: the liquid molecules become more ordered, the liquid progressively behaves more solid-like than liquid-like, and the mobility of the film reduces by multiple orders [29-33]. The Newtonian viscosity concept no longer holds true for such thin film as the liquid can resist shear stress. The classical liquid-crystal thermodynamic equation, well known as Thomson's equation, assumes that spherical stress state prevails in both the liquid and the crystal, and thus neglects the elastic energy term associated with the shear stresses introduced by the confinement. Applicability of the Thomson's equation to porous materials thus becomes questionable, especially at low temperatures (e.g. concrete tanks utilized for LNG storage) where the only liquid is found wrapping around the crystals, a few nanometers thick to prevent dry contact with the pore wall.

#### *1.1.4 Inability to utilize concrete for primary containment of LNG*

Concrete, because of its enhanced mechanical properties under cryogenic temperatures, as well as its economy, availability, casting simplicity and robustness has also gained widespread popularity as a suitable construction material for large scale storage tanks of liquefied natural gas (LNG). Much of the previous research

investigating the cryogenic behavior of concrete was published in the 1960s and 1970s which is out of print, and thus no longer readily accessible. Moreover, the available knowledge lacks important information regarding the concrete properties under cryogenic temperatures (i.e., temperatures  $\leq -160^{\circ}\text{C}$ ) that is essential to design concrete walled primary containment tank.

Thermal deformation of concrete is of critical importance while designing LNG tanks because of the large temperature change that the various components of the structure go through while being cooled down to cryogenic temperature from room temperature. Significant differences between thermal deformation of concrete and that of the other members may damage the structure by developing high internal stresses. In addition, thermal deformation of saturated concrete can be substantially influenced by the rate of cooling. Hence, in order to safely utilize concrete for primary containment of LNG, it is crucial to be able to accurately predict concrete CTE, and fully understand the role of moisture content and effect of cooling rate on the thermal deformation as the material is cooled from room temperature to cryogenic temperature.

## **1.2 Research scope and objectives**

Poroelastic theory [34, 35] has been used successfully to analyze concrete and cement paste characteristics [36-40], and model behavior of cement paste exposed to freezing temperatures [1, 41-43], but has not been applied to the problem of freezing aggregates within concrete. Thus, the focus of this research is to elucidate the freeze-thaw damage mechanisms in concrete due to substandard aggregates in order to theoretically validate and mechanistically explain experimental findings in the literature.

A simplified poromechanical model is used to predict the destructive tensile stress created in the aggregate and/or cement paste or mortar matrix associated with the freezing process. This model is developed with the intention to help practitioners select appropriate materials (e.g. aggregate type, size, w/c ratio, supplementary cementitious materials) for concrete pavements with minimal D-cracking and pop-out damage. The theory presented in this work identifies the causes of freeze-thaw damages, and does not explain damage mechanism evolving with successive freeze-thaw cycles.

We also intend to leverage the aforementioned poroelastic model of composite concrete to predict the optimum air void system specific to a concrete mixture design used for pavement construction without compromising the strength and permeability significantly. Significance of the concrete constituent properties and environmental exposure on the crack initiating tensile stresses and the efficiency of the air void system parameter (precisely the spacing factor) are studied to determine the role of air voids on the damage susceptibility of concrete exposed to freezing temperatures.

And finally, to demonstrate the effect of pore solution speciation and disjoining pressure on the liquid-solid phase transition, we have derived the solid-liquid thermodynamic equation within the framework of mixture theory adopted by Grasley and Rajagopal [44]. Poroelasticity is then utilized to determine deformation of porous materials saturated with salt solution and exposed to freezing temperatures. This study, however, does not account for the supersaturation of solutes upon the removal of solvent from the pore solution as ice deposits.

In addition, this study aims to utilize poroelasticity to predict freezing strain of saturated cryogenic concrete and demonstrate the effect of cooling rate and the subsequent temperature gradient on the deformation of the primary containment concrete wall. The unsaturated freezing theory is then presented to include gas as a third phase (in addition to liquid and crystal) to model stress and deformation of partially saturated freezing concrete to validate the role of moisture content found in the literature. The proposed model is believed to help engineer concrete mixture design for successful construction of concrete walled LNG tanks along with the choice of optimum cooling rate and moisture content. Again, only deformation caused by the cryogenic cooling (loading) will be considered in this study. Effect of thawing (unloading) and multiple freeze-thaw cycles and the resulting fatigue damage is not considered.

The primary objectives of this research are summarized in Table 1.

**Table 1. Summary of research objectives and research need**

<b>Research objective</b>	<b>Research need</b>
➤ Derive a thermoporomechanical model	<ul style="list-style-type: none"> <li>- to predict destructive tensile stresses caused by substandard aggregates</li> <li>- to demonstrate the effect of air void spacing on tensile stresses and deformation of concrete</li> <li>- to determine thermal expansion of cryogenic concrete</li> <li>- to investigate effect of cooling rate and moisture content on concrete deformation and stresses under cryogenic temperatures</li> </ul>
➤ Investigate the role of constitutive properties of concrete phases in the formation of damage via computer simulations implementing the derived model	<ul style="list-style-type: none"> <li>- to identify D-cracking susceptible aggregates and mixture design</li> <li>- to study optimum air void spacing for a certain concrete mixture design</li> <li>- to obtain concrete mixture design with the least vulnerability to destructive stresses under cryogenic temperatures</li> </ul>
➤ Use the developed model to evaluate concrete compatibility for the construction of LNG tanks	<ul style="list-style-type: none"> <li>- to explore suitability of concrete for different components (e.g. floor, walls without liner) of LNG tanks</li> </ul>
➤ Improve the existing theory, i.e. incorporate the effect of pore solution speciation and liquid confinement in the deformation of freezing concrete	<ul style="list-style-type: none"> <li>- to evaluate the shift in pore freezing due to the presence of dissolved ions and disjoining pressure</li> <li>- to examine the subsequent change in thermal deformation of frozen concrete</li> </ul>
➤ Provide a guideline on the concrete mixture design	<ul style="list-style-type: none"> <li>- to design durable concrete pavement</li> <li>- to construct safe and economic concrete walled LNG tanks</li> </ul>

### **1.3 Research outline**

The research tasks performed to attain the aforementioned objectives, that eventually furnished this dissertation, are organized into the following sections:

Section 1 briefly introduces the problem followed by an itemized list of objectives and dissertation outline.

A concise review of the existing literature related to the problem is depicted in section 2. Existing experimental findings on aggregate properties accountable for frost deterioration are compiled in section 2.1. The present specifications for the air void system established by the code writing bodies and the recent work studying the influence of air void parameters on modern concrete are presented in section 2.2. Current practice regarding the use of concrete as the primary material for the construction of LNG tanks is recapitulated in section 2.3.

Section 3 proposes a general scheme for modeling pore pressure, stress, strain, and temperature fields exhibited by porous material exposed to freezing temperatures. The solid-liquid thermodynamic equilibrium equation has been extended in this section to assimilate the effect of pore solution speciation and liquid confinement on the deformation of freezing porous media.

Section 4 employs the theory introduced in section 3 to mechanistically identify deleterious aggregate properties that may degrade concrete durability under frost actions. Section 5 extends the same model to optimize the air void spacing requirement for specific concrete mixture design exposed to certain environmental conditions. These results are then verified by the experimental findings recounted in section 2.

Section 6 extends the theory of thermoporoelasticity to simulate the deformation of concrete subjected to cryogenic temperatures. Effect of cooling rate and moisture

content is also studied in this section to provide suggestions for the safe and durable construction of concrete walled LNG tanks.

A simple solution of NaCl is adopted to demonstrate the effect of pore solution speciation on the depression of freezing point and the subsequent changes on the deformation of the porous material in section 7. Influence of the disjoining pressure on the solid-liquid phase transition and the deformation of the porous media is also investigated in this section.

Finally, section 8 concludes this dissertation with the most important findings derived from sections 3 to 7. Some recommendations for practitioner to help them select appropriate concrete mixture constituents and proportions to build safe and durable concrete structures are also provided in this section.

A flowchart summarizing the aforesaid objectives and the research layout is displayed in Figure 1.

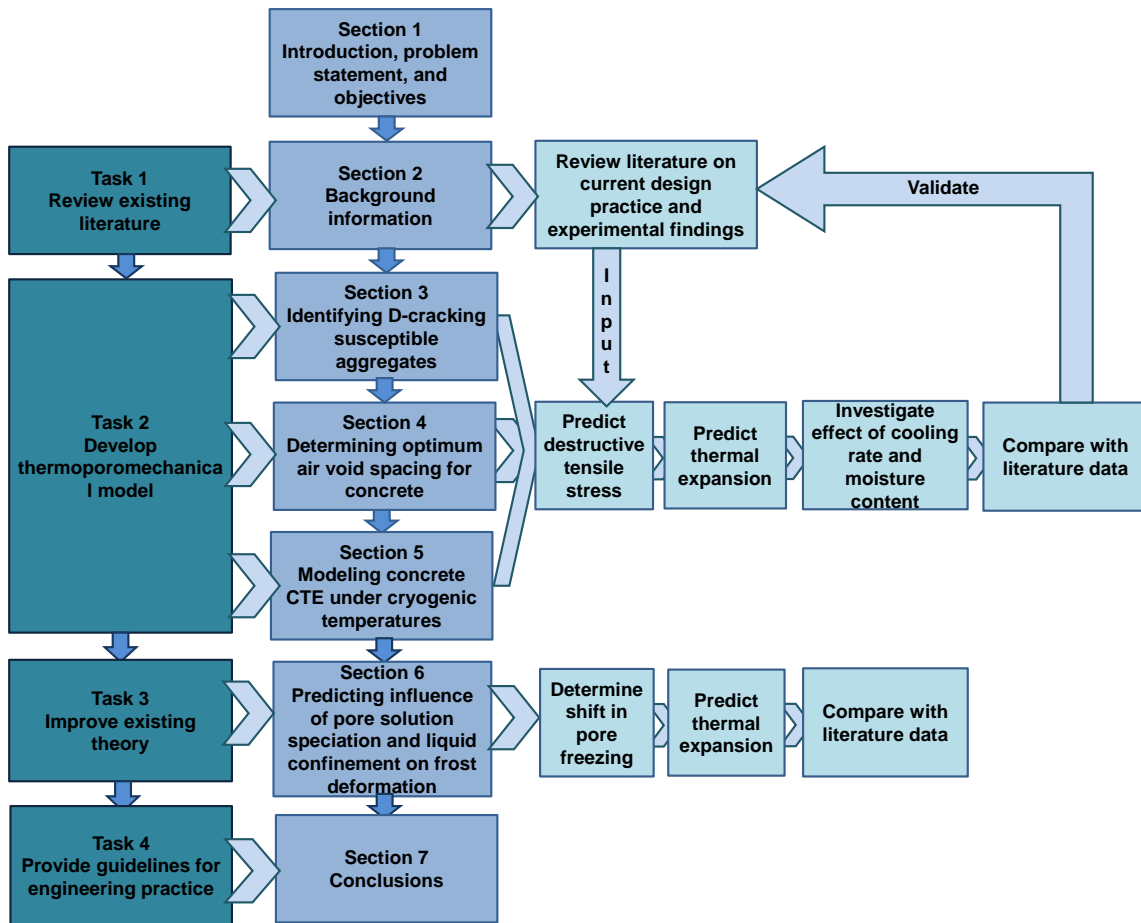


Figure 1. Flowchart for the performed research tasks.

## 2 BACKGROUND INFORMATION

Over the past years, numerous research projects regarding concrete deterioration by freezing and thawing actions were performed [3–5,7,25]. Most of these projects include experimental investigation providing ample data which is readily utilized in this work to validate the proposed model. A review of the influence of aggregate properties on concrete frost damage is presented in section 2.1. Current practice regarding the use of air voids on mitigating frost damage is summarized in section 2.2. Existing literature associated with the composite concrete cryogenic tanks [18,26–29] is also surveyed to adopt appropriate boundary conditions for the model pertaining to the concrete walled LNG tanks. Section 2.3 briefly reviews the current practice related to the use of concrete as a primary material for the construction of LNG tanks.

### **2.1 Effect of aggregates on frost damage**

D-cracking, caused by freezing and thawing of water saturated concrete, typically appears as a series of closely spaced, crescent-shaped cracks along joints in concrete slabs. This type of damage is a progressive structural deterioration of the concrete that has been linked to certain types of susceptible coarse aggregates [45]. D-cracking occurs parallel and adjacent to longitudinal and transverse joints, intermediate cracks, and the free edges of pavement slabs where concrete is exposed to wet and dry cycles at both the top surface and sides of slabs. According to Stark [14], aggregates that have potential to cause D-cracking are also susceptible to popout. A popout is a conical depression created on the surface of the concrete leaving a fragment of the fractured

aggregate particle at the bottom of the cavity with the other part sticking to the apex of the popout cone.

Various studies have established that the pore characteristics of aggregates significantly influences the frost resistance of concrete [11, 14, 45]. According to Verbeck and Landgren, low-porosity and low permeability aggregates, typical of quartzites, marbles, and traprocks are strong enough to withstand freezing distress. However, high-porosity but low-permeability aggregates, typical of cherts with a fine pore structure, can exhibit failure due to high internal pressures within the aggregates [11]. In the same study, it was estimated that peak pore pressure generated in low-permeability chert may be 100 times greater than for the high-permeability dolomite. Later, Kaneuji established a correlation between the pore structure of aggregates and concrete freeze-thaw durability, and attributed low aggregate durability to high pore volume and smaller median pore diameter [12]. It was noted in the study, however, that aggregate pores with radii less than 4.5 nm did not appear to contribute to freeze-thaw durability problems. Mehta and Monteiro associated D-cracking with coarse aggregates that contain high pore volume in the narrow pore size range (0.1 to 1  $\mu\text{m}$ ) [13]. Scherer also suggested that crystallization stress is lower for larger pores and lower crystal-pore wall contact angles [15]. However, as stated by Verbeck and Landgren, the high-porosity, high-permeability aggregates with coarse pore structure – if covered by mortar – can cause failure due to the high external pressure built up in the matrix [11]. Examples of such aggregates are limestones, dolomites, and sandstones. In this case, failure depends on the rate of temperature drop and the distance water must travel to find

an escape boundary [11]. Several studies suggest that reducing the maximum size of D-cracking susceptible aggregate particles improves the freeze-thaw durability of concrete and slows down the rate of development of D-cracking [14, 17, 45, 46]. Research by Verbeck and Landgren indicates that aggregates with higher permeability can include larger sizes without inducing freeze-thaw damage [11]. Therefore, smaller size aggregates with low porosity and high permeability perform better than the larger ones with respect to resistance to D-cracking.

As reported by Alexander and Mindess [18], the importance of aggregate coefficient of thermal expansion (CTE) to the performance of concrete under thermal cycling is twofold: first, it influences the CTE of the concrete and hence thermal movements in structures; and second, it may contribute to the development of internal stresses if there are large differences between the CTEs of the various constituents. Callan stated that the durability of the concrete may be low where the difference between the CTEs of coarse aggregate and cement paste is large, and the maximum stress in that case occurs at the aggregate-matrix interfacial boundary [19]. Therefore, it is suggested that the difference between CTEs of coarse aggregate and matrix in which they are embedded should not exceed about  $5.4 \times 10^{-6} \text{C}^{-1}$  [19].

## **2.2 Role of air voids in mitigating frost damage**

Dependence of the air content requirement on the aggregate size, as presented in ACI 201.2R, is solely due to the fact that high mortar content is required for small aggregates to maintain the same workability as the big aggregates. Consequently, high air content is required to protect the thick mortar cover around the small aggregates.

Since air void cannot be inserted into aggregates, the functionality of the air void is entirely restricted to the cement paste or mortar volume fraction. With this limitation in mind, the original theoretical air void spacing requirement was developed based on the assumption that only the cement paste becomes completely saturated, and concrete as a whole never becomes wet [2]. This hypothesis led to a very simplistic case where aggregates never reach full saturation. However, there has been evidence that the average capillary pores in aggregates are much larger than the hardened cement paste and ice propagates faster in saturated aggregates than the latter [13, 47]. As a consequence, supercooled water from the frozen capillaries in aggregates is expelled to the nearest paste matrix. If this expelled water is not properly accommodated, significant frost damage can be done depending on the cooling rate, saturation degree, and pore characteristics of aggregates [11, 47]. Since aggregates constitute around 60 to 80% of the total concrete volume, a significant portion of the concrete thus remains unprotected even with the specified air content.

Entrained air bubbles relax the excess pore pressure by accommodating the expelled water from the frozen capillaries and freezing it instantly [41, 42, 47]. As a result air-entrained cement matrix contracts more than the aggregates that do not contain any impregnated air. This excessive contraction of the air-entrained cement or mortar matrix compared to the aggregate, which contains minimal air, may cause a differential strain gradient between the aggregate and matrix. This strain gradient may lead to destructive tensile stresses in the interfacial transition zone (ITZ), making concrete vulnerable to freezing damage. Recently, a quantitative image analysis study of crack

evolution in freezing concrete supported this hypothesis by showing that the ITZ cracks contribute significantly to the freeze-thaw damage of air-entrained concrete [48].

A recent study performed by FHWA Office of Infrastructure Research and Development reported that satisfactory durability performance can be obtained for specific concrete with spacing factor higher than the specified value, and air content less than that required by the ACI [49]. Other studies dealing with frost resistant high strength concrete also reported that the spacing factor requirement increases with decreasing water to cement ratio (w/c) [50, 51]. A series of studies showed that high strength concrete with w/c less than 0.25 can successfully withstand frost damage without any entrained air [52-56]. These concrete mixtures however do not comply with the ACI 318 minimum requirement of air content for frost resistance. Excessive amounts of air than that necessary for mitigating freezing damage can cause loss of strength and increase in permeability, which in turn can negatively affect the durability of concrete. Concrete strength is anticipated to be decreased by 5% for an increase of 1% of entrained air [20]. Efforts to counteract such reductions in strength may include increasing the cement content with a concurrent increase in cost [50].

### **2.3 Concrete walled LNG tanks**

Liquefying natural gas by cooling down to  $-160^{\circ}\text{C}$  is an extremely efficient storage method as material volume is reduced drastically. Concrete, due to its economy, availability, casting simplicity and robustness has gained widespread popularity as a suitable construction material for large scale storage tanks of liquefied natural gas (LNG). Over the past years, numerous research studies have been performed to study

mechanical and thermal behavior of concrete subjected to freezing temperatures [1-3, 5, 11, 15, 16, 41, 42, 57-59]. Most of these studies primarily focus on concrete freezing down to  $-30^{\circ}\text{C}$ . Little is known about the properties of concrete at cryogenic temperatures (i.e., temperatures  $\leq -160^{\circ}\text{C}$ ) that are critical for the design of concrete-walled LNG tanks.

A comprehensive literature survey of the concrete mechanical and thermal properties subjected to single cycle cryogenic freezing has been documented by Krstulovic-Opara [60]. Kogbara et al. [61] recently extended this review to include the effect of thermal cycles on concrete properties necessary to design concrete tanks for direct containment of LNG. All the reviewed studies unanimously reported substantial variation of concrete properties at cryogenic temperatures that largely depends on the moisture content. For example, dry concrete shows linear contraction with cooling whereas saturated non-air-entrained concrete expands up to several hundred microstrains. Saturated concrete, because of its complex pore network, can contain varying proportion of ice crystals, vapor, and liquid at different temperatures. As a result, a complex thermal deformation is observed with high moisture content through which concrete contracts at the onset of cooling, expands between  $-20$  to  $-70^{\circ}\text{C}$ , and reverts to contraction upon further cooling [62-67]. Several researchers also identified that the higher the moisture content, the higher the expansion [60, 68, 69]. A critical relative humidity of 86% has been reported below which no expansion is observed [60, 69]. In the absence of moisture, aggregate type governs the thermal deformation of the cryogenic concrete since aggregate constitutes more than 70% of the typical concrete

volume [70]. Kogbara et al. investigated the effect of aggregate type on the change in microstructure of saturated concrete subjected to cryogenic freezing [71]. They found that high-porosity lightweight aggregate concrete is more susceptible to damage than the low-porosity traprock and limestone aggregate concrete due to the increased moisture movement leading to high internal stresses and successive disruptive volumetric change [71].

There has been ample evidence that thermal deformation of saturated concrete is significantly influenced by the rate of cooling. A slow cooling rate is reported to cause underpressure in small pores whereas a high cooling rate triggers overpressurization in the larger pores [72]. High cooling rate nucleates ice in the mesopores faster than the transfer rate of the excess water to the nearest boundary and leads to overpressurization in the pore network. Subsequently, high stresses result in microcracking inducing irreversible expansion [69]. Although many published experimental works register cooling rates as high as 60 °C/hr [73], 150 °C/hr [62] and 392 °C/hr [67], a much slower cooling rate of 0.6 °C/hr to 1.3 °C/hr has been suggested by practitioners to avoid overstressing of the primary LNG containment tank [74].

Thermal deformation of concrete is of critical importance while designing LNG tanks because of the large temperature change that the various components of the structure go through while being cooled down to cryogenic temperature from ambient temperature. In a common composite concrete cryogenic tank, a plane carbon steel liquid/vapor barrier is fastened around the concrete wall to prevent leaking, and 9% nickel steel plate is used as the bottom of the containment tank that is attached to the

concrete wall. It has been reported that the composite concrete wall of a 160,000 m<sup>3</sup> capacity tank can move up to 64 mm inward as temperature drops down to  $-188^{\circ}\text{C}$  [74]. Therefore, significant differences between thermal deformation of concrete and that of the 9% nickel steel and carbon steel may damage the structure by developing high internal stresses. Currently, for design purposes, an average CTE of  $9.9 \times 10^{-6} \text{ }^{\circ}\text{C}^{-1}$  is used for both the carbon steel and 9% nickel steel, and a CTE between  $7.9 \times 10^{-6}$  to  $9.4 \times 10^{-6} \text{ }^{\circ}\text{C}^{-1}$  is used for concrete [74]. However, researchers have showed that CTE of concrete may attain a negative value due to high moisture content [3, 75] (depending on cooling rate and air bubble spacing) causing cracks and creating internal stresses within the structure.

### 3 MODELING FREEZING POROUS MEDIA

Recently, Grasley and Rajagopal [44] derived accurate expressions for total, matric, and osmotic suction in a capillary system within the framework of mixture theory. In section 3.1, we follow the same approach to develop the liquid-solid phase transition thermodynamic relation. A set of governing equations comprising linear momentum balance for the total stress, mass balance for the fluid content, and energy balance for the heat transfer is presented in section 3.2. Theory of unsaturated poroelasticity is then recapitulated in section 3.3.

#### 3.1 Liquid solid phase transition

In light of the mixture theory presented by Grasley and Rajagopal [34, 44] The molar internal energy,  $\bar{u}^i$  of any species  $i$  can be expressed as

$$\bar{N}^i \frac{d\bar{u}^i}{dt} = \bar{N}^i \theta^i \frac{d\bar{S}^i}{dt} + \mu^i \frac{d\bar{N}^i}{dt} + \bar{V}_0 \underline{T}^i : \frac{d\underline{\underline{\epsilon}}^i}{dt}. \quad (3.1)$$

where kinetic and potential (e.g., from gravity or electric fields) energy have been ignored. Here,  $\bar{S}^i$  is the molar entropy of species  $i$ ,  $\mu^i$  is the molar chemical potential of species  $i$ ,  $\theta^i$  is the temperature of species  $i$ ,  $\bar{V}_0$  is the molar volume of the mixture at the reference state,  $\underline{T}^i$  is the partial Cauchy stress tensor of species  $i$ , and  $\underline{\underline{\epsilon}}^i$  is the infinitesimal strain tensor (which presumes the norm of the displacement gradient is sufficiently small) of species  $i$ .  $\bar{N}^i$  is the molar fraction of the individual species defined as

$$\bar{N}^i = \frac{N^i}{N}. \quad (3.2)$$

Here,  $N^i$  denotes the current number of moles of component  $i$ , and  $N$  presents the total number of moles of the mixture.

Now,  $\bar{V}_0 T^i : \frac{d \underline{\underline{\epsilon}}^i}{dt}$  can be written in terms of the mean stress,  $\sigma^i$  and the

deviatoric stress,  $\underline{\underline{s}}^i$  as

$$\bar{V}_0 T^i : \frac{d \underline{\underline{\epsilon}}^i}{dt} = \bar{V}_0 \sigma^i \frac{d \epsilon^i}{dt} + \bar{V}_0 \underline{\underline{s}}^i : \frac{d \underline{\underline{e}}^i}{dt}, \quad (3.3)$$

where,  $\epsilon^i$  is the current infinitesimal volumetric strain related to species  $i$  with respect to the reference state and defined as

$$\epsilon^i = \frac{\bar{V}^i - \bar{V}_0^i}{\bar{V}_0^i}, \quad (3.4)$$

where  $\bar{V}^i$  is the current molar volume of the species  $i$ , and  $\underline{\underline{e}}^i$  is the current

infinitesimal deviatoric strain tensor. With the help of (3.4), equation (3.3) reduces to

$$\bar{V}_0 T^i : \frac{d \underline{\underline{\epsilon}}^i}{dt} = \frac{\bar{V}_0}{\bar{V}_0^i} \sigma^i \frac{d \bar{V}^i}{dt} + \bar{V}_0 \underline{\underline{s}}^i : \frac{d \underline{\underline{e}}^i}{dt}. \quad (3.5)$$

Now we apply (3.5) in (3.1) and implement Legendre transform to derive

$$\bar{N}^i \frac{d \mu^i}{dt} + \bar{N}^i \bar{S}^i \frac{d \theta^i}{dt} + \frac{\bar{V}_0}{\bar{V}_0^i} \bar{V}^i \frac{d \sigma^i}{dt} + \bar{V}_0 \underline{\underline{e}}^i : \frac{d \underline{\underline{s}}^i}{dt} = 0. \quad (3.6)$$

Here, we also consider that at equilibrium, the rate of energy is zero. For a mixture, we can write

$$\sum_{i=1}^n \bar{N}^i \frac{d\mu^i}{dt} + \bar{S} \frac{d\theta}{dt} + \bar{V} \frac{d\sigma}{dt} + \bar{V}_0 \underline{\underline{e}} \frac{d\underline{\underline{s}}}{dt} = 0 \quad (3.7)$$

Let us now consider the problem of two chemically dependent phases that coexist in equilibrium. This problem could represent, for example, liquid in equilibrium with its vapor or liquid in equilibrium with its frozen or solid phase. Since liquids often include dissolved species, it is advantageous to consider that we have a mixture that exists at two levels: first, the liquid itself is a mixture consisting of water and various other dissolved species; second, the presence of liquid and its vapor or solidified phase represents a mixture at a higher scale. Thus, we can write for the mixture of ice and salt crystal,

$$\begin{aligned} & \bar{N}^{c-\text{H}_2\text{O}} \frac{d\mu^{c-\text{H}_2\text{O}}}{dt} + \sum_{i=1}^n \bar{N}^{c-i} \frac{d\mu^{c-i}}{dt} + \bar{V}_0^c \frac{d\sigma^c}{dt} + \bar{V}_0^c \frac{\sigma^c}{K^c} \frac{d\sigma^c}{dt} + 3\alpha^c (\theta^c - \theta_m^c) \bar{V}_0^c \frac{d\sigma^c}{dt} \\ & + \bar{V}_0^c \frac{\underline{\underline{s}}^c}{2G^c} \frac{d\underline{\underline{s}}^c}{dt} + \bar{S}_0^c \frac{d\theta^c}{dt} = 0 \end{aligned} \quad (3.8)$$

where  $\bar{V}$ , the molar volume of the mixture, is replaced by the relation

$$\bar{V} = \bar{V}_0 \left[ 1 + \frac{\sigma}{K} + 3\alpha(\theta - \theta_m) \right], \quad (3.9)$$

and

$$\underline{\underline{e}} = \frac{\underline{\underline{s}}}{2G} \text{ is used.} \quad (3.10)$$

Here, we have constrained the discussion to linearly elastic solids and affixed the reference configuration at the melting temperature. In (3.9),  $\alpha$  is the coefficient of

thermal expansion of the mixture, and  $K$  and  $G$  are the bulk modulus and shear modulus of the mixture, respectively. Equation (3.8) ignores the entropic term related to the heat capacity and can be rearranged to read

$$\begin{aligned} \frac{d\mu^{C-H_2O}}{dt} = & -\frac{1}{\bar{N}^{C-H_2O}} \sum_{i=1}^n \bar{N}^{C-i} \frac{d\mu^{C-i}}{dt} - \frac{\bar{V}_0^C}{\bar{N}^{C-H_2O}} \frac{d\sigma^C}{dt} - \frac{\bar{V}_0^C}{\bar{N}^{C-H_2O}} \frac{\sigma^C}{K^C} \frac{d\sigma^C}{dt} \\ & - 3\alpha^C (\theta^C - \theta_m^C) \frac{\bar{V}_0^C}{\bar{N}^{C-H_2O}} \frac{d\sigma^C}{dt} - \frac{\bar{V}_0^C}{\bar{N}^{C-H_2O}} \frac{s^C}{2G^C} \frac{ds^C}{dt} - \frac{\bar{S}_0^C}{\bar{N}^{C-H_2O}} \frac{d\theta^C}{dt} \end{aligned} \quad (3.11)$$

Let us now consider that the primary phase in the liquid is water. Thus, (3.7)

takes the form

$$\bar{N}^{L-H_2O} \frac{d\mu^{L-H_2O}}{dt} + \sum_{i=1}^n \bar{N}^{L-i} \frac{d\mu^{L-i}}{dt} + \bar{S}^L \frac{d\theta^L}{dt} + \bar{V}^L \frac{d\sigma^L}{dt} + \bar{V}_0^L \frac{d\underline{s}^L}{dt} = 0. \quad (3.12)$$

Now writing (3.9) and (3.10) for liquid and substituting them into (3.12) we obtain

$$\begin{aligned} \bar{N}^{L-H_2O} \frac{d\mu^{L-H_2O}}{dt} + \sum_{i=1}^n \bar{N}^{L-i} \frac{d\mu^{L-i}}{dt} + \bar{V}_0^L \frac{d\sigma^L}{dt} + \bar{V}_0^L \frac{\sigma^L}{K^L} \frac{d\sigma^L}{dt} + 3\alpha^L (\theta^L - \theta_m^L) \bar{V}_0^L \frac{d\sigma^L}{dt} \\ + \bar{V}_0^L \frac{s^L}{2G^L} \frac{ds^L}{dt} + \bar{S}_0^L \frac{d\theta^L}{dt} = 0 \end{aligned} \quad (3.13)$$

If we consider a salt with chemical composition of  $A_{\beta^1} B_{\beta^2} C_{\beta^3} \cdot \beta^{H_2O} (H_2O)$  [28],

then the chemical potential of the solute ( $\mu^{L-S}$ ) in the liquid phase can be written as the sum of the chemical potentials of the species forming it

$$\mu^{L-S} = \sum_{i=1}^n \beta^i \mu^{L-i} + \beta^{H_2O} \mu^{H_2O} \quad (3.14)$$

where  $i$  represents the species other than  $H_2O$  (i.e. A, B, and C), and  $\beta^{H_2O}$  is the number of molecules of water that are chemically bound to the hydrated salt. When the salt

concentration in the pore solution reaches supersaturation, these water molecules are removed from the solvent with the salt crystal and do not contribute to the ice volume.

For a non-hydrated salt, e.g. NaCl,  $\beta^{\text{H}_2\text{O}} = 0$ .

Equation (3.14) can be rearranged to provide the chemical potentials of the dissolved species (excluding the hydrated water molecules) in the liquid phase as

$$\mu^{L-i} = \frac{\mu^{L-S}}{\sum_{i=1}^n \beta^i} - \frac{\beta^{\text{H}_2\text{O}} \mu^{L-\text{H}_2\text{O}}}{\sum_{i=1}^n \beta^i} = \frac{\mu^{L-S}}{B} - \frac{\beta^{\text{H}_2\text{O}} \mu^{L-\text{H}_2\text{O}}}{B}, \quad (3.15)$$

where

$$B = \sum_{i=1}^n \beta^i. \quad (3.16)$$

Substituting (3.15) into (3.13), we write

$$\begin{aligned} & (\bar{N}^{L-\text{H}_2\text{O}} - x \beta^{\text{H}_2\text{O}}) \frac{d \mu^{L-\text{H}_2\text{O}}}{dt} + x \frac{d \mu^{L-S}}{dt} + \bar{V}_0^L \frac{d \sigma^L}{dt} + \bar{V}_0^L \frac{\sigma^L}{K^L} \frac{d \sigma^L}{dt} + \\ & 3 \alpha^L (\theta^L - \theta_m^L) \bar{V}_0^L \frac{d \sigma^L}{dt} + \bar{V}_0^L \frac{s^L}{2G^L} \frac{d s^L}{dt} + \bar{S}_0^L \frac{d \theta^L}{dt} = 0 \end{aligned}, \quad (3.17)$$

where we introduced,

$$x = \frac{\bar{N}^{L-i}}{\beta^i} = \frac{\sum_{i=1}^n \bar{N}^{L-i}}{\sum_{i=1}^n \beta^i}, \quad (3.18)$$

such that

$$\bar{N}^{L-\text{H}_2\text{O}} = 1 - B x, \quad (3.19)$$

Rewriting (3.17) with the help of (3.19), we find

$$\begin{aligned}
& (1 - Bx - x\beta^{\text{H}_2\text{O}}) \frac{d\mu^{L-\text{H}_2\text{O}}}{dt} + x \frac{d\mu^{L-S}}{dt} + \bar{V}_0^L \frac{d\sigma^L}{dt} \\
& + \bar{V}_0^L \frac{\sigma^L}{K^L} \frac{d\sigma^L}{dt} + 3\alpha^L (\theta^L - \theta_m^L) \bar{V}_0^L \frac{d\sigma^L}{dt} + \bar{V}_0^L \frac{s^L}{2G^L} \frac{ds^L}{dt} + \bar{S}_0^L \frac{d\theta^L}{dt} = 0
\end{aligned} \tag{3.20}$$

At equilibrium, not only do we consider the rate of energy to be zero, but we will also enforce a stronger statement of the second law by forcing the chemical potentials of the chemically dependent phases to be equal such that

$$\frac{d\mu^{L-\text{H}_2\text{O}}}{dt} = \frac{d\mu^{C-\text{H}_2\text{O}}}{dt} \tag{3.21}$$

Thus, (3.11) and (3.20) can be combined to yield

$$\begin{aligned}
& (1 - Bx - x\beta^{\text{H}_2\text{O}}) \left( \begin{aligned} & -\frac{1}{\bar{N}^{C-\text{H}_2\text{O}}} \sum_{i=1}^n \bar{N}^{C-i} \frac{d\mu^{C-i}}{dt} - \frac{\bar{V}_0^C}{\bar{N}^{C-\text{H}_2\text{O}}} \frac{d\sigma^C}{dt} \\ & -\frac{\bar{V}_0^C}{\bar{N}^{C-\text{H}_2\text{O}}} \frac{\sigma^C}{K^C} \frac{d\sigma^C}{dt} - 3\alpha^C (\theta^C - \theta_m^C) \frac{\bar{V}_0^C}{\bar{N}^{C-\text{H}_2\text{O}}} \frac{d\sigma^C}{dt} \\ & -\frac{\bar{V}_0^C}{\bar{N}^{C-\text{H}_2\text{O}}} \frac{s^C}{2G^C} \frac{ds^C}{dt} - \frac{\bar{S}_0^C}{\bar{N}^{C-\text{H}_2\text{O}}} \frac{d\theta^C}{dt} \end{aligned} \right) \\
& + x \frac{d\mu^{L-S}}{dt} + \bar{V}_0^L \frac{d\sigma^L}{dt} + \bar{V}_0^L \frac{\sigma^L}{K^L} \frac{d\sigma^L}{dt} + 3\alpha^L (\theta^L - \theta_m^L) \bar{V}_0^L \frac{d\sigma^L}{dt} \\
& + \bar{V}_0^L \frac{s^L}{2G^L} \frac{ds^L}{dt} + \bar{S}_0^L \frac{d\theta^L}{dt} = 0
\end{aligned} \tag{3.22}$$

Now, evaluating the chemical potential of the solute,

$$\frac{d\mu^{L-S}}{dt} = \frac{d\mu_*^{L-S}}{dt} + R\theta \frac{d \ln a^{L-S}}{dt}, \tag{3.23}$$

at the same pressure and temperature at the solution, we have

---

<sup>1</sup> The process is considered fully reversible since the rate of change of temperature is assumed to be slow enough to maintain a local state of near equilibrium.

$$\begin{aligned} \frac{d\mu^{L-S}}{dt} = & -\bar{V}_0^{\text{solute}} \frac{d\sigma^L}{dt} - \bar{V}_0^{\text{solute}} \frac{\sigma^L}{K^{\text{solute}}} \frac{d\sigma^L}{dt} - 3\alpha^{\text{solute}} (\theta^L - \theta_m^L) \bar{V}_0^{\text{solute}} \frac{d\sigma^L}{dt} \\ & - \frac{\bar{V}_0^{\text{solute}}}{2G^{\text{solute}}} \underline{s}^L : \frac{d\underline{s}^L}{dt} - \bar{S}_0^{\text{solute}} \frac{d\theta^L}{dt} + R\theta \frac{d \ln a^{L-\text{solute}}}{dt} \end{aligned} \quad (3.24)$$

Here,  $R$  is the ideal gas constant. Similarly chemical potential of the salt crystal is given by

$$\begin{aligned} \frac{d\mu^{C-i}}{dt} = & -\bar{V}_0^{C-i} \frac{d\sigma^C}{dt} - \bar{V}_0^{C-i} \frac{\sigma^C}{K^{C-i}} \frac{d\sigma^C}{dt} - 3\alpha^{C-i} (\theta^C - \theta_m^C) \bar{V}_0^{C-i} \frac{d\sigma^C}{dt} \\ & - \frac{\bar{V}_0^{C-i}}{2G^{C-i}} \underline{s}^C : \frac{d\underline{s}^C}{dt} - \bar{S}_0^{C-i} \frac{d\theta^C}{dt} \end{aligned} \quad (3.25)$$

where, the activity of the pure salt crystal equals one. Now we impose that the gradient in the strain energy or stress power across the crystal is negligible such that no preferential dissolution and precipitation occurs. Furthermore, we speculate that the normal stresses in the crystal are significantly higher than the deviatoric components. Hence, it is justifiable for us to assume that the crystal is subjected to a purely hydrostatic state of stress nullifying the shear contribution. However, the same treatment cannot be exercised with the liquid water due to the repulsive force originated from the crystal-pore wall interface incompatibility. Consequently, crystals can repel the pore wall across the thin film and exert an excess pressure. Due to this repulsive force, conservation of linear momentum requires shear stresses in the liquid film. Because of this shear and owing to the pressure gradient between the film and the bulk liquid, the liquid will tend to flow away from the interface to alleviate the excess pressure. However, due to the drastic transition from liquid like to solid like responses, mobility of the film reduces by orders of magnitude compared to the diffusion of the bulk water [32,

33]. Therefore, the liquid film between the crystal and the pore wall has to be treated as a non-Newtonian fluid capable of transmitting shear stresses. The associated strain energy term thus cannot be overlooked. With some mathematical manipulation, substitution of (3.24) and (3.25) in (3.22) provides

$$\begin{aligned} \frac{d\sigma^C}{dt} &= \frac{(\bar{V}_0^L - x\bar{V}_0^{\text{solute}})}{\bar{V}_{0-n}^C} \frac{d\sigma^L}{dt} + \frac{1}{\bar{V}_{0-n}^C} \left( \frac{\bar{V}_0^L}{G^L} - \frac{x\bar{V}_0^{\text{solute}}}{G^{\text{solute}}} \right) \frac{s^L}{2} \cdot \frac{ds^L}{dt} \\ &+ \frac{\Delta\bar{S}}{\bar{V}_{0-n}^C} \frac{d\theta}{dt} + R\theta \frac{\bar{N}^{C-\text{H}_2\text{O}}}{\left( \bar{V}_0^C - \sum_{i=1}^n \bar{N}^{C-i} \bar{V}_0^{C-i} \right) (1 - Bx - x\beta^{\text{H}_2\text{O}})} \frac{x}{dt} \frac{d \ln a^{L-\text{solute}}}{dt}, \end{aligned} \quad (3.26)$$

where the terms,

$$\bar{V}_{0-n}^C = (1 - Bx - x\beta^{\text{H}_2\text{O}}) \frac{\left( \bar{V}_0^C - \sum_{i=1}^n \bar{N}^{C-i} \bar{V}_0^{C-i} \right)}{\bar{N}^{C-\text{H}_2\text{O}}} \quad \text{and} \quad (3.27)$$

$$\Delta\bar{S} = (\bar{S}_0^L - x\bar{S}_0^{\text{solute}}) - (1 - Bx - x\beta^{\text{H}_2\text{O}}) \frac{\left( \bar{S}_0^C - \sum_{i=1}^n \bar{N}^{C-i} \bar{S}_0^{C-i} \right)}{\bar{N}^{C-\text{H}_2\text{O}}} \quad (3.28)$$

are used. If no salt precipitates ( $\bar{N}^{C-\text{H}_2\text{O}} = 1$  and  $\sum_{i=1}^n \bar{N}^{C-i} = 0$ ) then

$$\bar{V}_{0-n}^C = (1 - Bx - x\beta^{\text{H}_2\text{O}}) \bar{V}_0^C \quad \text{and} \quad \Delta\bar{S} = (\bar{S}_0^L - x\bar{S}_0^{\text{solute}}) - (1 - Bx - x\beta^{\text{H}_2\text{O}}) \bar{S}_0^C. \quad \text{In addition,}$$

if there is no dissolved salt present in the pore solution, then (3.27) and (3.28) simplify to

$$\bar{V}_{0-n}^C = \bar{V}_0^C \quad \text{and} \quad \Delta\bar{S} = \bar{S}_0^L - \bar{S}_0^C, \quad \text{respectively. Thus, } \bar{V}_{0-n}^C \text{ refers to the net molar volume of}$$

the ice crystal (excluding the molar volume of the salt crystal), and  $\Delta\bar{S}$  denotes the

change in molar entropy due to fusion. Here, we ignored the higher order stress terms

and the entropic term related to the thermal dilation. We also assumed that the liquid and

crystal are subjected to the same temperature  $\theta^L = \theta^C = \theta$ . Equation (3.26) illustrates that the mean stress in the crystal varies as a function of stresses in the liquid, temperature, and ionic activity in the solution. Now it is convenient for us to select the reference state as the state where  $\sigma^C = \sigma^L = \sigma_0$ , so that the related temperature is  $\theta = \theta_m$  and the molar fraction of salt is  $x = x_0$ . Integrating (3.26) from this reference state to a current state where  $\sigma^C \neq \sigma^L$ ,  $\theta = \theta$ , and  $x = x_f$  we find

$$\begin{aligned} \sigma^C - \sigma_0 = & \frac{(\bar{V}_0^L - x \bar{V}_0^{\text{solute}})}{\bar{V}_{0-n}^C} (\sigma^L - \sigma_0) + \frac{(\bar{V}_0^L - x \bar{V}_0^{\text{solute}})}{\bar{V}_{0-n}^C} \left( \frac{\bar{V}_0^L}{4G^L} - \frac{x \bar{V}_0^{\text{solute}}}{4G^{\text{solute}}} \right) \underline{\underline{S}}^L : \underline{\underline{S}}^L \\ & + \frac{\Delta \bar{S}}{\bar{V}_{0-n}^C} (\theta - \theta_m) + R \theta \frac{\bar{N}^{C-\text{H}_2\text{O}}}{\left( \bar{V}_0^C - \sum_{i=1}^n \bar{N}^{C-i} \bar{V}_0^{C-i} \right)} \int_{x_0}^{x_f} \frac{x}{(1 - Bx - x\beta^{\text{H}_2\text{O}})} d \ln a^{L-\text{solute}}. \end{aligned} \quad (3.29)$$

Here we also assume that the ice and salt crystals precipitate as pure substances. The last term of (3.29) calculates the change in crystal pressure due to the change in salt concentration with respect to the reference configuration,  $x = x_0$ . In this study we wish to calculate pore freezing depression due to the presence of dissolved ions. Thus we select the reference state as the state such that it corresponds to the pure water, i.e.  $x_0 = 0$ . If one wants to link the crystal pressure to the supersaturation [28, 76, 77], then the molar fraction related to the salt solubility could be chosen as the reference state. And so, when  $x_f$  is greater than  $x_0$ , the solution becomes supersaturated, and the corresponding crystal pressure accounts for the salt crystallization due to the removal of solvent with decreasing temperatures.

At this point, it is important to accurately determine the ionic activity in the pore solution. One can utilize Pitzer's equations [78, 79] to analyze ionic activity with a high degree of accuracy. However, implementation of such complex relations complicates the integral term. At low concentrations, the mixture can be treated as ideal, and the activity coefficient approaches to unity. Moreover, most cementitious materials do not contain very high concentrations of dissolved species, and ideal solution approximation yields an accurate measure of ionic activity for saturations down to 0.5 [80]. Therefore, The ionic activity in the last term of (3.29) can be approximated as  $a^{L-\text{solute}} \approx Bx$ , such that,

$$\begin{aligned} \sigma^C - \sigma_0 = & \frac{(\bar{V}_0^L - x\bar{V}_0^{\text{solute}})}{\bar{V}_{0-n}^C} (\sigma^L - \sigma_0) + \frac{(\bar{V}_0^L - x\bar{V}_0^{\text{solute}})}{\bar{V}_{0-n}^C} \left( \frac{\bar{V}_0^L}{4G^L} - \frac{x\bar{V}_0^{\text{solute}}}{4G^{\text{solute}}} \right) \underline{\underline{s}}^L : \underline{\underline{s}}^L \\ & + \frac{\Delta\bar{S}}{\bar{V}_{0-n}^C} (\theta - \theta_m) - R\theta \frac{\bar{N}^{C-\text{H}_2\text{O}}}{\left( \bar{V}_0^C - \sum_{i=1}^n \bar{N}^{C-i} \bar{V}_0^{C-i} \right)} \frac{1}{(B + \beta^{\text{H}_2\text{O}})} \ln \frac{(1 - Bx_f - \beta^{\text{H}_2\text{O}} x_f)}{(1 - Bx_0 - \beta^{\text{H}_2\text{O}} x_0)}. \end{aligned} \quad (3.30)$$

As uniform pressure subsists everywhere in the crystal, we state that  $\sigma^C = -p^C$ .

Furthermore, if we neglect the repulsive force across the thin film around the crystal so that spherical stress state is achieved in liquid with  $\sigma^L = -p^L$  and  $\underline{\underline{s}}^L = 0$ , (3.30)

simplifies to

$$\begin{aligned} -p^C + p_0 = & -\frac{(\bar{V}_0^L - x\bar{V}_0^{\text{solute}})}{\bar{V}_{0-n}^C} (p^L - p_0) + \frac{\Delta\bar{S}}{\bar{V}_{0-n}^C} (\theta - \theta_m) \\ & - R\theta \frac{\bar{N}^{C-\text{H}_2\text{O}}}{\left( \bar{V}_0^C - \sum_{i=1}^n \bar{N}^{C-i} \bar{V}_0^{C-i} \right)} \frac{1}{(B + \beta^{\text{H}_2\text{O}})} \ln \frac{(1 - Bx_f - \beta^{\text{H}_2\text{O}} x_f)}{(1 - Bx_0 - \beta^{\text{H}_2\text{O}} x_0)}, \end{aligned} \quad (3.31)$$

where we also assume that the reference state,  $\sigma_0 = -p_0$ . In addition, if we consider that at no point the salt concentration exceeds its solubility, and thus salt precipitation does

not occur, then  $\sum_{i=1}^n \bar{N}^{C-i} = 0$  and  $\bar{N}^{C-H_2O} = 1$ , such that

$$\begin{aligned}
p^C - p_0 &= \frac{(\bar{V}_0^L - x \bar{V}_0^{\text{solute}})}{(1 - Bx - x\beta^{\text{H}_2\text{O}}) \bar{V}_0^C} (p^L - p_0) \\
&+ \frac{(\bar{S}_0^L - x \bar{S}_0^{\text{solute}}) - (1 - Bx - x\beta^{\text{H}_2\text{O}}) \bar{S}_0^C}{(1 - Bx - x\beta^{\text{H}_2\text{O}}) \bar{V}_0^C} (\theta_m - \theta). \\
&+ R\theta \frac{1}{\bar{V}_0^C (B + \beta^{\text{H}_2\text{O}})} \ln \frac{(1 - Bx_f - \beta^{\text{H}_2\text{O}} x_f)}{(1 - Bx_0 - \beta^{\text{H}_2\text{O}} x_0)}
\end{aligned} \tag{3.32}$$

The last term in (3.32) accounts for the contribution of dissolved ions on the freezing point suppression of the pore solution. Furthermore, if we ignore the presence of dissolved species, i.e.  $x_f = 0$ , then (3.32) becomes

$$p^C - p_0 = \frac{\bar{V}_0^L}{\bar{V}_0^C} (p^L - p_0) + \frac{(\bar{S}_0^L - \bar{S}_0^C)}{\bar{V}_0^C} (\theta_m - \theta), \tag{3.33}$$

with  $\bar{S}_0^L$  and  $\bar{S}_0^C$  now being the molar entropy of pure liquid water and ice, respectively.

The above equation can be rearranged to read

$$p^C - p^L = - \left( 1 - \frac{\bar{V}_0^L}{\bar{V}_0^C} \right) (p^L - p_0) + \Sigma_m (\theta_m - \theta). \tag{3.34}$$

Equation (3.34) is known as the renowned Thomson's equation, where

$$\Sigma_m = \frac{(\bar{S}_0^L - \bar{S}_0^C)}{\bar{V}_0^C} \tag{3.35}$$

is the melting entropy. In terms of liquid and crystal densities, (3.34) equivalents to

$$p^C - p^L = -\left(1 - \frac{\rho^C}{\rho^L}\right)(p^L - p_0) + \sum_m (\theta_m - \theta), \quad (3.36)$$

where  $\rho^C$  and  $\rho^L$  denote the density of the crystal and liquid, respectively.

### 3.2 Governing equations

In the present section, governing equations associated with the mass balance, energy balance, and linear momentum balance for thermoelastic porous materials are provided. Omitting inertia and body forces, the conservation of linear momentum can be denoted by

$$\text{div} \underline{\underline{T}} = 0, \quad (3.37)$$

where  $\underline{\underline{T}}$  represents the externally applied total Cauchy stress tensor and is expressed

(for a linearly isotropic material) as

$$\underline{\underline{T}} = 2G \left[ \underline{\underline{\varepsilon}} + \frac{\nu}{1 - 2\nu} \text{tr}(\underline{\underline{\varepsilon}}) \underline{\underline{I}} \right] - 3K \varepsilon_f \underline{\underline{I}}. \quad (3.38)$$

Here,  $\underline{\underline{\varepsilon}}$  is the infinitesimal strain tensor,  $G$  is the shear modulus of the porous body,  $K$  is the bulk modulus of the porous body,  $\nu$  is the Poisson's ratio of the porous body,  $\underline{\underline{I}}$  is the identity tensor, and  $\varepsilon_f$  is the free strain.

If the fluid and solid temperatures are assumed to achieve equilibrium locally, the governing equation for heat transfer, assuming linearity and isotropy, is given by

$$\frac{\partial \theta}{\partial t} = \kappa \text{div}(\text{grad} \theta), \quad (3.39)$$

where  $\kappa$  is thermal diffusivity and is related to the thermal conductivity,  $\wp$ , through

$$\kappa = \frac{\wp}{\rho C_p}. \text{ Here, } \rho \text{ is the density and } C_p \text{ is the specific heat capacity (at constant}$$

pressure), and  $\theta$  is the temperature. Equation (3.39) is a highly simplified energy balance equation where heat flux associated with the pressure gradient, as well as latent heat due to skeletal and fluid expansion and phase transition are neglected. A detailed discussion of the above effects along with the complete energy balance are provided by McTigue and Coussy [35, 81].

Finally, using the mass balance equation along with Darcy's law we can write

$$\frac{1}{\rho^L} \frac{dm_w}{dt} = \frac{k}{\eta^L} \text{div}(\text{grad}p^L), \quad (3.40)$$

where  $\rho^L$  is the undeformed density of the liquid phase,  $k$  is the intrinsic permeability with dimensions of length squared,  $\eta^L$  is the viscosity of the pore liquid,  $p^L$  denotes the pore liquid pressure, and  $m_w$  stands for the total mass of water currently present in all forms (both liquid and solid – vapor mass is neglected) per unit initial volume of the porous material.

Adopting appropriate boundary conditions applicable to a specific problem, equation (3.39) can be solved independently for  $\theta$ , whereas coupled equations (3.37) and (3.40) need to be solved simultaneously to determine the unknowns,  $\underline{\underline{T}}$  and  $p^L$ .

### 3.3 Poroelasticity

For determining freezing deformation of fully saturated concrete, we now consider a porous material whose initial pore space is completely filled with liquid

water. For a poroelastic material (with invariant porosity upon pressurization) exposed to variable temperature,  $\varepsilon_f$  in equation (3.38) can be referred as

$$\varepsilon_f = \frac{b p^L}{3K} - \alpha \Delta\theta, \quad (3.41)$$

where  $\alpha$  is the linear CTE of the porous body and  $\Delta\theta = \theta_m - \theta$  is the change in temperature measured with respect to the melting temperature  $\theta_m$ , with  $\theta$  being the current temperature<sup>2</sup>. The term  $b$  is Biot's coefficient and can be written as

$$b = 1 - \frac{K}{K_s}, \quad (3.42)$$

where  $K_s$  is the bulk modulus of the solid phase comprising the skeleton of the porous body. If temperature is reduced below the melting point at constant relative humidity, solid crystals gradually invade the pore network. For such a case where the pore network is partially occupied by the ice crystals, the free strain in (3.41) can be extended to

$$\varepsilon_f = \frac{b^C p^C + b^L p^L - 3K\alpha\Delta\theta}{3K}, \quad (3.43)$$

and, according to [1, 41, 42], mass of water per unit initial volume of the porous body associated with (3.40) can be quantified as

$$m_w = \rho^L \phi_o + \rho^L (\mathcal{G}_{\Delta\rho} + \mathcal{G}_\varphi), \quad (3.44)$$

where  $\phi_o$  represents the initial porosity of the porous material while

---

<sup>2</sup> We choose melting temperature as the reference temperature, and do not consider thermal strain due to cooling from ambient temperature to the melting temperature.

$$\mathfrak{g}_{\Delta\rho} = \left( \frac{\rho^C}{\rho^L} - 1 \right) \phi_o S^C = \left( \frac{\bar{V}_0^L}{\bar{V}_0^C} - 1 \right) \phi_o S^C, \quad (3.45)$$

and

$$\mathfrak{g}_\varphi = b \varepsilon_{kk} + \frac{p^L}{M^L} + \frac{p^C}{M^C} + 3 \left( \phi_o S^L \alpha^L + \phi_o S^C \alpha^C + \varpi^L + \varpi^C \right) \Delta\theta, \quad (3.46)$$

with

$$\frac{1}{M^J} = \frac{b^J - \phi_o S^J}{K_s} + \frac{\phi_o S^J}{K^J}, \text{ and} \quad (3.47)$$

$$\frac{1}{M} = \frac{1}{M^C} + \frac{1}{M^L}. \quad (3.48)$$

Here, solid crystals and liquid water are referred to by the superscript  $J=C$  and  $J=L$ , respectively. The terms  $b^J$ ,  $M^J$ ,  $\rho^J$ , and  $K^J$  are the Biot's coefficient, Biot's modulus, density, and bulk modulus of the phase  $J$ , respectively.  $S^J$  indicates the volume fraction of the pores occupied by phase  $J$  satisfying the constraint

$$\sum_{J=C,L} S^J = 1. \quad (3.49)$$

The parameter  $\alpha^J$  stands for the linear CTE of the phase  $J$ . Additionally,

$$\sum_{J=C,L} b^J = b^C + b^L = b, \quad (3.50)$$

along with

$$b^J = S^J b. \text{ Finally,} \quad (3.51)$$

$$\varpi^J = \alpha \left( b^J - \phi_o S^J \right). \quad (3.52)$$

Here,  $\varpi^J$  is the coefficient related to the thermal expansion of the pore space occupied by the phase  $J$ .

Equation (3.40) needs to be solved for  $p^L$ , with  $p^C$  being determined in terms of  $p^L$  from the thermodynamic equilibrium equation of the crystal-liquid interface expressed by any of the forms given by (3.30), (3.32), and (3.34).

Once  $p^C$  and  $p^L$  are known, freezing strain exhibited by a fully saturated concrete can be calculated using equation (3.43). Substitution of  $\varepsilon_f$  into (3.38) along with the appropriate boundary condition provides solution for (3.37), which can then be used to determine  $\varepsilon_{kk}$ . Subsequently,  $\varepsilon_{kk}$  needs to be replaced in (3.46) to calculate the new  $p^L$  and other variables.

Throughout this dissertation, the following sign convention is used:

- Pore pressure (liquid or crystal) is positive for compression and negative for suction or tension.
- Stress and strain are positive for tension and negative for compression.
- Change in temperature,  $\Delta\theta = \theta_m - \theta$ , is positive for cooling and negative for heating, and measured with respect to the melting temperature  $\theta_m$ . Here,  $\theta$  is the actual temperature.

### 3.4 Summary

In this section, the present theory of poroelasticity has been advanced to include the effect of pore solution speciation and disjoining pressure on the deformation of porous media subjected to freezing temperatures. Table 2 summarizes the liquid-crystal

thermodynamic equilibrium relationships and governing equations of thermoporoelasticity of porous media exposed to freezing temperatures. Choice of the particular form of liquid-crystal thermodynamic equation will vary depending on the nature of the problem.



## 4 IDENTIFYING D-CRACKING SUSCEPTIBLE AGGREGATES<sup>3</sup>

Frost deterioration in concrete pavement is often attributed to aggregates with substandard properties. A poromechanical composite model is developed to predict time-dependent stress and strain fields in freezing concrete containing aggregates with undesirable combinations of geometry and constitutive properties. The model, presented in section 4.1, indicates that for both air-entrained and non-air-entrained concrete, destructive tensile stress may be triggered at the aggregate-matrix boundary. The severity of the damage is enhanced by the Mandel-Cryer effect as explained in section 4.2. Section 4.4 analyzes the sensitivity of stress and strain fields to the aggregate and matrix constitutive parameters and environmental exposure to suggest improved concrete mixture design for the construction of durable concrete pavement.

### 4.1 Model

A model concrete sphere is considered with a coarse aggregate core of radius  $R_i$  embedded inside a mortar or cement paste matrix shell (throughout this report, the term “aggregate” and “matrix” will be used to represent the coarse aggregate core, and the paste or mortar shell, respectively) of outer radius  $R_o$ , as shown in Figure 2. An elastic model incorporating free strains is first developed based on the classical elastic theory proposed by Timoshenko and Goodier [82] It is then extended to include poromechanical constitutive properties based on the theory developed by Biot [34] and

---

<sup>3</sup> Reprinted with permission from Rahman, S. and Z. Grasley, *A poromechanical model of freezing concrete to elucidate damage mechanisms associated with substandard aggregates*. Cement and Concrete Research, 2014. **55**: p. 88-101. Copyright 2013 Elsevier.

discussed by Coussy [1, 35], and Coussy and Monteiro [41, 42]. The linearly elastic case considering a general ‘free strain’ is presented in section 4.1.1, and then specifically refined for the case of unsaturated poroelasticity in section 4.1.2.

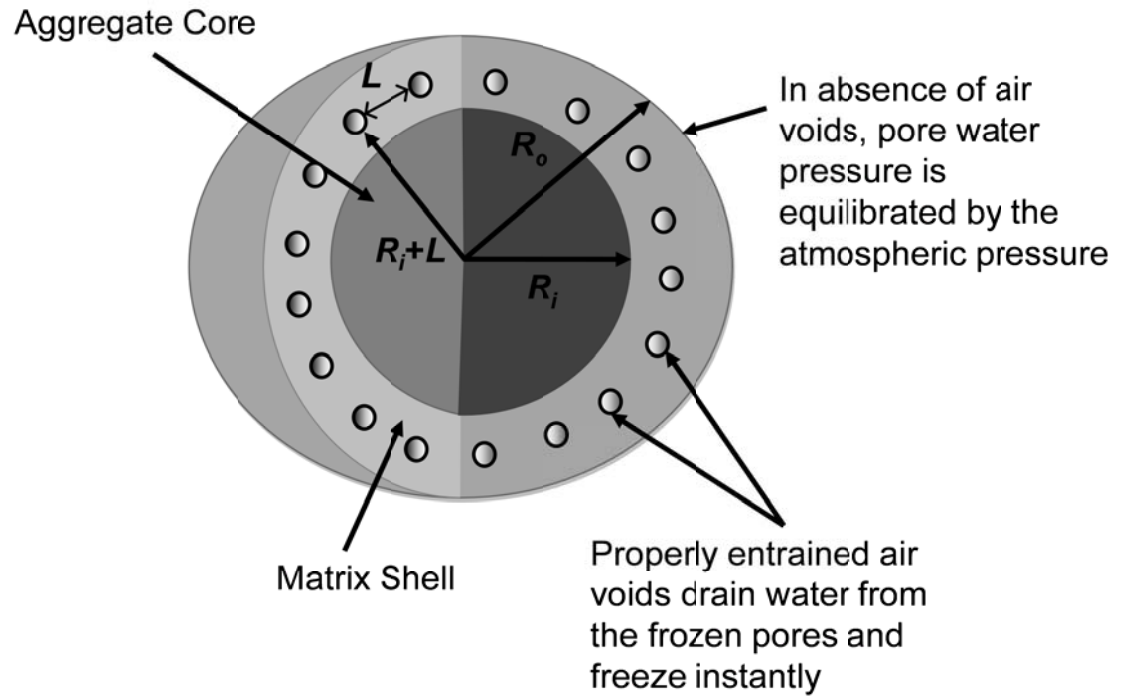


**Figure 2. Geometry of the proposed model representing a coarse aggregate core of radius  $R_i$  embedded in a cement paste or mortar matrix shell of outer radius  $R_o$ . In case of air-entrained concrete, uniformly distributed air bubbles are considered with a spacing of  $L$ .**

#### 4.1.1 Elastic material

Determination of the stress and strain components given in this section follows much of Timoshenko and Goodier’s work [82], with the only exception being that thermal strain is replaced by the more general ‘free strain.’ A simple case of a temperature symmetrical with respect to the center, and a function of radius,  $r$ , is considered. On account of the spherical symmetry, the non-zero radial deformation ( $u_r$ )

of the aggregate (denoted by superscript  $a$ ) along with the radial (subscript  $r$ ) and two tangential stress and strain components (subscript  $t$ ) in the principal directions are obtained by solving the conservation of linear momentum equation, (3.37), for spherical coordinate system whereby,

$$u_r^a = \frac{(1+\nu^a)}{(1-\nu^a)} \frac{1}{r^2} \int_{r=0}^{r=r} \varepsilon_f^a r^2 dr + C_1^a r, \quad (4.1)$$

$$\varepsilon_r^a = -2 \frac{(1+\nu^a)}{(1-\nu^a)} \frac{1}{r^3} \int_{r=0}^{r=r} \varepsilon_f^a r^2 dr + \frac{(1+\nu^a)}{(1-\nu^a)} \varepsilon_f^a + C_1^a, \quad (4.2)$$

$$\varepsilon_t^a = \frac{(1+\nu^a)}{(1-\nu^a)} \frac{1}{r^3} \int_{r=0}^{r=r} \varepsilon_f^a r^2 dr + C_1^a, \quad (4.3)$$

$$\sigma_r^a = -6K^a \frac{(1-2\nu^a)}{(1-\nu^a)} \frac{1}{r^3} \int_{r=0}^{r=r} \varepsilon_f^a r^2 dr + 3K^a C_1^a, \quad (4.4)$$

and

$$\sigma_t^a = 3K^a \frac{(1-2\nu^a)}{(1-\nu^a)} \frac{1}{r^3} \int_{r=0}^{r=r} \varepsilon_f^a r^2 dr - 3K^a \frac{(1-2\nu^a)}{(1-\nu^a)} \varepsilon_f^a + 3K^a C_1^a. \quad (4.5)$$

where,  $K$  and  $\nu$  are the bulk modulus and the Poisson's ratio of the isotropic linear elastic porous material, and  $\varepsilon_f$  is the free strain and a function of pore pressure and

temperature. Here we also defined that  $\sigma_r = T_{11}$  and  $\sigma_t = T_{22} = T_{33}$ . For paste or mortar

matrix, we write  $u_r, \varepsilon_r, \varepsilon_t, \sigma_r,$  and  $\sigma_t$  with superscript  $p$  as

$$u_r^p = \frac{(1+\nu^p)}{(1-\nu^p)} \frac{1}{r^2} \int_{r=R_i}^{r=r} \varepsilon_f^p r^2 dr + C_1^p r + \frac{C_2^p}{r^2}, \quad (4.6)$$

$$\varepsilon_r^p = -2 \frac{(1+\nu^p)}{(1-\nu^p)} \frac{1}{r^3} \int_{r=R_i}^{r=r} \varepsilon_f^p r^2 dr + \frac{(1+\nu^p)}{(1-\nu^p)} \varepsilon_f^p + C_1^p - \frac{2C_2^p}{r^3}, \quad (4.7)$$

$$\varepsilon_t^p = \frac{(1+\nu^p)}{(1-\nu^p)} \frac{1}{r^3} \int_{r=R_i}^{r=r} \varepsilon_f^p r^2 dr + C_1^p + \frac{C_2^p}{r^3}, \quad (4.8)$$

$$\sigma_r^p = -6K^p \frac{(1-2\nu^p)}{(1-\nu^p)} \frac{1}{r^3} \int_{r=R_i}^{r=r} \varepsilon_f^p r^2 dr + 3K^p C_1^p - \frac{(1-2\nu^p)}{(1+\nu^p)} \frac{6K^p}{r^3} C_2^p, \quad (4.9)$$

and

$$\begin{aligned} \sigma_t^p &= 3K^p \frac{(1-2\nu^p)}{(1-\nu^p)} \frac{1}{r^3} \int_{r=R_i}^{r=r} \varepsilon_f^p r^2 dr - 3K^p \frac{(1-2\nu^p)}{(1-\nu^p)} \varepsilon_f^p + 3K^p C_1^p \\ &+ \frac{(1-2\nu^p)}{(1+\nu^p)} \frac{3K^p}{r^3} C_2^p \end{aligned} \quad (4.10)$$

The three unknown integration constants,  $C_1^a$ ,  $C_1^p$ , and  $C_2^p$ , are determined using the following three boundary conditions:

- At the aggregate core-matrix shell interface ( $r=R_i$ ), radial displacement and radial stress are the same in the matrix and aggregate, so:

$$\left[ u_r^a \right]_{r=R_i} = \left[ u_r^p \right]_{r=R_i} \text{ in order to ensure a continuous displacement field, and } (4.11)$$

$$\left[ \sigma_r^a \right]_{r=R_i} = \left[ \sigma_r^p \right]_{r=R_i} \text{ to satisfy static, mechanical equilibrium. } (4.12)$$

- At the outer surface ( $r=R_o$ ) of the matrix shell, radial stress,  $\sigma_r^p$ , is equal to the applied stress,  $\sigma_{app}$ , so:

$$\left[ \sigma_r^p \right]_{r=R_o} = \sigma_{app}. \quad (4.13)$$

Substituting the integration constants in the equation for bulk strain,

$\varepsilon_{kk} = \varepsilon_r + 2\varepsilon_t$ , for the aggregate core, we obtain

$$\varepsilon_{kk}^a = X \langle \varepsilon_f^a \rangle + 3\beta \varepsilon_f^a + W \langle \varepsilon_f^p \rangle - \frac{p_{app} R_o^3}{Z} (1 + 2\chi_p^p), \quad (4.14)$$

and for matrix shell

$$\varepsilon_{kk}^p = U \langle \varepsilon_f^a \rangle + 3\beta^p \varepsilon_f^p + V \langle \varepsilon_f^p \rangle - \frac{p_{app} R_o^3}{Z} \frac{(K^a + 2K^p \chi^p)}{K^p}, \quad (4.15)$$

where the angle brackets indicate a volumetric average, such that for a sphere or spherical shell

$$\langle x \rangle = \frac{3}{b^3 - a^3} \int_a^b x(r) r^2 dr. \quad (4.16)$$

Superscripts  $a$  and  $p$  denote aggregate and matrix, respectively. Coefficients  $\beta$ ,  $\chi$ ,  $U$ ,  $V$ ,  $W$ ,  $X$ , and  $Z$  are functions of material constitutive properties and are given in APPENDIX A. For the aggregate, the lower limit  $a$  of the integral is substituted by  $r=0$ , and upper limit,  $b$  is substituted by  $r=R_i$ . Whereas, for the matrix shell,  $a$  and  $b$  are replaced by  $r=R_i$  and  $r=R_o$ , respectively.

#### 4.1.2 Unsaturated poroelastic materials

The fundamental equations needed to model the deformations in concrete exposed to freezing conditions, including thermal effects, hydraulic pressure, and cryo-suction have already been developed by Coussy [35] and Coussy and Monteiro [41, 42]. These equations are modified to determine the stress and strain fields in concrete

caused by the porous aggregates under freeze-thaw cycles. For simplicity, the following assumptions are made:

- We assume that the rate of thermal equilibration is orders of magnitude faster than the fluid flux such that a uniform temperature field in our model is a reasonable approximation. As fast cooling will be shown to lead to greater stresses, the assumption of rapid thermal equilibration is deemed acceptable for the investigation of damage mechanisms, since damage is more likely with faster cooling.
- Damage accretion with each successive freeze-thaw cycle and subsequent changes in poromechanical properties (e.g., permeability, Biot's coefficient and modulus, bulk modulus) are also neglected. In this study, the focus is strictly on stress magnitude during a single cooling event.

The mass conservation law (3.40) for spherical coordinate system takes the form

$$\frac{1}{\rho^L} \frac{dm_w}{dt} = \frac{k}{\eta^L} \text{div}(\text{grad} p^L) = \frac{k}{\eta^L} \frac{1}{r^2} \frac{d}{dr} \left( r^2 \frac{d}{dr} p^L \right), \quad (4.17)$$

Equation (4.17) should be solved for  $p^L$  for both the aggregate and matrix. In order to solve for pore liquid pressure in the aggregate and matrix,  $p^{a-L}$  and  $p^{p-L}$ , the following initial and boundary conditions are applied:

- Initially, the total mass,  $m_w$ , is equal to  $\rho^L \phi_0$ , where,  $\phi_0$  is the initial porosity of the porous material. (4.18)

- Furthermore, the initial pore pressure is uniform and equal to the atmospheric pressure ( $p_{am}$ ), so  $(p^{p-L})_{t=0} = p_{am}$ . (4.19)

- Thereafter, the surface can be subjected to arbitrary applied pressure,  $p_{app}$  such that

$$\left(p^{p-L}\right)_{r=R_o} = p_{app}. \quad (4.20)$$

- At the aggregate-matrix interface, continuity of the pressure requires the liquid pressure in the aggregate,  $p_l^a$ , and that in the matrix,  $p^{p-L}$ , to be the same, i.e.

$$\left(p^{a-L}\right)_{r=R_i} = \left(p^{p-L}\right)_{r=R_i}. \quad (4.21)$$

- Based on the mass conservation, the liquid flow into the matrix must equal the liquid flow out of the aggregate (and vice versa). Therefore,

$$k^a \left(\frac{dp^{a-L}}{dr}\right)_{r=R_i} = k^p \left(\frac{dp^{p-L}}{dr}\right)_{r=R_i}. \quad (4.22)$$

- Due to the radial symmetry, no flow condition occurs in the center, which yields

$$\left(\frac{dp^{a-L}}{dr}\right)_{r=0} = 0. \quad (4.23)$$

#### 4.1.3 Air entrained versus non-air-entrained concrete

Previous studies show that an air-entrained void can act as an expansion reservoir and cryo-pump and prevent frost damage [3, 42]. This section describes how the proposed model can be used to predict the effect of air entrainment on the cryo-deformation of the model concrete sphere. This is done according to the guidelines proposed by Coussy and Monteiro [41, 42]. Entrained air voids, when properly distributed in a saturated freezing porous solid, can accommodate the expelled liquid water from the freezing sites, and the liquid water freezes instantly upon entering the air

void. Thus, the crystal pressure in the air void is roughly in equilibrium with the atmospheric pressure, and the liquid depressurizes to a value of  $-\frac{\rho^L}{\rho^C} \Sigma_m \Delta\theta + p_{atm}$  (using equation (3.36)), owing to the solid-liquid thermodynamic equilibrium condition. If air voids are assumed to be uniformly distributed in the matrix shell with a spacing distance of  $L$  as shown in Figure 2, the maximum distance that water in the matrix has to travel to reach the equilibrium is  $L$  (instead of  $R_o - R_i$  in case of non-air-entrained matrix). On the other hand, since there is no entrained air void in the aggregate, the maximum distance that water in the aggregate needs to flow is  $R_i + L < R_o$  (instead of  $R_o$  in case of non-air-entrained concrete). The volume fraction of entrained air is accounted for through the value assigned to  $L$ ; as the volume fraction of air entrainment increases, the distance  $L$  that water must flow through the matrix to reach the air bubbles decreases.

Accordingly, for air-entrained concrete the boundary conditions, (4.13) and (4.20), will be

$$\left(\sigma_r^p\right)_{r=R_i+L} = \sigma_{app} = 0 \quad (4.24)$$

and

$$\left(p^{p-L}\right)_{r=R_i+L} = p_{app} = -\frac{\rho^L}{\rho^C} \Sigma_m \Delta\theta + p_{atm}. \quad (4.25)$$

For non-air-entrained concrete the boundary conditions, (4.13) and (4.20), become

$$\left(\sigma_r^p\right)_{r=R_o} = \sigma_{app} = 0 \quad (4.26)$$

and

$$\left(p^{p-L}\right)_{r=R_o} = p_{atm}. \quad (4.27)$$

Boundary conditions (4.26) and (4.27) are particularly valid for concrete with poor/no air-void system near pavement joints and corners where water passes down through the joint fracture to increase the moisture content in the base material and the bottom of the pavement slab in the vicinity of the joint. There are a few situations where, at least where the matrix shell intercepts a concrete surface, these boundary conditions are feasible. If, for any reason, either the water has dried from a surface or the surface water is not frozen, then the boundary condition is essentially  $p_{atm}$ . The water on the surface of the concrete might not be frozen for a pavement, for example, because the surface has a substantially higher concentration of salts due to road salting or because of high traffic movement. In many cases, it is true that the boundary for the simple model chosen would more appropriately be a zero flux boundary (if representing a representative volume element (RVE) of concrete away from the concrete surface), or a zero ice pressure boundary if near an ice-coated surface. However, since D-cracking typically appears near pavement corners and joints where concrete is exposed to free surface, it seems relevant to model such a situation if one is interested in probing failure mechanisms. Furthermore, of the three possible boundary conditions (i.e.,  $p_{atm}$ , zero flux, or ice pressure), a boundary condition of  $p_{atm}$  resulting from a boundary of liquid water or vapor yields the greatest aggregate stresses among the possible boundary

choices. As this boundary condition is most appropriate near the corners of slabs, this might explain why D-cracking is most prevalent in such locations.

## 4.2 Damage mechanism

To implement the proposed model and to investigate the damage mechanism responsible for D-cracking, both air-entrained and non-air-entrained concrete are considered. A coarse aggregate core of diameter 0.0254 m (1 inches) ( $R_i = 0.0127$  m) is considered to be embedded in an elastic matrix shell. According to the ACI 211.1 mixture design procedure, for this maximum coarse aggregate size, if a fineness modulus of 2.7 is assumed for the fine aggregate, the volume fraction of the dry-rodded coarse aggregate is found to be 68%. For this volume fraction, the outer diameter of the model concrete sphere can be calculated as 0.0288 m (1.13 inches) (outer radius,  $R_o$ , of the concrete model sphere is 0.0144 m). The model body is assumed to be initially completely water saturated, and surrounded by free water such that boundary conditions (4.26) and (4.27) prevail for non-air-entrained concrete. Whereas, for the air-entrained concrete, uniformly distributed air bubbles with a spacing of  $L = 250 \mu\text{m}$  [41, 42] are considered along with the boundary conditions given by (4.24) and (4.25). Furthermore, we let  $\eta^L = 1.79 \times 10^{-3}$  Pa s at  $0^\circ\text{C}$ ,  $K^L = 1.79 \times 10^3$  MPa and  $\alpha^L = -98.77 \times 10^{-6} \text{ }^\circ\text{C}^{-1}$  at  $-10^\circ\text{C}$  for supercooled water, and  $K^C = 7.81 \times 10^3$  MPa and  $\alpha^C = 51.67 \times 10^{-6} \text{ }^\circ\text{C}^{-1}$  at  $-10^\circ\text{C}$  for ice crystals[1]. Liquid density,  $\rho^L$ , and crystal density,  $\rho^C$ , are assumed to be  $999.8 \text{ kg/m}^3$  and  $916.7 \text{ kg/m}^3$  at  $0^\circ\text{C}$ , respectively [1]. Additionally,  $\Sigma_m$  is

considered to be 1.2 MPa/°C [1, 24] and liquid degree of saturation,  $S^L$ , is determined using the van Genuchten model [83] according to

$$S^L = \left[ 1 + \left( \frac{1}{\mathfrak{S}} \left( \Delta\theta - \frac{1}{\Sigma_m} \left( 1 - \frac{\rho^C}{\rho^L} \right) (p^L - p_{atm}) \right) \right)^{\frac{1}{1-m}} \right]^{-m}, \quad (4.28)$$

where,  $m$  is the shape factor relating the pore size distribution, and  $0 < m < 1$ . The closer  $m$  is to 1, the more narrowly banded the pore radius distribution. Also, (3.34) is applied here to obtain the capillary pressure. In other words, pore water freezes over a narrow range of temperature when  $m$  approaches unity.  $\mathfrak{S}$  is related to both the porous material geometry and the interface properties and can be determined according to

$$\mathfrak{S} = \frac{2\gamma_{CL}}{R_* \Sigma_m}, \quad (4.29)$$

where,  $R_*$  is the pore radius related to the characteristic cooling  $\mathfrak{S}$ , and  $\gamma_{CL}$  is the water/ice interfacial energy, and is assumed to be 0.0409 J/m<sup>2</sup> [1, 24]  $S^C$  is then calculated from the constraint

$$S^C = 1 - S^L. \quad (4.30)$$

When low liquid pressure is generated, and the term associated with  $p^L$  in (4.28) is neglected, equation (4.17) can be solved analytically in the Laplace Transformed domain. The pore pressure, stress, and strain results obtained in the Laplace transformed domain can then be inverted numerically into the time domain with the Stehfest Algorithm [84] using the script from [85] in *Mathematica*. However, such assumption also neglects effect of high pore pressure on the suppression of the freezing of pore

water [86], and results thus obtained under predict the crack initiating tensile stress.

Dependence on  $S^L$  on  $p^L$  makes (4.17) non-linear, which can thus be solved numerically (e.g., using the Crank-Nicolson scheme [87]). In this work, since high pore fluid pressures were routinely predicted, the problem was solved numerically via finite difference using the Crank-Nicolson scheme.

Intrinsic permeability of the porous media may be approximated by

$$k = k_0 \Lambda(S^L), \quad (4.31)$$

where,  $k_0$  is the constant intrinsic permeability at full liquid saturation,  $\Lambda(S^L)$  is a reduction factor accounting for the change in effective pore volume due to the change in liquid saturation.  $\Lambda(S^L)$  can be determined using the classical Kozeny-Carman equation pioneered by Kozeny and later refined by Carman [88] for unsaturated and saturated media. The Kozeny-Carman model is developed on the basis of a simple assumption of uniform pore size, whereby the entire pore network is characterized by a single smoothed wall cylindrical tube with a constant cross sectional area [89]. Due to this assumption, there have been serious difficulties in applying the theory to materials with wide ranges of pore size distribution [89-92]. In order to determine unsaturated permeability of a porous medium containing interconnected pores of various radii, Mualem [93] proposed an analytical model using the water retention curve. Later, Luckner et al. [94] coupled the van Genuchten model with the Mualem's work to predict intrinsic permeability of the unsaturated porous media as

$$k = k_0 \Lambda(S^L) = k_0 \sqrt{S^L} \left( 1 - \left( 1 - (S^L)^{1/m} \right)^m \right)^2. \quad (4.32)$$

The above equation relates  $k$  to the same shape factor,  $m$  associated with the pore size distribution in equation (4.28). Despite the popularity and widespread use, this model assumes a randomly connected pore network with a length proportional to the pore radius, and therefore does not represent the real material, which has far more complex microstructure with a wide range of pore sizes [95, 96]. Researchers have also found that the Mualem-van Genuchten model provides reasonable predictions for high-permeability soils with permeability varying from  $10^{-12} \text{ m}^2$  to  $10^{-14} \text{ m}^2$ , but considerably under predicts the measured unsaturated permeability of the low-permeability compacted clay soils [96, 97]. This inadequacy limits applicability of the Mualem-van Genuchten model to concrete, since both the aggregate and matrix permeability are typically reported to be less than the above mentioned value [13, 98]. Thus, equation (4.32) will be utilized to approximate the effect of the reduction in permeability associated with ice blocking the pores, but with the understanding that while predicted trends might be accurate the rates and magnitudes of predicted stresses are likely highly inaccurate when using this model.

Studies have shown that capillary porosity of cement paste may range from 0.22 to 0.33 for a  $w/c$  of 0.47 and can be as high as 0.51 for a  $w/c$  of 0.71, depending on the degree of hydration [99]. The volume of pores in most natural aggregates is usually under 3% and rarely exceeds 10% [13, 18]. For limestone, intrinsic permeability is reported to be  $1.7 \times 10^{-21} \text{ m}^2$  [36], and for sandstone, it can be as high as  $1.28 \times 10^{-15} \text{ m}^2$

value [13, 98]. Permeability of a hardened cement paste is reported to have an average value of about  $6 \times 10^{-20} \text{ m}^2$  value [13, 98]. Microscopic image analysis has shown that most capillary pores in a mortar matrix have an average diameter between 0.02 and 50  $\mu\text{m}$  [100].

Typical values for  $\alpha^a$  for various aggregates are reported to vary from  $4 \times 10^{-6} \text{ }^\circ\text{C}^{-1}$  to  $13 \times 10^{-6} \text{ }^\circ\text{C}^{-1}$  [20], whereas for cement paste,  $\alpha^p$  is reported to be  $10 \times 10^{-6} \text{ }^\circ\text{C}^{-1}$  to  $20 \times 10^{-6} \text{ }^\circ\text{C}^{-1}$  [101], and for concrete, it varies from about 6 to  $14 \times 10^{-6} \text{ }^\circ\text{C}^{-1}$ , with an average value of about  $10 \times 10^{-6} \text{ }^\circ\text{C}^{-1}$  [18].  $\alpha^p$  is reported to be  $7.4 \times 10^{-6} \text{ }^\circ\text{C}^{-1}$  for Elgin sand mortar and  $9.9 \times 10^{-6} \text{ }^\circ\text{C}^{-1}$  for Ottawa sand mortar [102]. Callan reported that limestone-sand mortars have coefficients of  $7.2 \times 10^{-6} \text{ }^\circ\text{C}^{-1}$  to  $9 \times 10^{-6} \text{ }^\circ\text{C}^{-1}$ , while most natural siliceous-sand mortars have  $\alpha^p$  near  $10.8 \times 10^{-6} \text{ }^\circ\text{C}^{-1}$  [19]. Therefore,  $\alpha^a = 8 \times 10^{-6} \text{ }^\circ\text{C}^{-1}$  and  $\alpha^p = 10 \times 10^{-6} \text{ }^\circ\text{C}^{-1}$  are assumed.

For both concrete and cement paste, bulk modulus of the solid paste matrix,  $K_s^p$  may vary from  $37 \times 10^3 \text{ MPa}$  to  $63 \times 10^3 \text{ MPa}$ , depending on the water-to-cement mass ratio ( $w/c$ ) and age [36].  $K_s^a$  is stipulated to be  $25.4 \times 10^3 \text{ MPa}$  for the aggregate and  $13.9 \times 10^3 \text{ MPa}$  for the matrix.  $K$  is then approximated in terms of  $\phi_0$  using  $K = (1 - \phi_0)^2 K_s$  [80, 103]. To reveal the damage mechanism, the limiting case of instantaneous freezing of the completely saturated concrete sphere is considered whereby temperature is dropped to  $-15 \text{ }^\circ\text{C}$  in a single step and kept constant for several hours.

Resulting plots are shown in Figure 3 and Figure 4 for analysis of elastic, non-air-entrained and air-entrained concrete, respectively. A high-porosity ( $\phi_0^a = 0.1$ ), low-permeability ( $k^a = 1.7 \times 10^{-21} \text{ m}^2$ ), aggregate with wide distribution of fine pore structure ( $R_*^a = 0.08 \mu\text{m}$ ,  $m^p = 0.5$ ) is assumed to be covered by a moderate-porosity ( $\phi_0^p = 0.2$ ), low-permeability ( $k^p = 1 \times 10^{-21} \text{ m}^2$ ) mortar matrix with fine pore structure ( $R_*^p = 0.08 \mu\text{m}$ ,  $m^p = 0.5$ ). When temperature is dropped below the melting point, pore water freezes in the bigger pores, and positive pressure builds up due to the volume increase associated with the ice formation and the resulting pore volume change. Immediately after the temperature drop, pore liquid pressure at the aggregate-matrix interface differs from that in the core of the aggregate owing to the continuity requirement as provided by (4.21). Furthermore, pressure at the boundary relaxes immediately to atmospheric pressure as the excess water is expelled instantly to the surrounding free water body (non-air-entrained) or to the air-void system (air-entrained concrete) resulting in an immediate pore pressure gradient across the radius. This gradient further increases over time since high positive pressure at the center cannot dissipate at once because of the distance that the excess water must travel to the boundary to relax it. Moreover, the poroelastic relaxation time can be on the order of hours for a material with a very low permeability. This is shown in Figure 3 (a) and Figure 4 (a) for non-air-entrained and air-entrained concrete, respectively. As temperature is held constant, pore pressure dissipates from the outer part of the body, and the boundary contracts. Consequently, the entire body contracts owing to the strain

compatibility, and pore pressure increases more than the initial value before it starts to decay. This phenomenon by which additional pressure builds up at the center is called the Mandel-Cryer effect [104] and is shown in Figure 3 (b) and Figure 4 (b). With time, the excess water from inside the body is expelled to the outer periphery to relieve the gradient, and the pressure equilibrates everywhere. The over pressurized center takes longer to equilibrate (Figure 3 (c) and Figure 4 (c)) and exerts delayed increased tensile tangential stress (Figure 3 (d) and Figure 4 (d)) at the boundary of the aggregate.

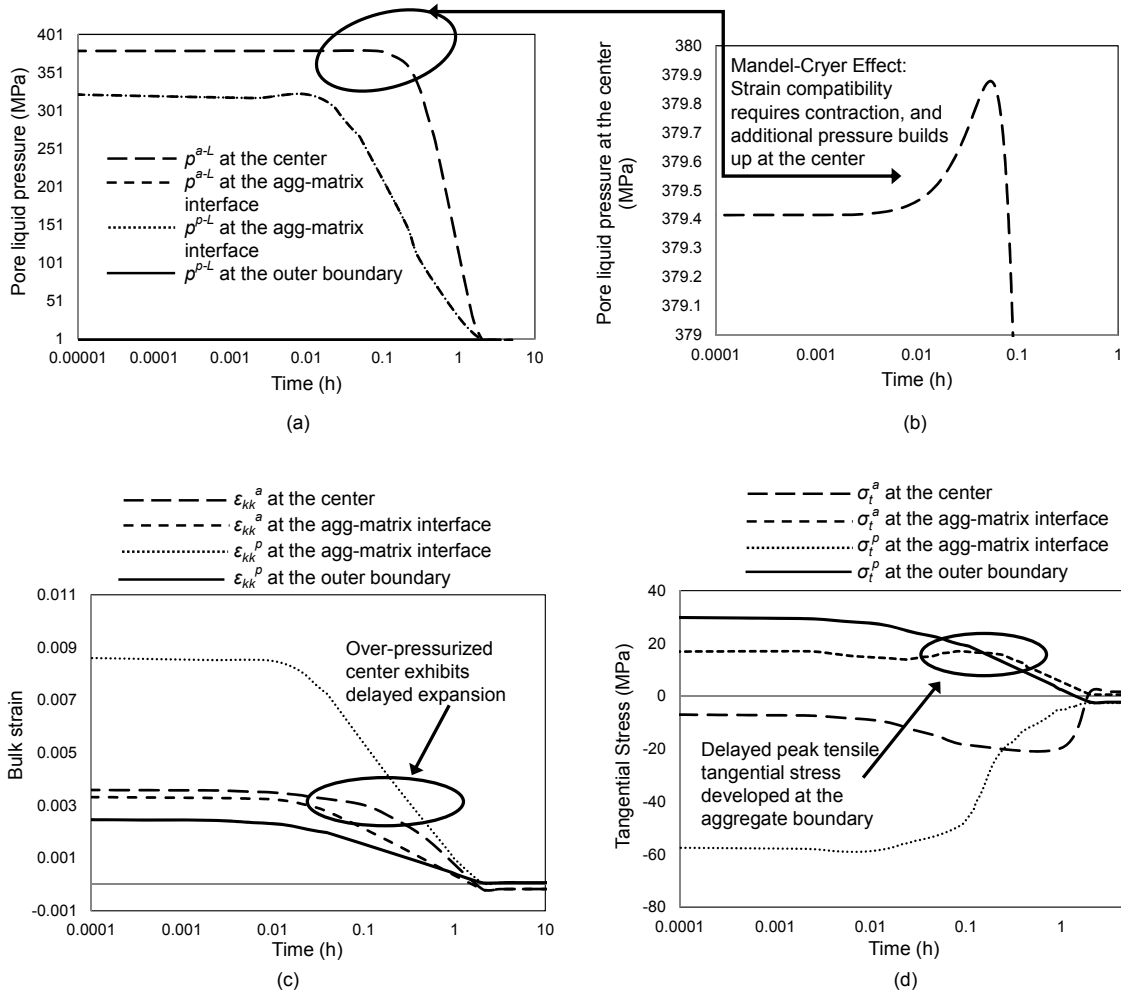


**Figure 3. Pore liquid pressure (a) and (b), bulk strain (c), and tangential stress (d) distribution in non-air-entrained concrete due to a step change of temperature to  $-15^{\circ}\text{C}$ . Center exhibits over pressurization (b) and subsequent expansion (c) due to the Mandel-Cryer effect. As a result, delayed tensile tangential stress (d) is developed at the contracting aggregate boundary.**

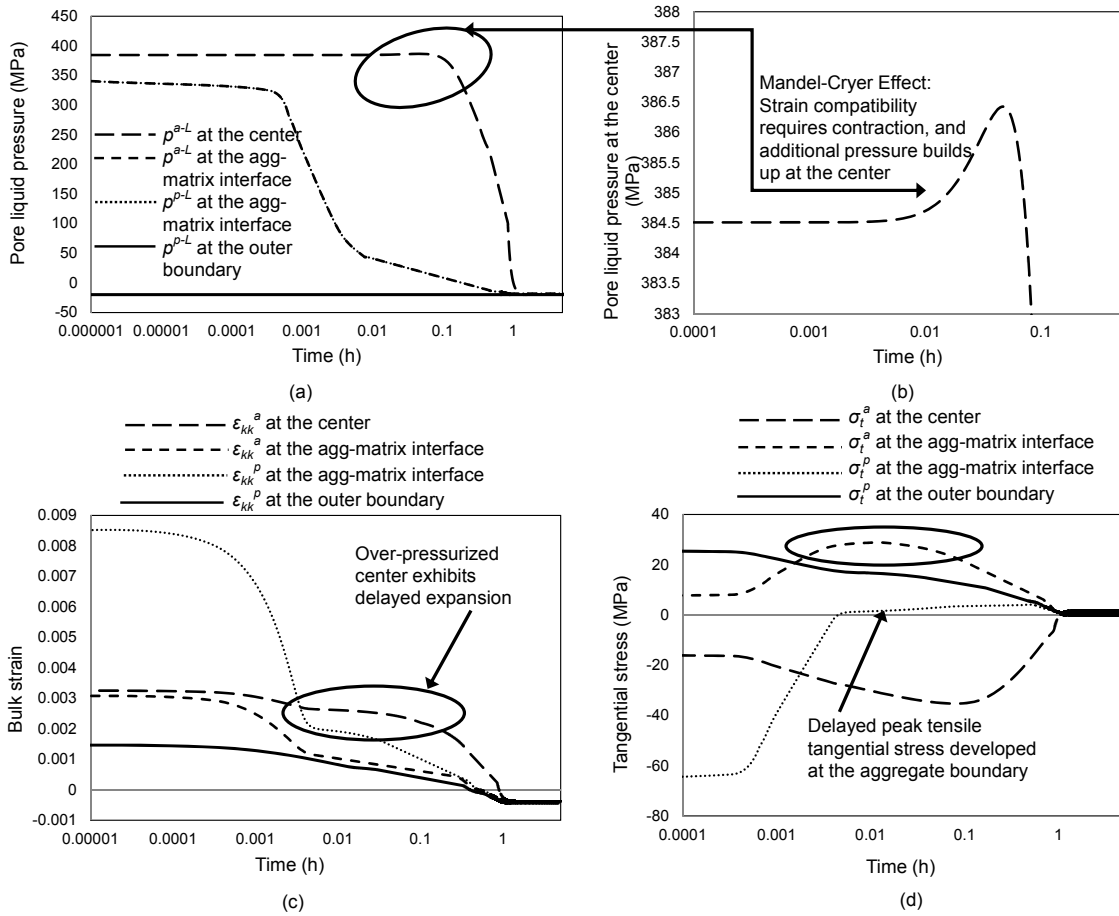


**Figure 4. Pore liquid pressure (a) and (b), bulk strain (c), and tangential stress (d) distribution in air-entrained concrete due to a step change of temperature to  $-15^{\circ}\text{C}$ . As the drained boundary contracts (c), the center over pressurizes itself (b) and exhibits delayed expansion (c) and subsequently exerts peak tensile tangential stress at the boundary (d). However, with time, as the equilibrium is established and the pore water depressurizes, the air-entrained concrete contracts (c) as opposed to the non-air-entrained concrete (Figure 3 (c)).**

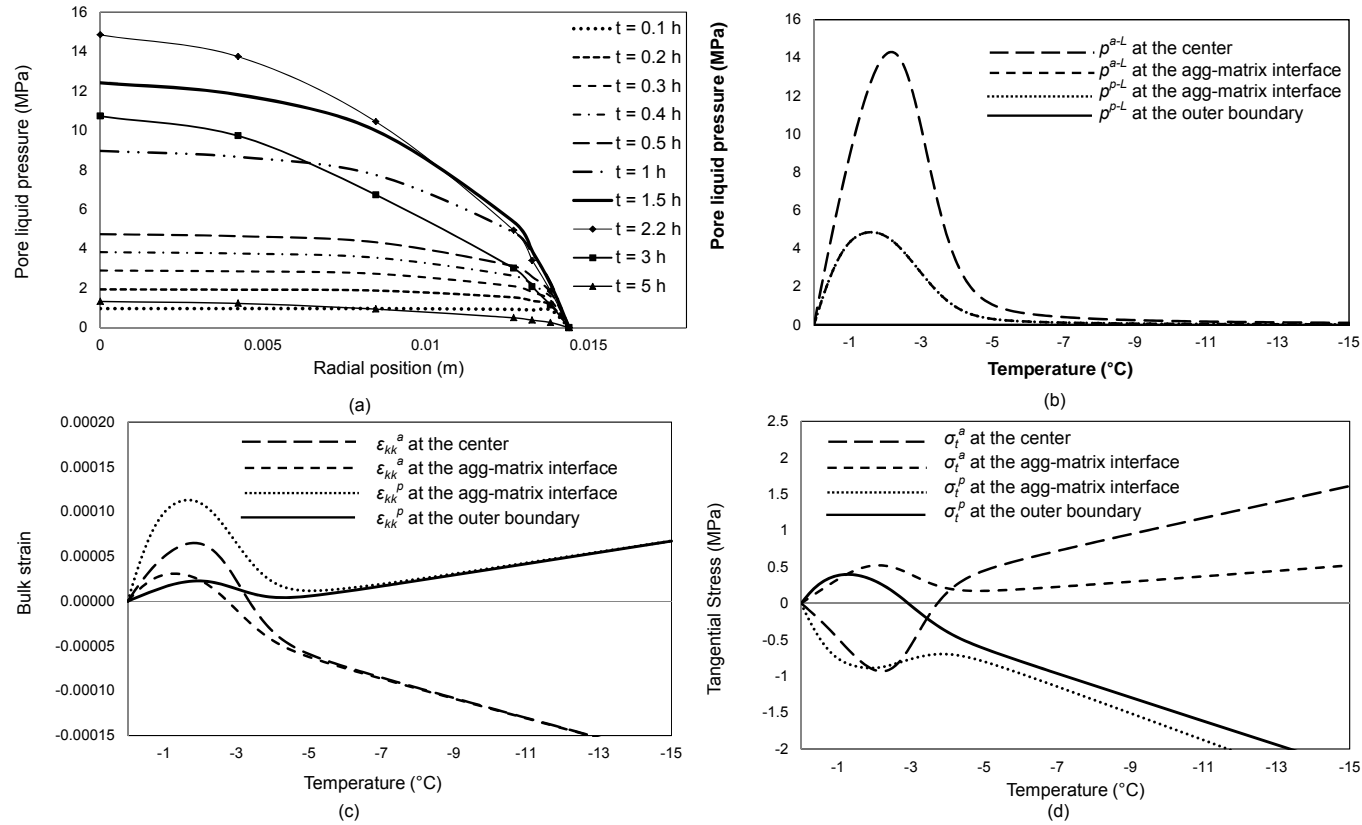
Water in concrete freezes at a temperature below  $0^{\circ}\text{C}$  depending on the radius of curvature of the air-water interface, which is in turn dependent on the pore diameter [105]. This (along with a suppression of the pore water chemical potential associated with dissolved species) is why concrete pore structure can contain both frozen and

unfrozen water under freezing temperatures. When the temperature drops, various deformations occur for different phases (solid skeleton, ice, and unfrozen water) and affect the dimensional change of the body. Water shows highly complex and anomalous behavior due to its intra-molecular hydrogen bonding [106]. Water has a nonlinear CTE, which reduces increasingly at low temperatures and becomes negative below 0 °C [106]. As a result, when water freezes at 0 °C, its volume increases by about 9% under atmospheric pressure. Moreover, while cooling at below 0 °C, unfrozen water expands whereas the frozen ice contracts. Coussy [1] attributed volumetric freezing deformation of a porous material to the following mechanisms: (i) the difference of density between the liquid water and the ice crystal, which results in the initial build-up of an in-pore pressure at the onset of crystallization; (ii) the interfacial effects arising between the different constituents, which eventually govern the crystallization process in connection with the pore access radius distribution; (iii) the drainage of the liquid water expelled from the freezing sites towards the air voids; (iv) the cryo-suction process, which drives liquid water towards the already frozen pores as the temperature further decreases; and (v) the thermomechanical coupling between the solid matrix, the liquid water, and the ice crystal. As a combined action of all these mechanisms, the porous body may exhibit dilation caused by the hydraulic pressure and micro-cryo-suction process, and contraction caused by the thermal deformation [1, 41, 42]. Which deformation mechanism dominates over the others is dictated by the physical and poromechanical properties of the aggregate and matrix, as well as the cooling rate and temperatures. In the model considered in this work, initial contraction caused by the thermal deformation

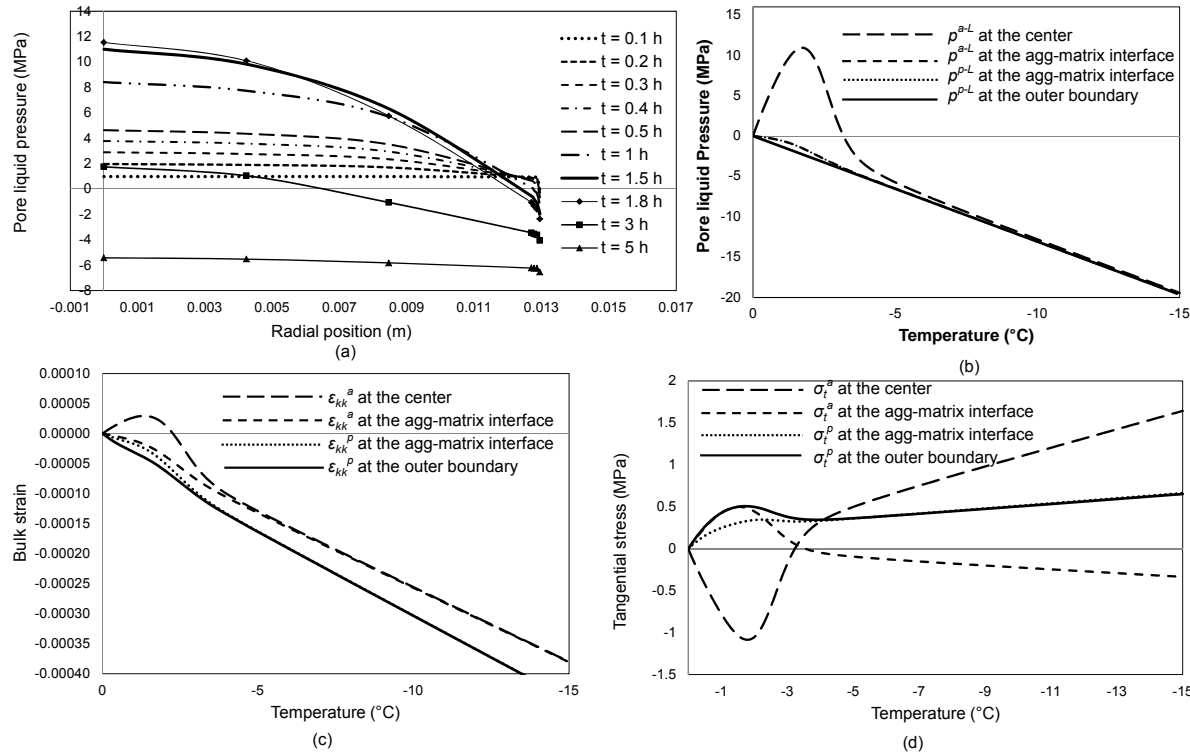
is offset by the dilation resulting from the hydraulic pressure and the micro-cryo-suction process, and hence expansion is observed. The matrix shell expands more than the aggregate due to higher pore volume fraction. However, the outermost fiber of the matrix shell contracts due to the immediate equilibration of the pore pressure. As a result, a strain differential develops throughout the model concrete sphere. With time, dilation disappears as the excess of pore water dissipates and the hydraulic pressure decays to reach equilibrium, resulting in a net contraction/expansion in the non-air-entrained concrete contributed by the competitive action of thermal deformation (contraction) and the micro-cryo-suction process (expansion) (Figure 3 (c)). For air-entrained concrete on the other hand, mortar matrix depressurizes due to the presence of air voids which act as cryo-pumps. Therefore, air-entrained concrete shows a net contraction (Figure 4 (c)).

Figure 3 (d) and Figure 4 (d) provide the tangential stress distribution for the non-air-entrained and air-entrained concrete, respectively. As water solidifies to ice, the crystal sustains a water film between the pore wall and the crystal, allowing it to grow and push the wall away. The pressure that ice generates this way creates tensile hoop stress and is called crystallization stress [16]. Moreover, the pore pressure gradient (Figure 3 (a-b) and Figure 4 (a-b)) created by the various deformations of the constituent materials results in strain differential (Figure 3 (c) and Figure 4 (c)), which in turn generates a tangential stress gradient in the body. This gradient occurs because the center has the peak positive pressure and dilates more than the boundary. The boundary, which is at equilibrium with the boundary pressure, on the other hand, does not dilate and thus

exerts compression on the center. Similarly, higher dilation at the center than the boundary exerts tensile stress at the surface. With time, as the matrix shell starts to contract more than the aggregate core due to the pore water dissipation, over-pressurization occurs at the center, induced by the Mandel-Cryer effect. This in turn results in high tensile stress at the aggregate-matrix interface and high compressive stress at the center. An initial peak stress of around 20 MPa (Figure 3 (d)) is predicted by the model at the outermost fiber of the matrix by the instantaneous cooling of the material to  $-15^{\circ}\text{C}$ , which is unlikely to occur in reality. In reality, the cooling rate is much slower than the rate assumed here ( $0.8\sim 0.9^{\circ}\text{C/hr}$  [45]) and is incapable of developing this high stress. To better represent realistic cooling conditions, temperature is reduced gradually to  $-15^{\circ}\text{C}$  at a rate of  $1^{\circ}\text{C/hr}$ , and the resulting plots are shown in Figure 5 and Figure 6 for non-air-entrained and air-entrained concrete, respectively. At time  $t \approx 3$  hr (Figure 5 (a) and Figure 6 (a)), at which point a significant amount of pore water pressure is dissipated from the matrix shell, over-pressurization at the center may still sustain delayed tensile tangential stresses (Figure 5 (d) and Figure 6 (d)) in the aggregate-matrix interface, which appears as a hump in the plots before  $-5^{\circ}\text{C}$  is reached. This hump vanishes when high-permeability and/or low-porosity aggregates are used.



**Figure 5. Pore liquid pressure (a) & (b), bulk strain (c), and tangential stress (d) distribution for non-air-entrained concrete for a gradual change of temperature at a rate of  $-1^\circ\text{C}/\text{hr}$ . Peak tensile stress (short dashed line in (d)) is developed at the aggregate boundary due to the Mandel-Cryer effect induced by over pressurization (long dashed line in (b)) and delayed expansion of the center (long dashed line in (a)).**



**Figure 6. Pore liquid pressure (a) & (b), bulk strain (c), and tangential stress (d) distribution for air-entrained concrete for a gradual change of temperature at a rate of  $-1^\circ\text{C/hr}$ . Peak tensile stress (dotted line and solid line in (d)) is developed at the matrix due to the Mandel-Cryer effect induced by over pressurization (long dashed line in (b)) and delayed expansion of the center (long dashed line in (c)) which is analogous to the behavior of non-air-entrained concrete. For air-entrained concrete, water can reach the escape boundary faster than the non-air-entrained concrete because of the air-void system. Consequently, air-entrained matrix shrinks more than the non-air-entrained matrix, and causes tensile stress in the mortar that may initiate cracks in the interfacial transition zone (ITZ) over successive freeze-thaw cycles.**

### 4.3 Effect of crystal saturation on permeability

In order to approximate the effect of crystal saturation (i.e., ice blocking pores) on intrinsic permeability using (4.32), and the resulting tangential stress, the following material properties are assumed:  $m^a = 0.5$ ,  $m^p = 0.5$ ,  $\phi_0^a = 0.1$ ,  $\phi_0^p = 0.2$ ,  $k_0^a = 1.7 \times 10^{-19} \text{ m}^2$ ,  $k_0^p = 1 \times 10^{-19} \text{ m}^2$ ,  $\nu^a = \nu^p = 0.2$ ,  $K_s^a = 25.4 \times 10^3 \text{ MPa}$ ,  $K_s^p = 13.9 \times 10^3 \text{ MPa}$ ,  $\alpha^a = 8 \times 10^{-6} \text{ }^\circ\text{C}^{-1}$ ,  $\alpha^p = 10 \times 10^{-6} \text{ }^\circ\text{C}^{-1}$ . Two different pore radii are considered to assess the effect of pore size on the unsaturated intrinsic permeability, and the corresponding effect on the tangential stress at the aggregate boundary of the non-air-entrained concrete. Resulting plots are provided in Figure 7. As shown in the figure, it is seen that ice blocking in larger pores has greater influence on the unsaturated intrinsic permeability than ice blocking in the smaller pores. Furthermore, the result of ice blocking pores is greater peak stresses and greater rate of stress increase (than predicted when assuming a constant permeability). However, previous researchers claimed that large pores significantly affect the permeability function near saturation ( $S_l = 1$  at  $0 \text{ }^\circ\text{C}$ ) [96] and lead to under prediction of the measured values especially for the low-permeability materials [97]. Moreover, in reality unsaturated permeability can be even more complex due to the presence of new macropores caused by freeze-thaw damage, and cannot be accurately determined using simple models like (4.32). Hence, as lower permeability increases the intensity of the tangential stress magnitude, but does not change the overall predicted trends in the following sensitivity analysis, constant intrinsic permeability will be used in this work for the rest of the simulations.

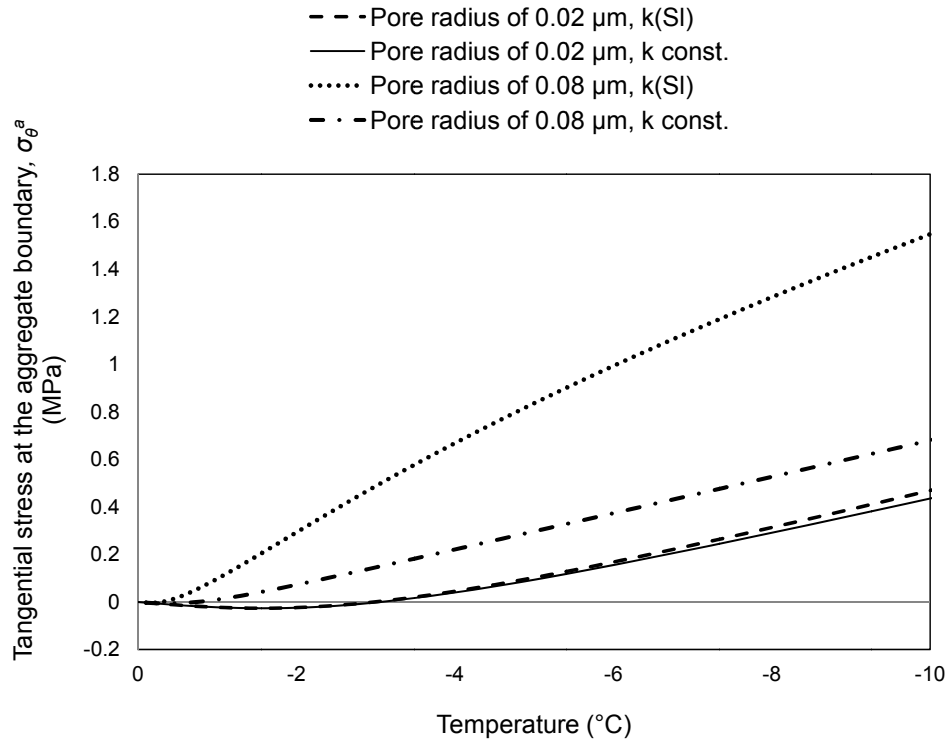


**Figure 7. Effect of unsaturated intrinsic permeability on the tangential stress at the aggregate boundary.**

#### 4.4 Results and discussions

The extent of the expansion and resulting damage under freezing temperatures depends on many factors including aggregate size, pore size distribution, aggregate and matrix permeability, porosity, and thermal properties (e.g., CTE of ice, water, aggregates, and matrix), and aggregate and matrix bulk modulus [11, 14, 17, 45, 46, 107]. In addition, cooling rate and air entrainment play key roles in determining concrete durability. Sensitivity of the damage propensity of non-air-entrained and air-entrained concrete to these various factors is provided in the following subsections. Material properties used to investigate their role in freezing damage are provided in Table 3.

**Table 3. Material properties used for sensitivity analysis where,  $\phi_0$  is the porosity,  $m$  is the shape factor in the van Genuchten model [27] relating to the pore size distribution,  $k$  is the permeability,  $\alpha$  is the coefficient of thermal expansion, and  $R_*$  is the pore radius related to the characteristic cooling. Superscripts,  $a$  and  $p$  denote aggregate and matrix, respectively.**

Effect of:	Aggregate					Matrix					
	Max. agg. size	$\phi_0^a$	$m^a$	$k^a$	$\alpha^a$	$R_*^a$	$\phi_0^p$	$m^p$	$k^p$	$\alpha^p$	$R_*^p$
	m (in)			m <sup>2</sup>	°C <sup>-1</sup>	μm			m <sup>2</sup>	°C <sup>-1</sup>	μm
Agg. pore proper-ties	0.025 (1)	0.1	0.5	$1.7 \times 10^{-21}$		0.08					
		0.1	0.4	$1.7 \times 10^{-21}$		0.08					
		0.1	0.5	$1.7 \times 10^{-21}$		0.1					
		0.003	0.5	$1.7 \times 10^{-21}$		0.1					
		0.003	0.5	$1.7 \times 10^{-18}$		0.1					
		0.1	0.5	$1.7 \times 10^{-18}$		0.1	0.2	0.5	$1 \times 10^{-21}$		
Agg. size	0.025 (1)										
	0.019 (0.75)	0.1	0.5	$1.7 \times 10^{-21}$	$8 \times 10^{-6}$	0.08					
	0.012 (0.5)									$10 \times 10^{-6}$	
Paste pore proper-ties	0.025 (1)	0.1	0.5	$1.7 \times 10^{-21}$		0.08	0.2	0.5	$1 \times 10^{-21}$		0.2
							0.3	0.5	$1 \times 10^{-21}$		0.2
							0.3	0.5	$1 \times 10^{-21}$		0.08
							0.3	0.5	$1 \times 10^{-19}$		0.5
CTE	0.012 (0.5)	0.1	0.4	$1.7 \times 10^{-21}$	$\frac{8 \times 10^{-6}}{6 \times 10^{-6}}$	0.08	0.2	0.5	$1 \times 10^{-21}$		0.08
Cooling rate	0.025 (1)	0.1	0.5	$1.7 \times 10^{-21}$	$8 \times 10^{-6}$	0.04	0.2	0.5	$1 \times 10^{-21}$		0.04

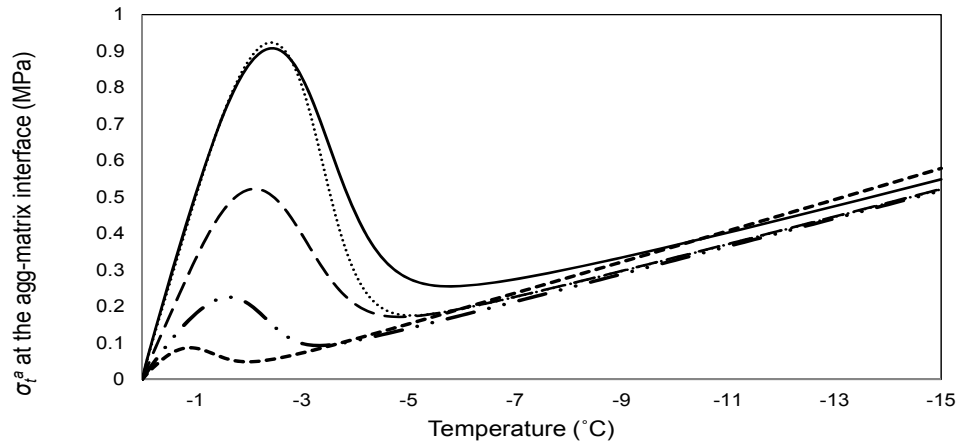
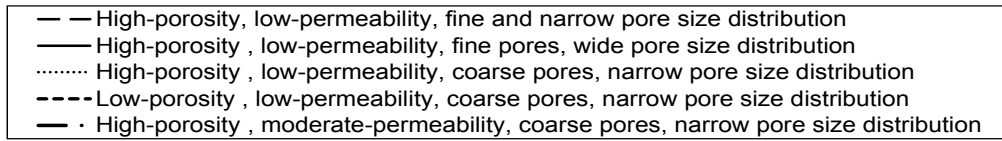
#### 4.4.1 Effect of aggregate pore structure

Based on the previous studies on the aggregate response under freezing conditions, the following classes of aggregates are considered for analyzing the proposed model:

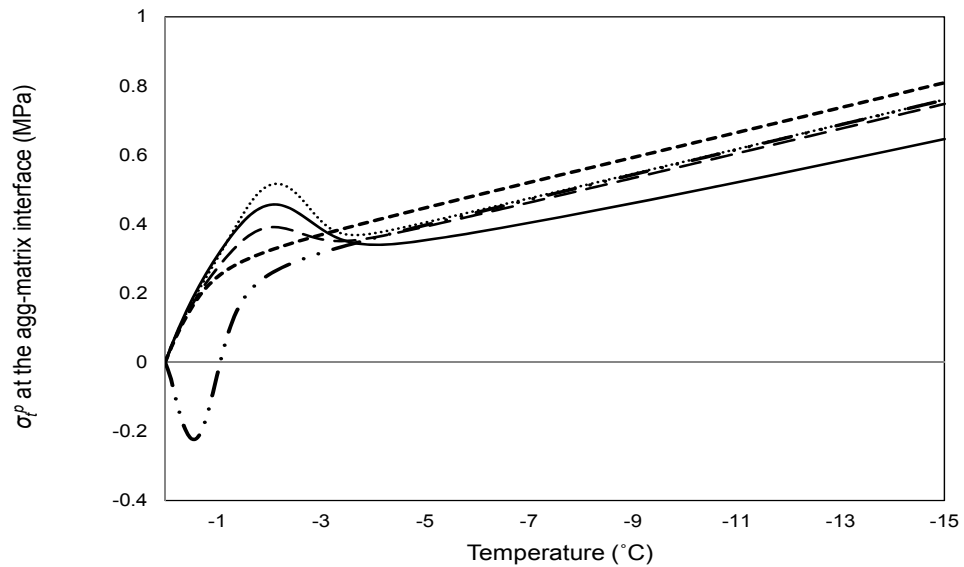
- High-porosity ( $\phi_0^a = 0.1$ ), low-permeability ( $k^a = 1.7 \times 10^{-21} \text{ m}^2$ ) aggregate with fine pores and narrow pore size distribution ( $R_*^a = 0.08 \mu\text{m}$  and  $m^a = 0.5$ ).
- High-porosity ( $\phi_0^a = 0.1$ ), low-permeability ( $k^a = 1.7 \times 10^{-21} \text{ m}^2$ ) aggregate with fine pores and relatively wide pore size distribution ( $R_*^a = 0.08 \mu\text{m}$  and  $m^a = 0.4$ ).
- High-porosity ( $\phi_0^a = 0.1$ ), low-permeability ( $k^a = 1.7 \times 10^{-21} \text{ m}^2$ ) aggregate with coarse pores and narrow pore size distribution ( $R_*^a = 0.1 \mu\text{m}$  and  $m^a = 0.5$ ).
- Low-porosity ( $\phi_0^a = 0.003$ ), low-permeability ( $k^a = 1.7 \times 10^{-21} \text{ m}^2$ ) aggregate with coarse pores and narrow pore size distribution ( $R_*^a = 0.1 \mu\text{m}$  and  $m^a = 0.5$ ).
- Low-porosity ( $\phi_0^a = 0.003$ ), moderate-permeability ( $k^a = 1.23 \times 10^{-18} \text{ m}^2$ ) aggregate with coarse pores and narrow pore size distribution ( $R_*^a = 0.1 \mu\text{m}$  and  $m^a = 0.5$ ).
- High-porosity ( $\phi_0^a = 0.1$ ), moderate-permeability ( $k^a = 1.23 \times 10^{-18} \text{ m}^2$ ) aggregate with coarse pores and narrow pore size distribution ( $R_*^a = 0.1 \mu\text{m}$  and  $m^a = 0.5$ ).

For the above six cases, a 0.0254 m (1 inch) diameter aggregate is assumed to be embedded in a cement paste matrix with fine pore structure ( $R_*^p = 0.08 \mu m$  and  $m^p = 0.5$ ), porosity of  $\phi_0^p = 0.2$ , and permeability of  $k^p = 1 \times 10^{-21} m^2$ . Both air and non-air entrained concrete are considered. In addition, the following material properties are assumed:  $K_s^a = 25.4 \times 10^3 MPa$ ,  $K_s^p = 13.9 \times 10^3 MPa$ ,  $\alpha^a = 8 \times 10^{-6} \text{ } ^\circ C^{-1}$ ,  $\alpha^p = 10 \times 10^{-6} \text{ } ^\circ C^{-1}$  and  $\nu^a = \nu^p = 0.2$ . Temperature is decreased to  $-15 \text{ } ^\circ C$  at a cooling rate of  $1 \text{ } ^\circ C/hr$ . The resulting plots are provided in Figure 8.

For the aggregates with high volume of fine pores with low permeability, the tangential stress developed at the outermost fiber of the aggregate adopts a hump shape imposed by the Mandel-Cryer effect, and therefore exhibits a high value before  $-5 \text{ } ^\circ C$  is reached. Therefore, high-porosity, low-permeability aggregate is found to be susceptible to D-cracking for small temperature cycles, which is in accord with previous findings [11, 13]. On the other hand, for the aggregates with low porosity and/or high permeability, peak tensile stress reduces significantly, because low aggregate porosity creates less hydraulic pressure, and high permeability allows quick dissipation of pore pressure. It should be added here that high-porosity, high-permeability aggregates with open pore structure resemble lightweight aggregates, which proved beneficial under freeze-thaw cycles with improved durability [108, 109].



(a) Non-air-entrained concrete

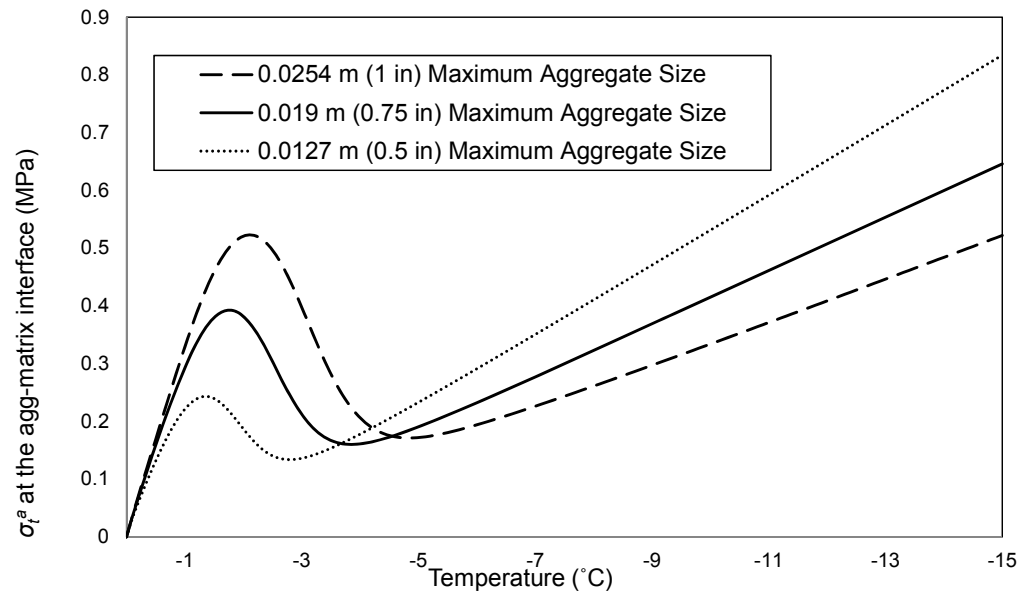


(b) Air-entrained concrete

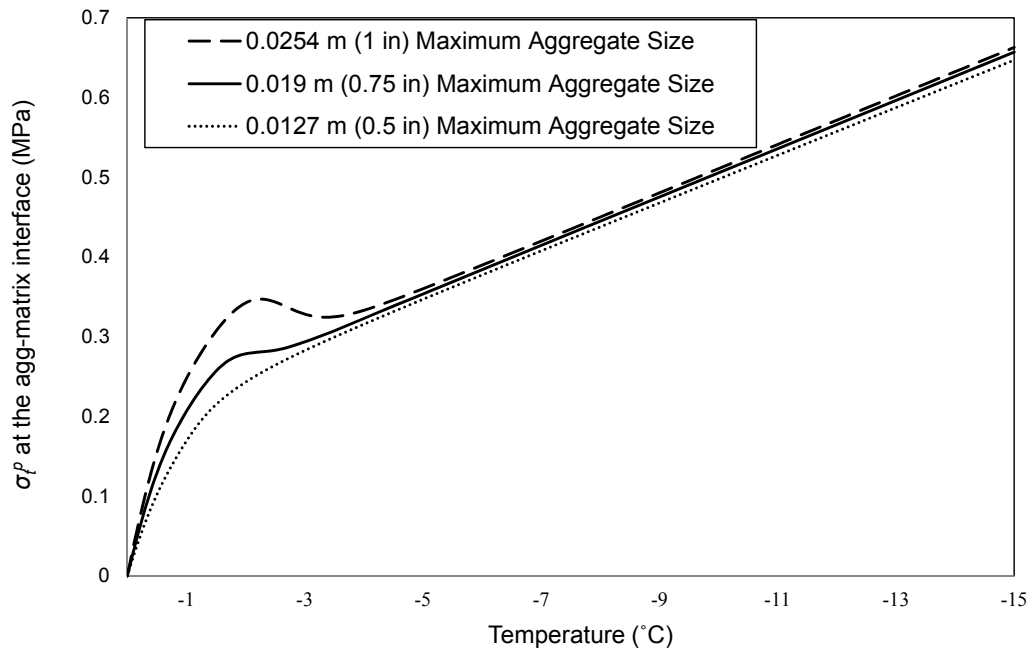
**Figure 8. Effect of aggregate pore properties on the peak tensile stress. At a temperature above  $-5\text{ }^{\circ}\text{C}$ , due to Mandel-Cryer effect, high-porosity, low-permeability aggregates exhibit peak tensile tangential stress at the boundary. Whereas, low-porosity and/or high-permeability aggregates do not show such peak stress because high permeability allows quick pore pressure relaxation to the escape boundary, and low-porosity reduces the impact of the hydraulic pressure.**

#### 4.4.2 Effect of aggregate size

To investigate the role of maximum aggregate size on damage propensity, high-porosity ( $\phi_0^a = 0.1$ ), low-permeability ( $k^a = 1.7 \times 10^{-21} \text{ m}^2$ ) aggregate with fine pores and wide pore size distribution ( $R_*^a = 0.08 \mu\text{m}$  and  $m^a = 0.5$ ), which is expected to be vulnerable to D-cracking is considered. The diameter of the aggregate is changed to 0.013 m (0.5 inch) and 0.019 m (0.75 inches) to examine if it improves or deteriorates the aggregate performance under freezing temperatures. The comparative effect of the aggregate size reduction on the peak stress in the aggregate-matrix interface is shown in Figure 9. It is seen that reducing the aggregate size proves beneficial and reduces damage propensity by dissipating the Mandel-Cryer effect quickly. This result agrees well with the previous empirical model and experimental findings [11, 17]. Larger aggregates with high porosity and high permeability delay the pore pressure relaxation time, and thus exhibit high stress at the aggregate-matrix interface. This may in turn create cracks in the matrix shell, where fatigue tensile stress exceeds the fatigue resistance of the matrix. Although such freeze-thaw damage originating in the cement matrix resembles the cracking caused by nondurable coarse aggregates, it is not considered D-cracking [45]. However, development of cracks in the matrix may alter the stress state and help initiate and accelerate D-cracking during the successive freeze-thaw cycles when unsound aggregates are present in the concrete. In general, it can be concluded that the use of a small aggregate is beneficial because the harmful tensile tangential stresses at the boundary of the aggregate and the matrix are relaxed quickly due to the short travel path to the escape boundary.



(a) Non-air-entrained concrete



(b) Air-entrained concrete

**Figure 9. Effect of aggregate maximum size on the peak tensile stress. Reduction in aggregate size from 0.0254 m (1 inches) to 0.0127 m (0.5 inches) proves beneficial for a high-porosity, low-permeability aggregate and likely reduces damage propensity, which agrees well with the previous empirical findings [11].**

#### 4.4.3 *Effect of paste or mortar pore structure*

Matrix pore properties such as porosity, permeability, and pore size distribution contribute significantly towards the freezing damage of concrete. It is seen from Figure 8 and Figure 9 that at very low temperatures, an air-entrained matrix can undergo tensile stress at the ITZ (interfacial transition zone) owing to thermal contraction, and provoked by the pore liquid depressurization. To investigate the effect of the matrix properties on the tensile stress development, several combinations of matrix pore properties are considered and resulting plots are shown in Figure 10. It is observed that matrix pore properties do not have a substantial influence on the tensile stress at the aggregate boundary. However, tensile stress at the ITZ increases with time as porosity increases and pore size decreases. High porosity of the matrix creates high pore pressure at the beginning. As a result, matrix boundary that contracts due to the presence of the air voids initially exerts compressive stress at the ITZ, which quickly turns into tensile stress triggered by the over pressurization of the aggregate center. Tensile stress is reduced when a majority of the pores have large diameter, and pore water freezes over a narrow range of temperature. Although large pores with uniform pore size distribution expedite pore water freezing and creates high hydraulic pressure at the beginning, such pores also reduce the amount of expelled water (Figure 11), and moderate the damaging tensile tangential stress at the ITZ at a lower temperatures. Analogous results are obtained by Scherer [15] where crystallization stress is reported to be low for large pores. In contrast, as documented by Jackson and Chalmers [110], severity of frost heave increases for fine soils with small pores.

#### 4.4.4 Effect of coefficient of thermal expansion (CTE)

High-porosity ( $\phi_0^a = 0.1$ ), low-permeability ( $k^a = 1.7 \times 10^{-21} \text{ m}^2$ ), fine-pore-structured ( $R_*^a = 0.08 \mu\text{m}$  and  $m^a = 0.4$ ) 0.013 m (0.5 inch) diameter aggregates with two different thermal expansion coefficients  $6 \times 10^{-6} \text{ }^\circ\text{C}^{-1}$  and  $8 \times 10^{-6} \text{ }^\circ\text{C}^{-1}$  are considered for simulations on the effect of CTE on stress development.  $\alpha^p$  of the air-entrained mortar matrix is assumed to be  $10 \times 10^{-6} \text{ }^\circ\text{C}^{-1}$ . Other material properties are prescribed as following:  $R_*^p = 0.08 \mu\text{m}$ ,  $m^p = 0.5$ ,  $\phi_0^p = 0.2$ ,  $k^p = 1 \times 10^{-21} \text{ m}^2$ ,  $K_s^a = 25.4 \times 10^3 \text{ MPa}$ ,  $K_s^p = 13.9 \times 10^3 \text{ MPa}$ , and  $\nu^a = \nu^p = 0.2$ . As shown in Figure 12, due to high CTE difference between aggregate and matrix, the much greater contraction of the matrix versus the aggregate results in high tensile stress at the ITZ<sup>4</sup>. Similarly, peak tensile tangential stress can be found at the aggregate boundary if the aggregate has a greater CTE than the matrix shell. Analogous results were shown by Callan [19] for spherical inclusions with the maximum stress being generated at the aggregate-matrix interface. Therefore, increase in the difference between CTE of the matrix and aggregate (matrix CTE is higher than aggregate) may substantially reduce concrete durability due to increasing tensile tangential stress in the ITZ. In the same way, severe D-cracking is expected if aggregate CTE is significantly higher than the matrix.

---

<sup>4</sup> At lower temperatures, for air-entrained concrete, because the matrix cover is so thin almost uniform stress is developed everywhere.

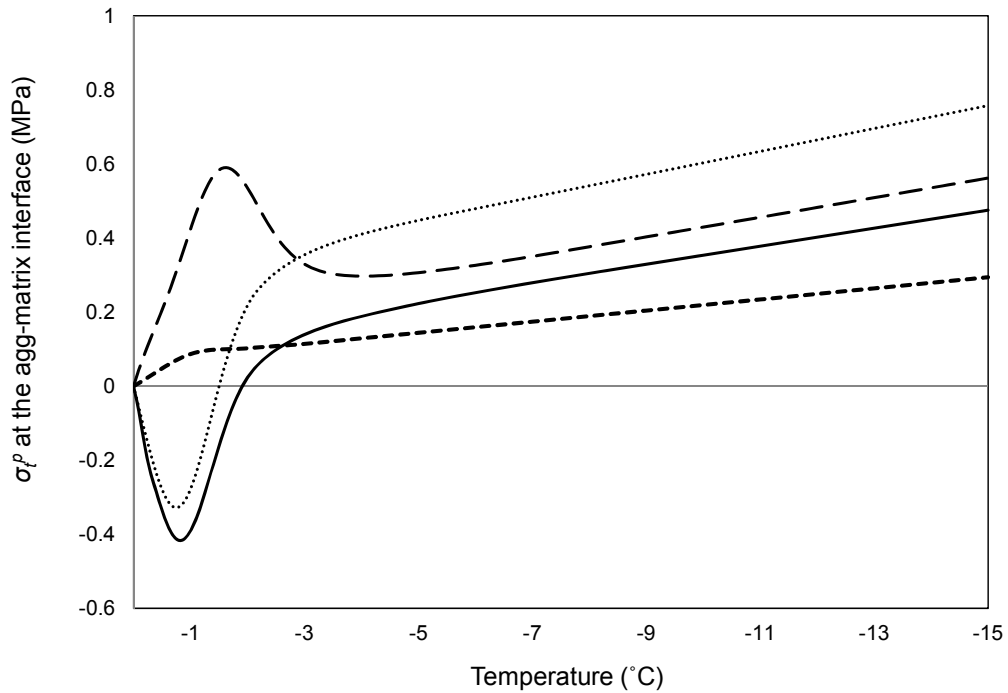
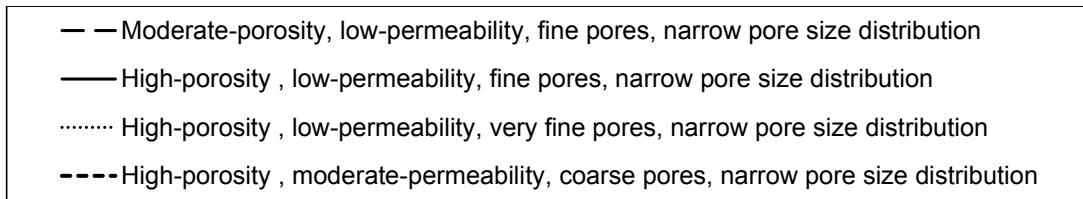


**Figure 10. Effect of matrix pore properties on the maximum tensile stress in the ITZ for air-entrained concrete. Tensile tangential stress decreases if the matrix pore size increases, and porosity decreases.**

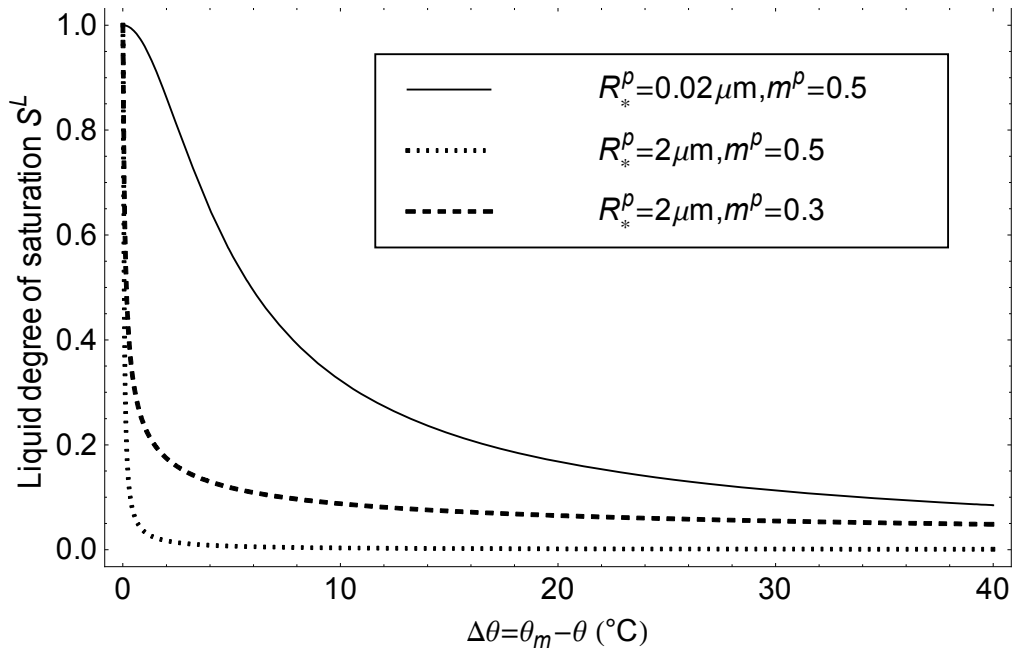


**Figure 11. Effect of pore characteristics on liquid saturation. Large pores with uniform pore size distribution reduce the amount of expelled water. The closer  $m^p$  is to 1, the more narrow-banded the pore radius distribution. In other words, pore water freezes over a narrow range of temperature when  $m^p$  approaches unity.**

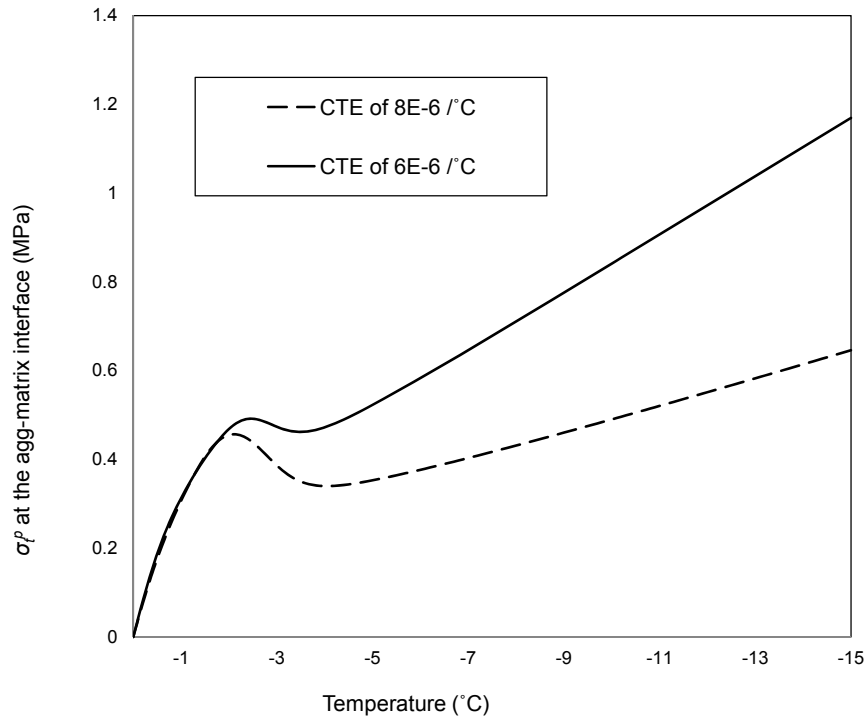


**Figure 12. Effect of different CTE on the peak tensile tangential stress in the ITZ for air-entrained concrete. High difference in the CTE between the aggregate and the matrix may cause high tangential stress in the ITZ, with the stress magnitude progressively increasing as temperature decreases below the melting point.**

#### 4.4.5 Effect of cooling rate

Studies have shown that the freezing rate has a major influence on the severity of concrete freeze-thaw deterioration [45]. In order to simulate the effect of cooling rate on the concrete freeze-thaw durability associated with substandard aggregates, cooling rates of 1 °C/hr, 2.5 °C/hr, and 5 °C/hr are considered. In all cases, the temperature is reduced to -50 °C. The following material properties are prescribed:

$$R_*^a = 0.04 \mu m, R_*^p = 0.04 \mu m, m^a = 0.5, m^p = 0.5, \phi_0^a = 0.1, \phi_0^p = 0.2,$$

$$k^a = 1.7 \times 10^{-21} m^2, k^p = 1 \times 10^{-21} m^2, K_s^a = 25.4 \times 10^3 MPa, K_s^p = 13.9 \times 10^3 MPa,$$

$\alpha^a = 6 \times 10^{-6} \text{ } ^\circ\text{C}^{-1}$ ,  $\alpha^p = 10 \times 10^{-6} \text{ } ^\circ\text{C}^{-1}$ , and  $v^a = v^p = 0.2$ . The resulting plots are shown in Figure 13. It is found that the high cooling rate correlates with high initial dilation. This higher initial dilation occurs because the higher the cooling rate the slower the pore pressure dissipation, and thus the greater the Mandel-Cryer effect. Therefore, rapid cooling is expected to cause more damage than the slow freezing of the material, which is in accord with the findings of [111, 112], where reduced freeze-thaw durability was found for rapid freezing and thawing laboratory tests.

At very low temperatures, the model concrete sphere shows constant contraction regardless of the cooling rate, probably because at such low temperatures, the hydraulic pressure is entirely dissipated, and the resulting contraction is caused by the thermal contraction (non-air-entrained) or cryo-pumps (air-entrained), and depends solely on the material properties. For the air-entrained concrete, a high thermal contraction is seen with time. A recent study by Liu et al. found identical results for a concrete specimen containing 3% entrained air voids exposed to surface water without any salt. High thermal contraction in the air-entrained concrete can be attributed to the liquid depressurization induced by the air voids, which act as expansion reservoirs and cryo-pumps [42]. However, as aggregates do not have entrained air voids, high contraction in the matrix may cause a high differential strain gradient in the concrete composite resulting in high tensile tangential stress in the matrix. This high stress in the matrix may in turn initiate cracks in the ITZ making air-entrained concrete susceptible to thermal cracking, at least when cooled to very low temperatures. Although numerous researchers have proved that air-entrained voids are beneficial against freezing damage, this result is

consistent with [11] (according to which the greatest hydraulic pressure developing the most severe freezing damage occurs in the ITZ with air voids in it), and supports [113] (which states that fully saturated concrete – whether it is air-entrained or not – always shows damage).

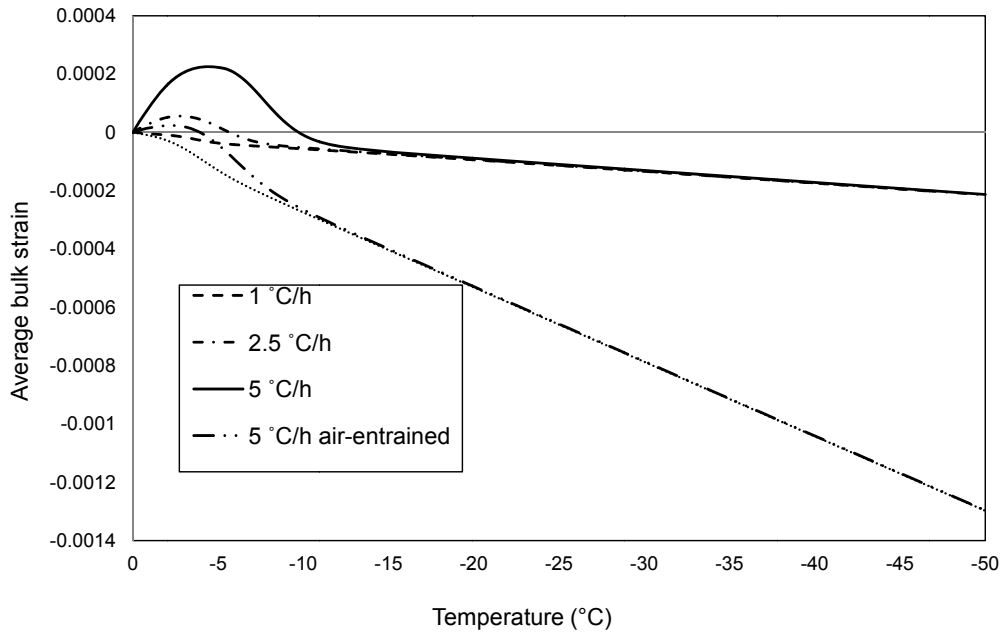


**Figure 13. Effect of cooling rate on the bulk strain of concrete cooled to -50 °C. The higher the cooling rate, the higher the initial swelling. However, at very low temperatures, after which hydraulic pore pressure dissipates completely, constant contraction caused by the thermal contraction (non-air-entrained concrete) is observed that is solely dependent on material properties, and not the cooling rate. In the air-entrained concrete this contraction is more enhanced by the presence of cryo pumps or air voids.**

#### 4.5 Summary

In this section, we have developed a poroelastic composite model that can predict transient stress and strain fields in concrete induced by the freezing of substandard aggregates located at the pavement surfaces, where concrete may be exposed to a pool of

unfrozen water. The model trends agree well with experimental findings obtained from literature. The most relevant results found from this study are:

- The model indicates that for both air-entrained and non-air-entrained concrete, destructive tensile stress may be triggered at the aggregate-matrix boundary, and the damaging stresses are enhanced by the Mandel-Cryer effect.
- The high-porosity, low-permeability aggregates are the most susceptible to freezing damage.
- An increase in aggregate size intensifies the damage propensity by increasing the tensile tangential stresses developed in the aggregate boundary.
- Since aggregates do not contain any entrained air bubbles, excessive contraction of the air-entrained mortar matrix compared to the aggregate may cause high tensile stresses in the aggregate matrix boundary.
- The higher the cooling rate, the greater the hydraulic pressure developed in the aggregate core.
- Significant tensile stresses may also be exhibited in the aggregate-matrix interface if the difference between the CTEs of the aggregate and matrix is high.

## 5 DETERMINING OPTIMUM AIR VOID PARAMETER<sup>5</sup>

The frost resistance of concrete is a function of the concrete constituent properties, entrained air void system parameters, and environmental exposure history. However, only a single maximum value for the void spacing factor is specified for all types of concrete by code writing bodies for successful protection against freezing damage. The advent and utilization of new materials over the recent years warrant reevaluation of the validity of this single pass/fail criteria established more than 50 years ago. In this section, the poromechanical model developed in section 4.1, has been used to predict efficiency of the air void system in various concrete mixture designs involving modern materials, such as light weight aggregate (section 5.1.2), low w/c, and supplementary cementitious materials (SCMs) (section 5.1.3). Effect of environmental exposure has also been investigated and presented in section 5.1.4.

For the non-air entrained concrete, the thickness of the mortar cover ( $R_o - R_i$ ) covering the aggregate particle (radius  $R_i$ ) (Figure 2) is determined as described in section 4.2 using the ACI 211.1 mixture design specification of the required dry rodded aggregate volume fraction and the assumption of spherical aggregate geometry. To be more specific, the radius of the aggregate core,  $R_i$  in Figure 2, corresponds to half of the maximum aggregate size used in the concrete mixture. Once the aggregate volume fraction is known, the mortar volume fraction can be determined by subtracting the

---

<sup>5</sup> Reprinted with permission from Rahman, S. and Z. Grasley, *Determining optimum air-void spacing requirement for a given concrete mixture design using poromechanics*. International Journal of Pavement Engineering, 2016: p. 1-10. Copyright 2016 Taylor & Francis.

aggregate volume fraction from the total volume of the concrete composite, which is unity in this case. The thickness of the spherical mortar matrix shell can then be calculated from the volume-radii relationship of a hollow sphere. For simplicity, we assume that the concrete volume remains constant after it hardens, i.e., we do not account for any reduction of volume due to chemical, autogenous, and drying shrinkage.

The pore pressure in this case is dictated by the atmospheric pressure at the mortar surface (see section 4.1.3). This pore pressure is particularly chosen to mimic degradation of the pavement distresses relevant to the freezing damage that are manifested on the pavement surface where surface water is not frozen due to the presence of deicer salts. The unfrozen surface water would be subject to atmospheric pressure – hence the boundary condition for the model. In contrast, for the air entrained concrete, the uniformly distributed air bubbles with a spacing of  $L$  are considered so that the water from the frozen pores can escape and freeze in these air voids to relax the excess pore pressure. The simulated results are provided and discussed in the following section.

## 5.1 Results and discussion

For simulation, we specify the following properties for the supercooled pore water: viscosity of  $1.79 \times 10^{-3}$  Pa s at 0 °C, bulk modulus of  $1.79 \times 10^3$  MPa and CTE of  $-98.77 \times 10^{-6}$  °C<sup>-1</sup> at -10 °C, and for ice crystals: bulk modulus of  $7.81 \times 10^3$  MPa and CTE of  $51.67 \times 10^{-6}$  °C<sup>-1</sup> at -10 °C [1]. Water liquid density and crystal density are assumed to be  $999.8 \text{ kg m}^{-3}$  and  $916.7 \text{ kg m}^{-3}$  at 0 °C, respectively [1]. Additionally, melting entropy is considered to be  $1.2 \text{ MPa C}^{-1}$  [1]. Typical values for the CTE for

various aggregates are reported to vary from  $4 \times 10^{-6} \text{ } ^\circ\text{C}^{-1}$  to  $13 \times 10^{-6} \text{ } ^\circ\text{C}^{-1}$  [20], whereas for cement paste,  $\alpha^p$  is reported to be  $10 \times 10^{-6} \text{ } ^\circ\text{C}^{-1}$  to  $20 \times 10^{-6} \text{ } ^\circ\text{C}^{-1}$  [114] and for concrete, it varies from about 6 to  $14 \times 10^{-6} \text{ } ^\circ\text{C}^{-1}$ , with an average value of about  $10 \times 10^{-6} \text{ } ^\circ\text{C}^{-1}$  [18]. For siliceous sand mortars CTE can vary from 10 to  $12 \times 10^{-6} \text{ } ^\circ\text{C}^{-1}$ , whereas for the limestone sand mortar this value can range from 10 to  $5 \times 10^{-6} \text{ } ^\circ\text{C}^{-1}$  [19, 20]. Since the aim of this study is to evaluate the significance of concrete material properties on the effectiveness of the air void spacing factor a CTE of  $7 \times 10^{-6} \text{ } ^\circ\text{C}^{-1}$  has been stipulated for *both* the aggregate and mortar matrix. If there is a significant difference in the CTEs of the aggregate and that of mortar, high tensile stress is expected to develop in the aggregate boundary or ITZ. A detail discussion is dedicated to this issue in section 4.4.4. In addition, bulk moduli of the solid aggregate and sand mortar matrix are considered to be  $40 \times 10^3 \text{ MPa}$  and  $30 \times 10^3 \text{ MPa}$ , respectively. The mixture designs and other related input parameters studied in this section are listed in Table 4.

**Table 4. Mixture design input parameters and the related material properties.**

Mix Design	Aggregate					Mortar					Air-void system input parameter	Environmental exposure	
	Max. agg. size (in)	$\phi_0^a$	$k^a$	$m^a$	$R_*^a$	Agg. type	$\phi_0^p$	$k^p$	$m^p$	$R_*^p$	Mortar type	Spacing factor	Cooling rate °C/h
	in		m <sup>2</sup>		μm			m <sup>2</sup>		μm		mm	°C/h
MD1												No air	
MD2	0.75	0.1	1E-21	0.51	10	Limestone	0.2	1E-21	0.51	0.1	Moderate w/c	0.8	2
MD3												0.2	
MD4												0.2	
MD5	0.75	0.2	1E-19	0.51	0.1	Light weight agg.	0.35	1E-20	0.51	0.08	High w/c	0.8	
MD6												No air	
MD7	0.75	0.05	1E-20	0.51	0.1							0.2	2, 5, & 10
MD8	0.35	0.05	1E-20	0.51	0.1	Trap rock	0.2	1E-21	0.51	0.05	Moderate w/c	0.2	10
MD9	0.75	0.05	1E-18	0.51	0.1							0.2	10

**Table 4. Continued**

Mix Design	Aggregate					Agg. type	Mortar				Mortar type	Air-void system input parameter	Environmental exposure
	Max. agg. size (in)	$\phi_0^a$	$k^a$	$m^a$	$R_*^a$		$\phi_0^p$	$k^p$	$m^p$	$R_*^p$		Spacing factor	Cooling rate °C/h
	in		m <sup>2</sup>		μm		m <sup>2</sup>		μm		mm	°C/h	
MD10						Lime-stone	0.1	5E-21	0.51	0.05	MN1: MnDot standard, 15% Fly ash, 4% air	0.228	
MD11							0.1	5E-21	0.51	0.05	MN2: Same as MN1, 15% fly ash, 2.7% air	0.306	
MD12							0.1	5E-21	0.51	0.05	MN3: Same as to MN1, 15% fly ash, 2.5% air	0.78	
MD13	1.25	0.01	1E-21	0.51	0.04		0.2	1E-20	0.51	0.1	MN4: Same as MN1, no fly ash, 2.5% air	0.344	2
MD14							0.05	1E-21	0.51	0.03	MN6: Similar to MN1, 30% C fly ash, 2.5% air	0.261	
MD15							0.05	1E-21	0.51	0.01	MN6-finer pores: Same as MN1, 30% C fly ash, 2.5% air	0.261	

### 5.1.1 *Effect of air entrainment*

Figure 14 illustrates the simulated pore liquid pressure (a) – (c), bulk strain (d) – (f), and tangential stresses (g) – (i) for three mixture designs containing variable air contents: 1) 0 % air content, 2) marginal air entrainment system with spacing factor of 0.8 mm and 3) recommended air entrainment system with a spacing factor of 0.2 mm. The concrete sphere is cooled to  $-10\text{ }^{\circ}\text{C}$  at a rate of  $2\text{ }^{\circ}\text{C/h}$ . It is evident that the decrease in bubble spacing decreases damage propensity by quickly relaxing the pore pressure and reducing the magnitude of the peak tensile tangential stresses developed at the matrix outer boundary. In the non-air-entrained concrete, since there are no air voids present in the mortar matrix, high hydraulic pore pressure of around 9 MPa is developed at the aggregate center resulting in dilation of the aggregate, a phenomenon known as Mandel-Cryer effect in oil and gas industries (see section 4.2 for a detailed discussion). The pore pressure in this case is determined by the atmospheric pressure at the concrete boundary. As a result, the mortar squeezes the expansive aggregate particle, and peak tensile tangential stress of about 0.6 MPa is developed at the outer boundary of the mortar matrix. This tangential stress, over successive freeze thaw cycles, can cause damage to the concrete pavement. The hydraulic pore pressure can be reduced if air voids are provided in the mortar matrix where the expelled water from the frozen capillary pores is relieved and freezes instantaneously without inducing crystal growth pressure. The magnitude of the hydraulic pressure can be significantly reduced by lowering the air void spacing and reducing the distance that the water has to travel from the expelled sites. A reduction of around 4 MPa of hydraulic pressure can reduce the

crack initiating tensile stresses from 0.6 MPa (non-air-entrained concrete Figure 14 (g)) to around 0.3 MPa (Figure 14 (i)) if a spacing factor of 0.2 mm can be attained. It is also seen that the reduction in the spacing factor accompanies decreased expansion at the aggregate core and a slight increase in contraction as concrete is cooled to  $-10\text{ }^{\circ}\text{C}$ . Average bulk strain of these three mixture designs are simulated and presented in Figure 14 (j). For the non-air-entrained concrete, initial contraction caused by the thermal deformation of various phases (ice, water, aggregate and mortar matrix) is offset by the dilation resulting from the hydraulic pressure and the micro-cryo-suction process, and hence expansion is observed everywhere in the sphere. However, due to the instantaneous equilibration of the pore pressure at the outermost boundary, the mortar shell starts contracting and a strain gradient develops across the concrete sphere. As the excess of supercooled water dissipates to the surface of the sphere (non-air-entrained concrete) or that of the air void (air-entrained), a net contraction is observed. For air-entrained concrete, due to the presence of uniformly distributed air bubbles, which freeze the expelled water immediately, mortar matrix depressurizes itself and adds to the overall contraction of the constituent phases. Consequently, a decrease in air-void spacing reduces the dilation of the saturated concrete which is consistent with the results published by Kang et al. [27]. A reduction in air void spacing also increases the ultimate contraction of the concrete composite as shown in Figure 14 (j).

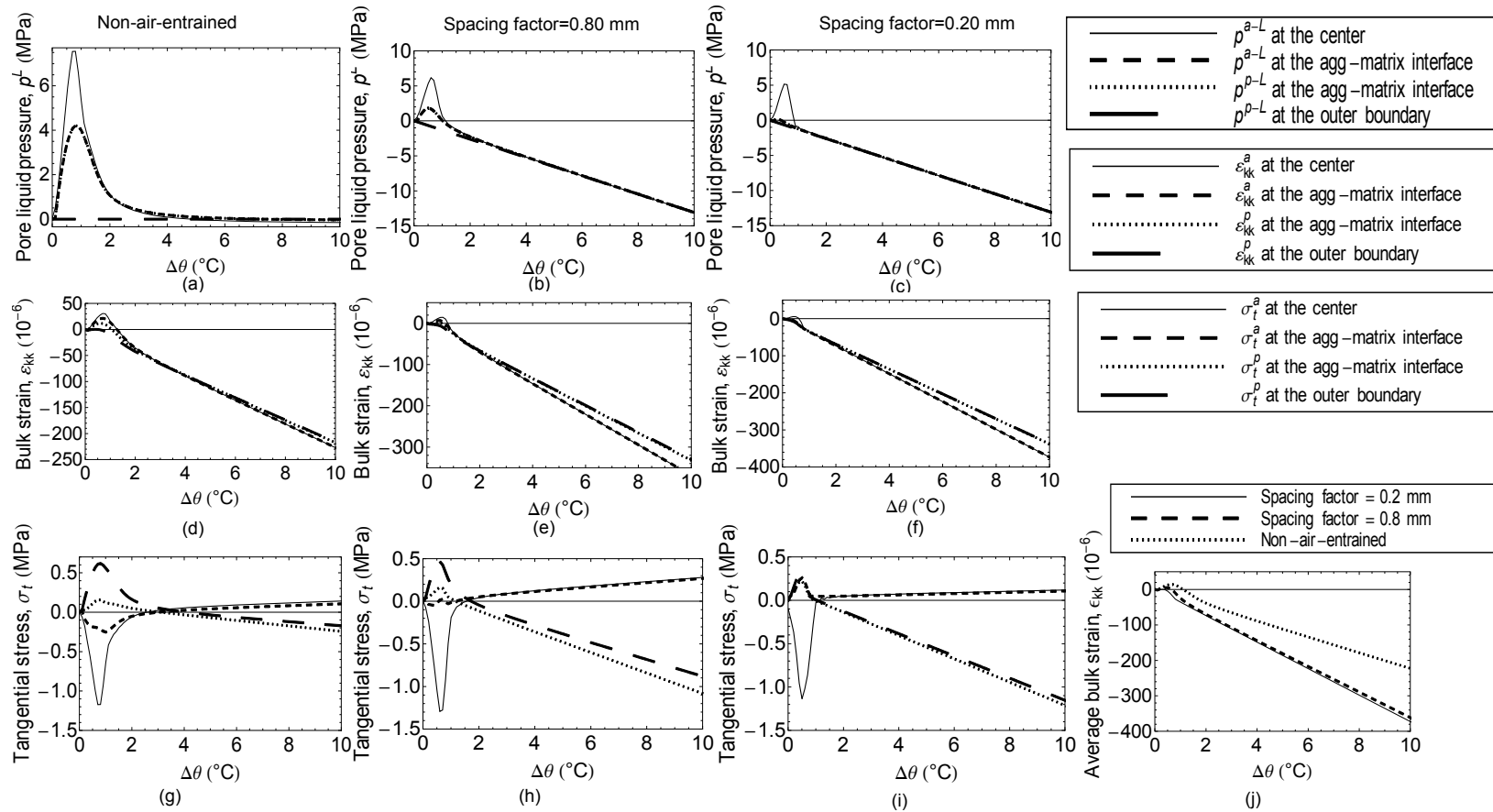


**Figure 14. Modeled pore pressure ( $p^L$ ), bulk strain ( $\epsilon_{kk}$ ), and tangential stresses ( $\sigma_t$ ) for non-air-entrained concrete (mixture design 1 (MD1)), and air-entrained concrete with 0.8 mm (MD2) and 0.2 mm (MD3) spacing factor. Superscripts  $a$  and  $p$  denote aggregate and mortar matrix, respectively.  $\Delta\theta$  is the change in temperature and measured as  $\theta_m - \theta$ . Here,  $\theta_m$  is the melting temperature (i.e.,  $0^\circ\text{C}$ ), and  $\theta$  is the current temperature.**

### *5.1.2 Effect of light weight aggregate on freezing stresses with variable spacing factors*

Tangential stress distributions in concrete containing high-porosity, high-permeability, aggregates (characteristics of light weight aggregates), for three different scenarios (concrete with 0.2 mm spacing factor (MD4), 0.8 mm spacing factor (MD5), and non-air-entrained concrete (MD6)) are presented in Figure 15. It has been observed that, although non-air-entrained light weight aggregate concrete can sustain mild winter where temperature drops to around  $-5\text{ }^{\circ}\text{C}$  Figure 15 (a), it can cause high tensile stresses at the aggregate center if used in very harsh winters where temperature decreases below  $-10\text{ }^{\circ}\text{C}$  Figure 15(b). Similar results are demonstrated by several studies performed on light weight aggregate concrete exposed to severe freezing suggested by the ASTM C666 procedure [115, 116]. The peak tensile stresses expected in harsh winters can be mitigated using air entrainment. However, for small freeze-thaw cycles, with temperature above  $-5\text{ }^{\circ}\text{C}$ , air voids can cause high tensile tangential stress at the matrix outer boundary, and may prove less efficient than the non-air-entrained concrete in mitigating freezing damage. Since the air entrained mortar depressurizes as the air voids act as expansion reservoirs and cryo pumps [42], the mortar shell contracts. Subsequently, the mortar shell experiences tensile tangential stress as it constrains the aggregate that does not contain any air filled pores. The resulting high stress may propagate to the ITZ if the spacing factor is further reduced (Figure 15(a)) and may in turn initiate cracks in the ITZ, making air-entrained concrete susceptible to thermal cracking. A similar conclusion was deduced by Verbeck and Landgren (1960), who hypothesized that high-porosity, high-permeability aggregates with coarse pore structure

can cause failure to the surrounding mortar by building high external pressure [11]. Development of high stress in the aggregate center, as shown in Figure 15 (b), is also in good agreement with the experimental studies performed by Mao et al (2009). Their work on the damage analysis of lightweight aggregate concrete shows that micro-cracks originate in the aggregate particle and spread to the nearby mortar when exposed to harsh freeze-thaw tests [116]. The modeling also suggests that to effectively protect light weight aggregate concrete in harsh winters, it is crucial to achieve the recommended air void spacing factor since high spacing factor will cause high tensile tangential stresses at the aggregate center.

### *5.1.3 Effect of SCM and low w/c on freezing stress with variable bubble spacing factor*

SCMs are widely used in the majority of the concrete mixtures in highway pavements, and there is evidence that SCMs adversely react with some air entraining admixtures, thus affecting the air void system parameters. A high dosage of SCM tends to induce higher spacing factor than the air-entrained concrete without any SCM [117]. The mixture designs selected for this study are adopted from the Strategic Highway Research Program (SHRP) report that highlighted the durability responses of several concrete specimens with varying amount of SCMs (added as a partial replacement of cement by mass) and marginal air content [107]. The corresponding mixture design parameters are listed in Table 4 for MD10-15. All these specimens showed a minimum durability factor of 95 despite of exhibiting spacing factor more than the maximum requirement [107]. The resulting stress analyses for these mixture designs are shown in Figure 16. A cooling rate of  $-2\text{ }^{\circ}\text{C/h}$  is used to reduce the temperature to  $-20\text{ }^{\circ}\text{C}$ . It is

seen that the mixture designs MD10 – MD14 showed similar peak tensile stresses at the paste inner and outer boundaries, which is consistent with the findings of the original report. However, MD15 was predicted to exhibit twice as much stress as the other mixture designs, suggesting that very fine pores (pore radii  $< 0.05 \mu\text{m}$  for both the aggregate and mortar matrix, Table 4, MD15) may adversely affect durability of concrete by inducing high crystallization pressure for prolonged period and causing extended peak tensile stresses. Similar projections of durability are also possible for high contents of SCMs, which implies that there is an optimum amount of SCMs that provides good durability. This optimum SCM content is reported to be 15%, above which further increases in SCMs were claimed to reduce durability unfavorably by adversely affecting the moisture movement within the pore space [107, 117]. Numerous studies [50, 51, 53-55] on high strength concrete with low w/c ratio also confirmed the modeled trends presented herein; i.e. the required spacing factor for low-porosity, low-permeability mortar or cement matrix with fine pores may be higher than the durability requirement of a maximum spacing of 0.2 mm. Thus, the ACI 318 specification of minimum air content may be overly conservative for low w/c, high strength concrete with or without the addition of SCMs.

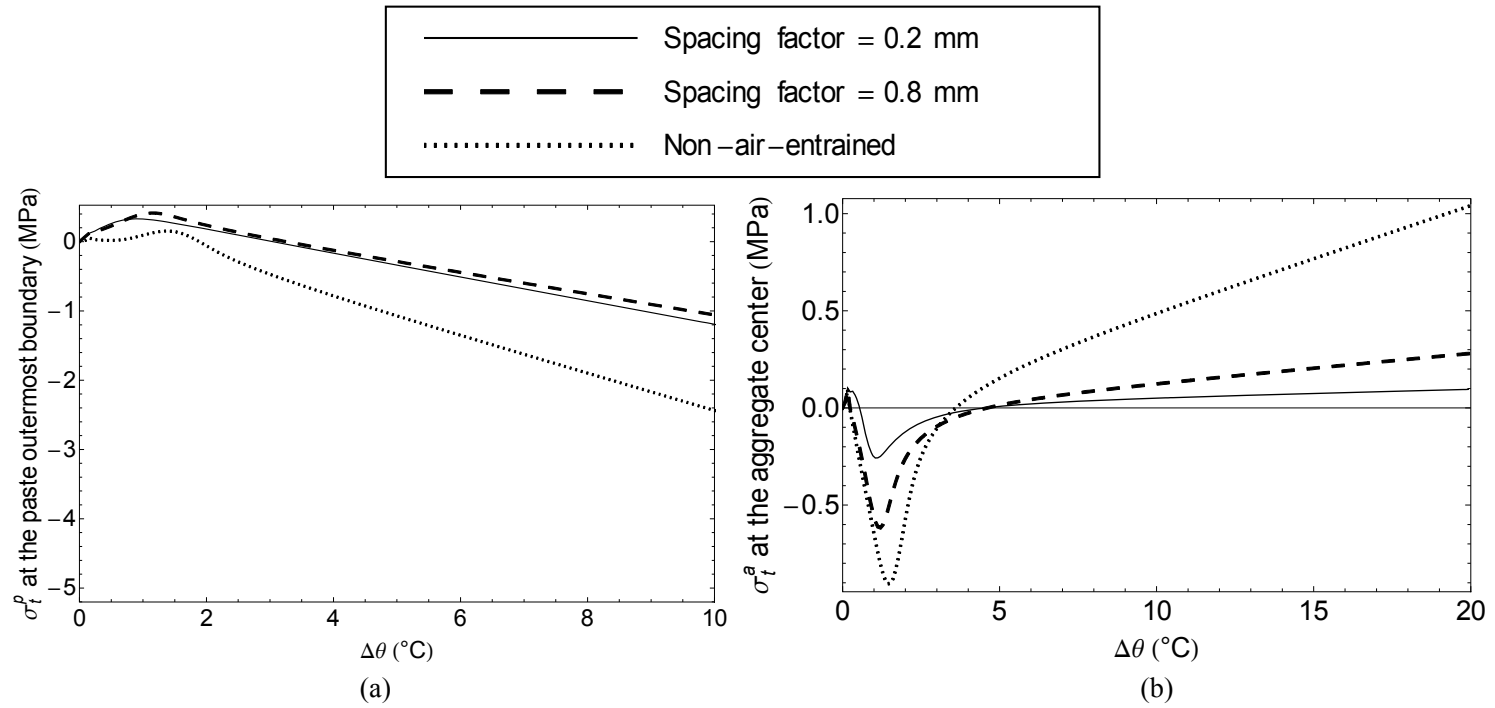


**Figure 15. Effect of light weight aggregate and air entrainment on the tangential stresses ( $\sigma_t$ ) for MD4, MD5, and MD6.**

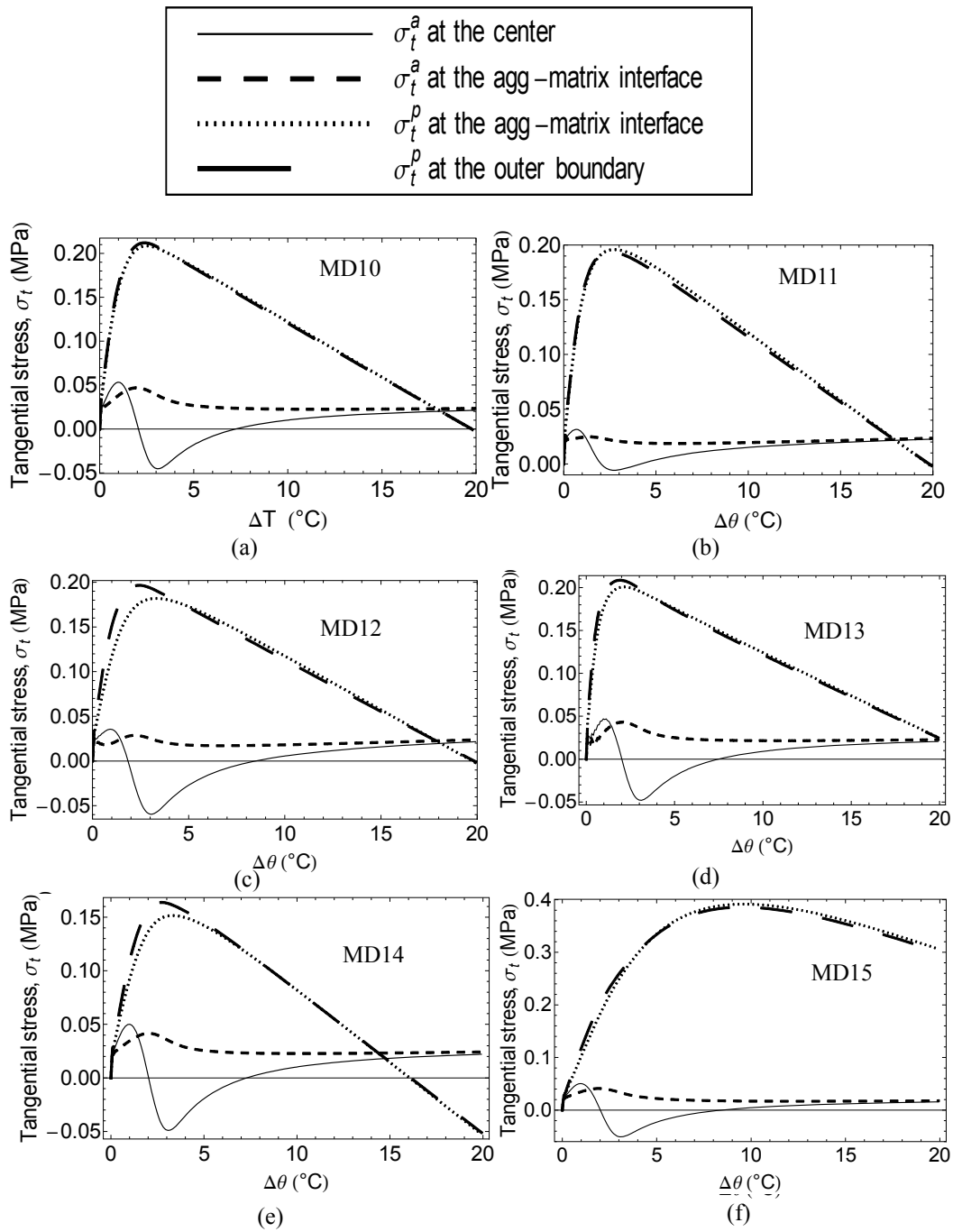


**Figure 16. Effect of SCMs and the air void spacing factor on the tangential stresses ( $\sigma_t$ ) developed in the concrete sphere (MD10 –15). Superscripts  $a$  and  $p$  denote aggregate and mortar matrix, respectively.**

#### 5.1.4 *Effect of environmental exposure*

To study the significance of the magnitude and duration of the minimum temperature to which concrete is exposed, three different cooling rates have been studied: 2 °C/h, 5 °C/h, and 10 °C/h. The resulting average bulk strain, maximum pore liquid pressure generated at the aggregate center, and the peak tensile stress developed at the mortar outermost boundary are reported in Figure 17. The spacing factor of 0.2 mm is maintained for all three mixtures. As seen in the figure, a slight expansion is observed for high cooling rates as the concrete sphere is cooled to  $-5$  °C. This expansion is due to the limited time available for pressurized water to travel to the nearest air void associated with the faster cooling rate. At very low temperatures, a constant contraction is observed that is independent of the cooling rate. The reason behind this uniform contraction is probably that at low temperatures all excess pore pressure is completely dissipated, and the resulting contraction caused by the thermal deformation of various phases and depressurization of the expelled water in the air voids is a function of material constituent properties, and does not depend on the cooling rate. This observation substantiates the claim that existing, standardized laboratory tests that incorporate very high cooling rates in assessing concrete durability are overly severe and thus may under predict durability of certain concrete mixture designs. Furthermore, the results depict that the maximum recommended spacing factor may not be adequate for cold regions where temperature drops at a very high rate. An efficient way to mitigate this problem would be to adopt a concrete mixture design that utilizes high permeability aggregates and/or smaller sized aggregate particles that would quickly dissipate the

hydraulic pore pressure relieving the tensile stresses. Average bulk strain, pore pressure, and the tangential stresses for such concrete mixtures are simulated in Figure 18, supporting this claim.

## **5.2 Summary**

Poroelectricity has been utilized to determine the role of various concrete constituents and air void system on the damage propensity of concrete exposed to freezing temperatures. It is found that a maximum threshold of acceptance, for instance a 0.2 mm spacing factor, may not be adequate for all concrete mixture designs subject to various cooling conditions. The model also suggests that concrete with low-porosity, low-permeability mortar matrix, a characteristic property of mortar containing supplementary cementitious materials and/or low water to cement ratio, can perform satisfactorily under freezing temperatures even with a spacing factor greater than the recommended value. If utilized for design, this model will give more freedom to practitioners in ensuring concrete durability by controlling multiple factors including the concrete mixture components and proportions rather than just satisfying a single pass/fail criterion for void spacing factor for all concrete mixtures.

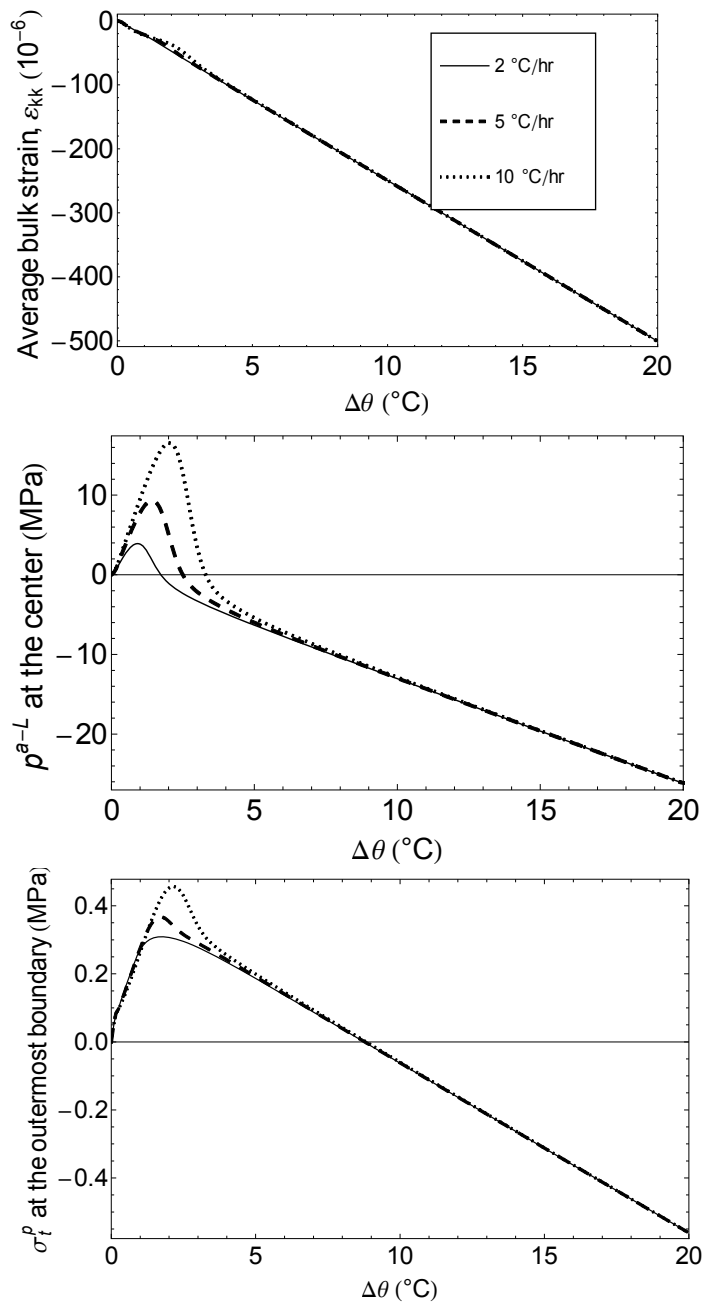


**Figure 17. Effect of cooling rate on the average bulk strain ( $\varepsilon_{kk}$ ), pore pressure at the aggregate center ( $p^{a-L}$ ), and peak tangential stresses ( $\sigma_t^p$ ) developed at the matrix outer boundary for the mixture designs, MD7 with cooling rate of 2 °C/h, 5 °C/h, and 10 °C/h.**

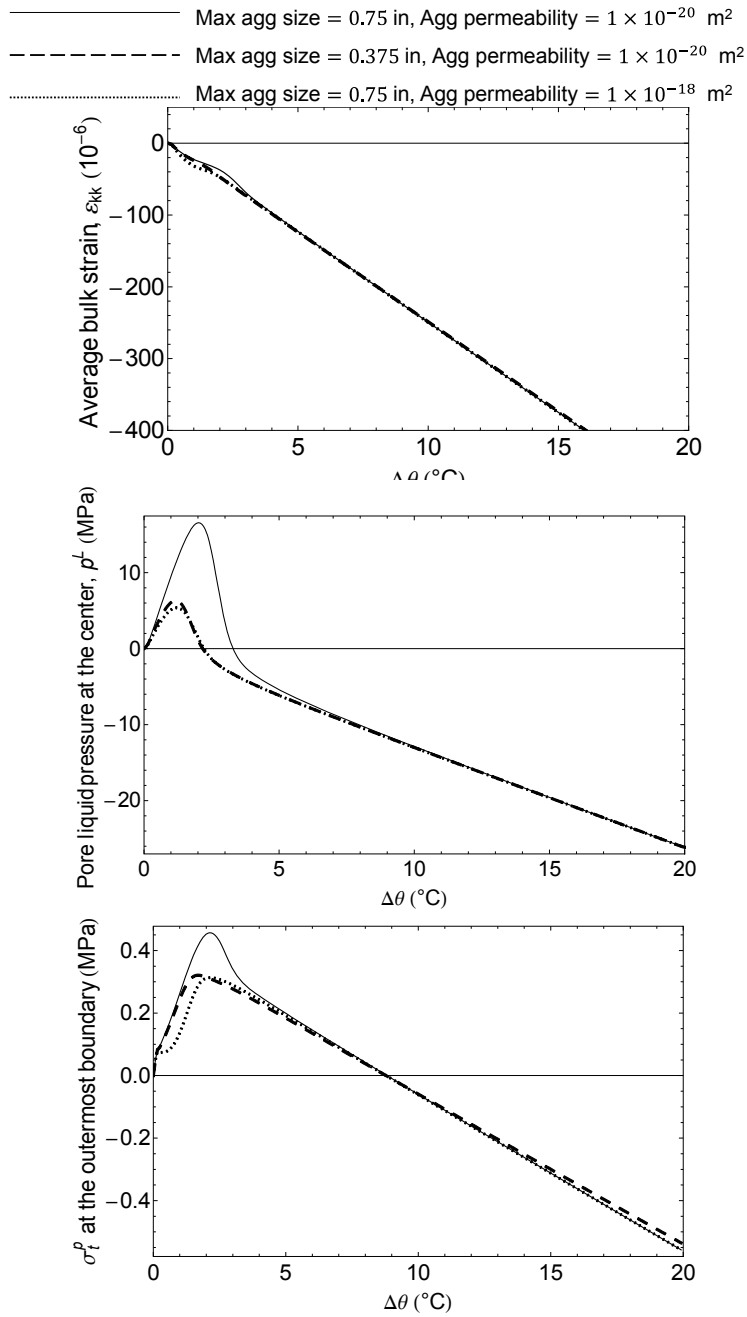


**Figure 18. Effect of aggregate size and permeability on the average bulk strain ( $\varepsilon_{kk}$ ), pore pressure at the aggregate center ( $p^{a-L}$ ), and peak tangential stresses developed at the matrix outer boundary ( $\sigma_t^p$ ) exposed to a cooling rate of  $10 \text{ }^{\circ}\text{C/h}$  (MD7, MD8, MD9, & MD10).**

## 6 EVALUATING CONCRETE COMPATIBILITY FOR THE CONSTRUCTION OF LNG TANKS<sup>6</sup>

In section 6.1, the theory of unsaturated freezing porous media is applied to model deformation of concrete, whose pore network is pressurized by the wet air, frozen ice, and unfrozen water. A general solution scheme is provided for the appropriate boundary conditions pertaining to the primary concrete containment in a liquefied natural gas tank in section 6.2. Effect of cooling rate, moisture content, and cryo-swelling is presented in section 6.3 to inform practitioners about the probable range of thermal deformation exhibited by concrete cooled from room temperate to cryogenic temperatures.

### 6.1 Deformation of fully and partially saturated concrete

Determination of free strain induced in freezing concrete completely saturated with water follows the same procedure described in section 3.3. In case of a partially saturated porous body subjected to freezing, a third phase,  $J=G$  representing the gas phase has to be introduced, and  $\varepsilon_f$  of (3.41) must be modified such that

$$\varepsilon_f = \frac{b^C p^C + b^G p^G + b^L p^L - 3K \alpha \Delta\theta}{3K}, \quad (6.1)$$

---

<sup>6</sup> Reprinted with permission from Rahman, S., et al., *Simulation of Mass, Linear Momentum, and Energy Transport in Concrete with Varying Moisture Content during Cooling to Cryogenic Temperatures*. Transport in Porous Media, 2016. **112**(1): p. 139-166. Copyright 2016 Springer Science+Business Media Dordrecht.

<sup>7</sup> The gas pressure,  $p^G$ , is generally much smaller than the liquid and crystal pressures, but is included for completeness.

along with

$$b = b^C + b^G + b^L = 1 - \frac{K}{K_s}. \quad (6.2)$$

Determination of  $b^C$ ,  $b^G$  and  $b^L$  is provided along with the state equations associated with unsaturated thermo-poro-elastic material in APPENDIX B. For a porous material partially saturated with a gaseous phase and partially saturated with liquid water, the pore liquid pressure provoked by the gas-liquid interface may be expressed by the Laplace equation,

$$p^G - p^L = \frac{2\gamma_{GL}}{r_{GL}}, \quad (6.3)$$

where  $r_{GL}$  denotes the current circumferentially averaged radius of curvature of the gas-liquid interface formed by the evaporation process, and  $\gamma_{GL}$  is the surface energy of the gas-liquid interface. Kelvin's law relates the isothermal pore liquid pressure to the current relative humidity,  $h_r$ , as

$$p^G - p^L = -\frac{R\theta}{\bar{V}^L} \ln(h_r). \quad (6.4)$$

Here,  $R$  represents the ideal gas constant,  $\bar{V}^L$  is the molar volume of the pore liquid.

Equations. (6.3) and (6.4) combine to give

$$\frac{1}{r_{GL}} = -\frac{R\theta}{2\gamma_{GL}\bar{V}^L} \ln(h_r). \quad (6.5)$$

Consequently, the liquid saturation,  $S^L$ , which is the function of the largest pores having the approximate entry radius  $r_{GL}$  can be specified as

$$S^L = S^L(r_{GL}). \quad (6.6)$$

Once the temperature is reduced below the melting point and pore radius is large enough to accommodate crystallization, the capillary pressure on the crystal is dictated by the Laplace equation,

$$p^C - p^L = \frac{2\gamma_{CL}}{r_{CL}}. \quad (6.7)$$

Therefore, along with the thermodynamic equilibrium between the solid and liquid phases governed by (3.36), radius of the crystal-liquid interface,  $r_{CL}$ , can be expressed as

$$\frac{1}{r_{CL}} = -\frac{1}{2\gamma_{CL}} \left\{ \sum_m (\theta - \theta_m) + (1 - \rho^C / \rho^L) (p^L - p_{atm}) \right\}. \quad (6.8)$$

The current liquid saturation can then be determined as the function of the largest pores with the entry radius  $r_{CL}$  that are still filled with liquid water. Thus,

$$S^L = S^L(r_{CL}). \quad (6.9)$$

Crystal saturation can be calculated from the conservation of the overall mass of water in all forms (e.g., crystal and liquid, and assuming that the rate of evaporation is much slower than the rate of crystallization). If the current liquid mass is

$\phi_t^L \rho^L \approx \phi_0 S_t^L \rho^L$ , the current ice mass is  $\phi_0 S_t^C \rho^C$ , the liquid mass at the previous time

step is  $\phi_0 S_{t-1}^L \rho^L$ , and the ice mass at the previous time step is  $\phi_0 S_{t-1}^C \rho^C$ , mass

conservation of water allows us to write

$$\phi_0 S_t^L \rho^L + \phi_0 S_t^C \rho^C = \phi_0 S_{t-1}^L \rho^L + \phi_0 S_{t-1}^C \rho^C, \quad (6.10)$$

where subscript  $t$  and  $t-1$  denote the current time step and the previous time step, respectively. Rearranging (6.10), the current ice saturation can be written in the form

$$S_t^C = S_{t-1}^C + (S_{t-1}^L - S_t^L) \frac{\rho^L}{\rho^C}. \quad (6.11)$$

Current gas saturation can then be determined as

$$S_t^G = 1 - S_t^C - S_t^L. \quad (6.12)$$

When concrete is partially saturated, expelled water from the freezing sites can flow towards the empty pores allowing the expansion caused by the density change in (6.11). Upon entering these empty pores with bigger radius than the freezing sites, since water evaporates from the biggest pore as dictated by (6.5), water freezes instantly. This entire freezing mechanism is shown in Figure 19. Therefore, the pore liquid can be considered to be bounded by ice on all sides and the equilibrium pressure of the liquid is dictated by the ice-liquid interface as given by (3.36), where ice is in contact with the wet air.

## 6.2 Concrete tank subjected to cryogenic temperatures

Concrete can undergo significant drop in temperature when it is used as the primary containment of LNG. In composite concrete LNG tanks the primary concrete wall is directly exposed to LNG on the inside surface, and wrapped with carbon-steel liquid and vapor barrier and perlite insulator on the outside surface [118] as shown in Figure 20 (a). The appropriate boundary conditions pertaining to this problem are depicted in Figure 20 (b). Such a problem can be modeled considering deformation in only one direction with a stress free surface which gives

$$\varepsilon_{yy} = \varepsilon_{zz} = 0, \quad (6.13)$$

and <sup>8</sup>

$$\sigma_x = T_{11} = 0. \quad (6.14)$$

Thus, the nonzero stresses and strains can be determined as

$$\sigma_y = T_{22} = \sigma_z = T_{33} = -3K \frac{(1-2\nu)}{(1-\nu)} \varepsilon_f \quad (6.15)$$

and

$$\varepsilon_{kk} = \varepsilon_{xx} = \frac{(1+\nu)}{(1-\nu)} \varepsilon_f. \quad (6.16)$$

Here,  $\sigma$  and  $\varepsilon$  stand for stress and strain, respectively, with subscripts  $x$ ,  $y$  and  $z$  denoting the three orthogonal directions. The term  $\varepsilon_{kk}$  denotes the bulk (volumetric) strain. For the inside surface exposed to cryogenic temperatures, if the temperature induced by the cryogenic liquid is termed as  $\theta_{cryo}$  and the reference temperature is chosen as  $\theta_m = 273 \text{ K}$  ( $0 \text{ }^\circ\text{C}$ ), we can write that

$$\theta_{(x=0,t)} = \theta_{cryo}. \quad (6.17)$$

The other side of the wall, on the other hand, assumes limited heat transfer due to the perlite insulator such that

$$\left( \frac{\partial \theta}{\partial x} \right)_{(x=d,t)} = \left( \frac{\partial \theta^p}{\partial x} \right)_{(x=d,t)}, \quad (6.18)$$

---

<sup>8</sup> Here, we've presumed that the pressure exerted by the LNG on the inner side of the tank is negligible. Depending on the depth of the LNG in the tank, this presumption may only apply nearer to the top of the tank.

where,  $\theta^P$  is the temperature in the perlite layer, and  $d$  stands for the thickness of the primary concrete containment wall. On the outer boundary of the perlite layer, temperature is assumed to be fixed at the reference temperature.

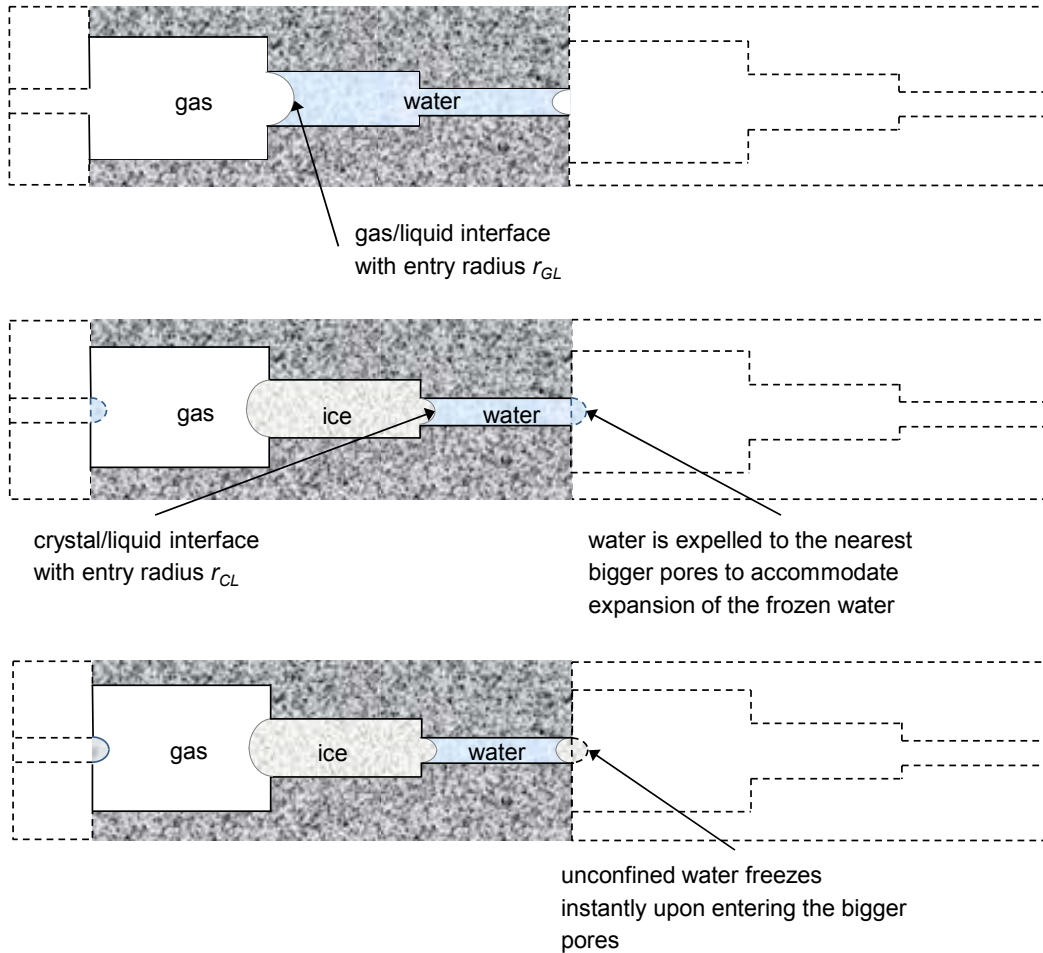


**Figure 19. Schematics of freezing mechanisms in partially saturated concrete**

### 6.2.1 Pore pressure in the fully saturated concrete

For the fully saturated non-air-entrained concrete, initial pore liquid pressure is in equilibrium with the atmospheric pressure ( $p_{atm}$ ),

$$p_{(x, t=0)}^L = p_{atm} \cdot \quad (6.19)$$

When the temperature is dropped below the melting point, water on the surface will freeze immediately setting ice in equilibrium with the atmospheric pressure so that

$$p_{(x=0, t)}^C = p_{atm} \cdot \quad (6.20)$$

Pore liquid pressure at the interior boundary can therefore be given by the water-ice thermodynamic condition (3.36)

$$p_{(x=0, t)}^L = -\frac{\rho^L}{\rho^C} \Sigma_m (\theta_m - \theta_{cryo}) + p_{atm} \cdot \quad (6.21)$$

On the outer surface where the concrete wall is water tight due to the carbon steel liner

$$\left( \frac{\partial p^L}{\partial x} \right)_{(x=d, t)} = 0. \quad (6.22)$$

In addition to the above mentioned boundary conditions, for the air-entrained concrete, due to the presence of the air bubbles, pore liquid pressure is relieved at a distance equivalent to the aggregate radius ( $r_i$ ) plus the air bubble spacing ( $L$ ), and therefore can be written as

$$p_{C(x=r_i+L, t)} = p_{atm} \cdot \quad (6.23)$$

such that, to meet the liquid-crystal thermodynamic equilibrium,

$$p_{(x=r_i+L, t)}^L = -\frac{\rho^L}{\rho^C} \Sigma_m (\theta_m - \theta) + p_{atm} \cdot \quad (6.24)$$

with  $\theta$  denoting the temperature at the air bubble surface. Condition (6.23) implies that the displaced unfrozen water freezes instantaneously upon entering the air-voids, and

assumes that these air-voids are large enough to accommodate indefinite growth of ice without confining it.

### 6.2.2 Pore pressure in the partially saturated concrete

Initially, pore liquid in the partially saturated concrete is in equilibrium with the pore gaseous phase, the initial pore liquid pressure is given by (6.4). Consequently, the initial liquid saturation can be obtained from (6.6). As the temperature drops below the freezing point, water will freeze in the bigger pores and expand. Liquid in the adjacent smaller pores will then flow to the nearest empty pores to accommodate this expansion. Since these empty pores are bigger than the currently freezing pores as water evaporates from the biggest pores imposed by (6.5), water will freeze instantly and reach equilibrium. As a result, pore liquid will be confined by the frozen ice crystals on all sides, and the pore liquid pressure is sustained by the liquid-ice interface. Assuming that the porous space never fills with ice completely, we can write

$$p^C = p^G = p_{atm}, \quad (6.25)$$

and

$$p^L = -\frac{\rho^L}{\rho^C} \Sigma_m (\theta_m - \theta) + p_{atm} \text{ everywhere in the partially saturated concrete}^9. \quad (6.26)$$

## 6.3 Results and discussions

To implement the proposed model, we consider a fully saturated 0.4 m thick concrete wall used for primary containment of LNG. Temperature at the interior surface,

---

<sup>9</sup> We assume that equilibrium is achieved instantly everywhere in the unsaturated strips of Figure 24.

i.e. at  $x=0$  in Figure 20 (b), is reduced at a rate of  $0.5 \text{ }^\circ\text{C/hr}$  [74] down to  $-150^\circ\text{C}$  from the reference temperature,  $\theta_m$ , taken as  $0^\circ\text{C}$ . As a design requirement practiced in field, we also consider that the primary concrete wall is insulated by a 1 m thick perlite layer [74]. Thermal properties of concrete and perlite used in this simulation are  $\phi^c = 2 \text{ W m}^{-1} \text{ K}^{-1}$ ,  $\phi^p = 0.04 \text{ W m}^{-1} \text{ K}^{-1}$ ,  $C_p^c = 0.75 \text{ J kg}^{-1} \text{ K}^{-1}$ ,  $C_p^p = 387 \text{ J kg}^{-1} \text{ K}^{-1}$ , with superscripts  $c$  and  $p$  denoting concrete and perlite, respectively. In addition, we let  $\rho^c = 2400 \text{ kg m}^{-3}$ ,  $\rho^p = 100 \text{ kg m}^{-3}$  as well as  $R_* = 0.05 \mu\text{m}$ ,  $m = 0.5$ ,  $\phi_0 = 0.15$ ,  $k = 1.7 \times 10^{-19} \text{ m}^2$ ,  $K_s = 45 \times 10^3 \text{ MPa}$ ,  $\alpha = 6 \times 10^{-6} \text{ }^\circ\text{C}^{-1}$ , and  $\nu = 0.2$ . Furthermore,  $\eta^L = 1.79 \times 10^{-3} \text{ Pa s}$  at  $0^\circ\text{C}$ ,  $K^L = 1.79 \times 10^3 \text{ MPa}$  and  $\alpha^L = -98.77 \times 10^{-6} \text{ }^\circ\text{C}^{-1}$  at  $-10^\circ\text{C}$  for supercooled water, and  $K^C = 7.81 \times 10^3 \text{ MPa}$  and  $\alpha^C = 51.67 \times 10^{-6} \text{ }^\circ\text{C}^{-1}$  at  $-10^\circ\text{C}$  for ice crystals are adopted [1]. Liquid density,  $\rho_L$ , and crystal density,  $\rho_C$ , are assumed to be  $999.8 \text{ kg m}^{-3}$  and  $916.7 \text{ kg m}^{-3}$  at  $0^\circ\text{C}$ , respectively [1]. Additionally,  $\Sigma_m$  is considered to be  $1.2 \text{ MPa }^\circ\text{C}^{-1}$  [1, 16], and liquid degree of saturation,  $S^L$ , is determined using the van Genuchten model [83] as described in section 4.2.

Intrinsic permeability, being a dominant material characteristic that governs the fluid transport in a porous body, affects the pore pressure and the tensile stresses substantially, as the liquid in pores transforms into crystals at freezing temperatures [119] or gas at constant or elevated temperatures [120, 121]. Relative permeability models [88, 93, 94] of unsaturated porous body, whose pore network is gradually invaded by solid crystals blocking the pore entry, are based on simple pore geometry and

do not represent the complex pore network of real materials, especially those with permeability less than  $10^{-14} \text{ m}^2$  [90-92, 95-97]. In addition, it is very likely that the extensive cooling to cryogenic temperatures, targeted in this work, will induce freezing damage creating macropores and lead to much more complex pore network, especially in partially saturated concrete where relative permeability is already a function of three phases coexisting in the pore network- water, ice, and humid air. Such complex permeability cannot be captured accurately using the simple models that are originally developed to model two-phase flow, and hence a constant permeability is used in this work knowing that the modeled results may inaccurately predict the pore pressure and tensile stresses (see section 4.3) obtained with the relative permeability functions available in literature. However, as claimed by Powers and Willis [2], ice blockage has negligible effect on permeability since the pore blocking effect may be offset by microcracking induced during the freezing process.

Since a high magnitude of pore pressure is expected to be developed as the temperature is dropped to  $-150^\circ\text{C}$ , and pore pressure and liquid saturation are interdependent, the Crank-Nicolson [122] scheme is used to numerically solve (3.40) for the pore fluid pressure field. For a fully saturated non-air-entrained concrete, boundary conditions (6.19) to (6.22) are utilized and the resulting temperature gradient, pore liquid pressure field, pore liquid saturation, bulk strains and vertical stress distributions are plotted in Figure 21. As we can see from Figure 21 (a), temperature gradient gradually increases as concrete is cooled to  $-150^\circ\text{C}$ , exhibiting higher temperature at the outer boundary than the surface directly exposed to the cryogenic temperature. When water

progressively transforms to ice, high hydraulic pressure is developed by the displaced unfrozen water due to the volume expansion of ice (Figure 21 (b)). This hydraulic pressure increases towards the outer boundary as the distance that the expelled water has to travel to the escape boundary increases. Consequently, the freezing temperature for ice crystallization at the outermost surface is suppressed by several degrees as shown in Figure 21 (c). Maximum expansion is therefore observed at the outer surface, developing peak compression. Once this hydraulic pressure dissipates at around  $-32^{\circ}\text{C}$ , almost 90% of the pore liquid freezes and uniform pore pressure is established everywhere. At this point, as most pores contain frozen ice, deformation caused by the thermal contraction of the ice and solid matrix surpasses the swelling caused by cryo-suction and the thermal expansion of liquid water on cooling (note the negative coefficient for supercooled water), and creates a strain gradient with a steady decrease towards the outer boundary. This strain gradient presented in Figure 21 (d) is mainly caused by the temperature gradient across the concrete wall shown in Figure 21 (a). Accordingly, peak tensile stress is developed in the vertical direction at the innermost surface directly exposed to cryogenic liquid (Figure 21 (e)).

For air-entrained concrete, in addition to the boundary conditions applied at the two outer surfaces, we assume that air bubbles are uniformly distributed with a spacing of  $250\mu\text{m}$ , and equilibrium is locally achieved by the ice boundary pressure at the air void surface governed by (6.24). Due to the presence of air voids, excess pore water quickly escapes to these air voids relieving the pore pressure (Figure 22 (a)), and freezes instantly. The resulting suction (Figure 22 (b)) draws water from the unfrozen pores to

the air-void surface, and expedites crystallization (Figure 22 (c)). Consequently, a gradual contraction (Figure 22 (d)) is observed, resulting in steady increase in stresses (Figure 22 (e)) along the  $Y$  and  $Z$  directions.

### 6.3.1 Effect of cooling rate

In order to demonstrate the effect of cooling rate the following material properties are assumed:  $R_* = 0.05 \mu\text{m}$ ,  $m = 0.5$ ,  $\phi_0 = 0.15$ ,  $k = 1.7 \times 10^{-19} \text{m}^2$ ,  $K_s = 45 \times 10^3 \text{MPa}$ ,  $\alpha = 6 \times 10^{-6} \text{°C}^{-1}$  and  $\nu = 0.2$ . LNG temperature is reduced at a rate of 0.5, 1, and 2 °C/hr. Values obtained at the innermost surface ( $x=0\text{m}$ ) directly exposed to LNG are shown by the solid black lines in Figure 23. Plots with triangular, circular, and square markers show results at the reverse side ( $x=0.4\text{m}$ ). As expected, identical temperature values are obtained for both the non-air-entrained and air-entrained concrete for the same cooling rate (Figure 23 (a)). However, high hydraulic pressure (Figure 23 (b)) is generated for the non-air-entrained concrete because pore liquid has to travel greater distance than the air-entrained concrete to relieve the pressure. This high pressure suppresses pore liquid freezing temperature (Figure 23 (c)) by several degrees. This suppression of crystallization is further elevated by higher cooling rate. Consequently, higher expansion is observed for higher cooling rate in non-air-entrained concrete as shown in (Figure 23 (d)). Therefore, high pore pressure is expected to develop for high cooling rate making concrete vulnerable to compressive failure. Once water in most pores freezes, and hydraulic pressure disappears, the porous body starts to contract at an accelerated rate. For faster cooling rate, high temperature gradient and high pore



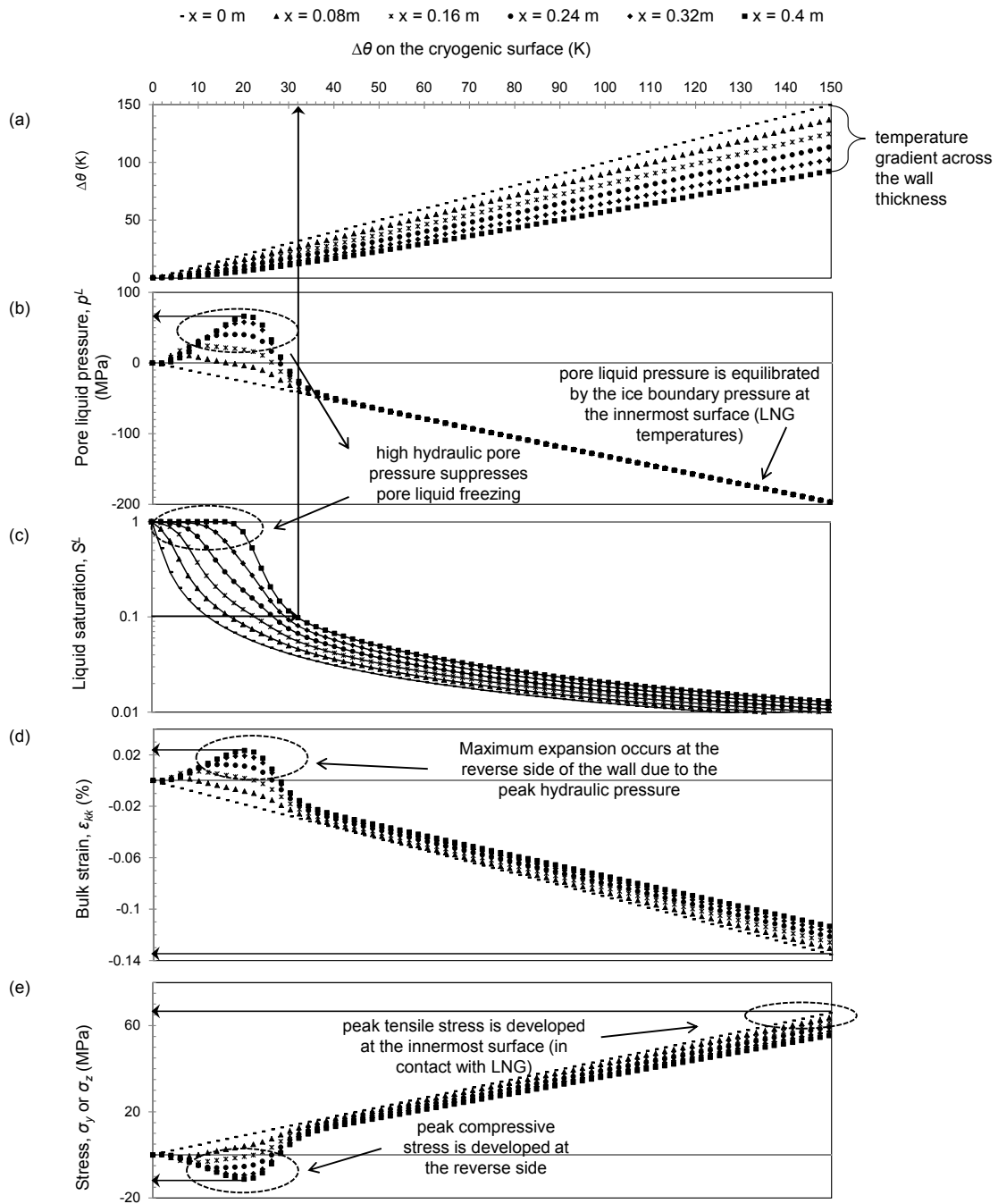


**Figure 21. (a) Temperature, (b) pore liquid pressure, (c) liquid saturation, (d) bulk strain, and (e) stresses in the Y and Z directions in a 0.4 m thick concrete (non-air-entrained) wall directly exposed to cryogenic temperature at  $x=0$  m. The concrete wall is simulated as liquid tight and insulated with perlite layer on the reverse side.**

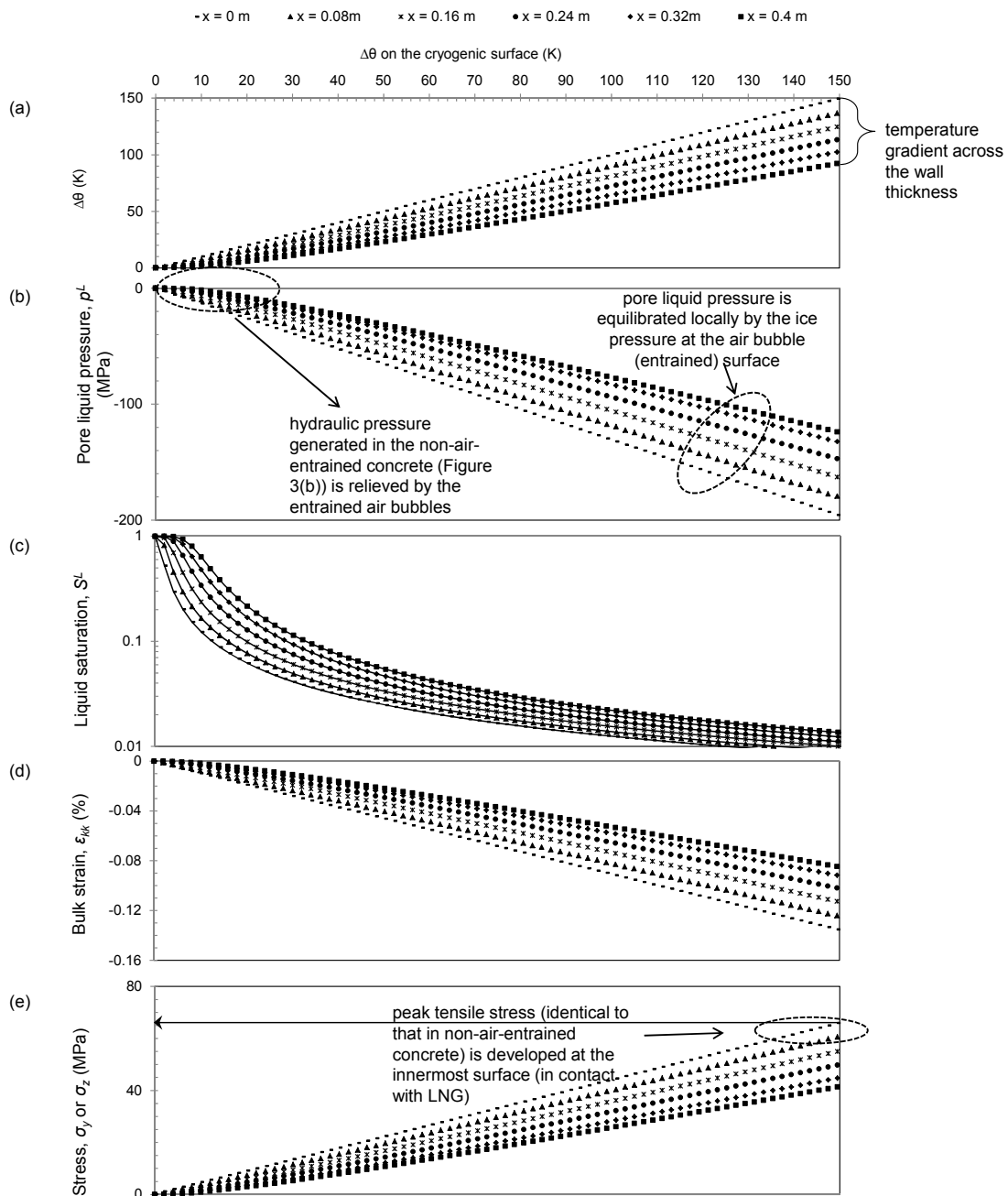


**Figure 22. (a) Temperature, (b) pore liquid pressure, (c) liquid saturation, (d) bulk strain, and (e) stresses in the Y and Z directions in a 0.4 m thick concrete (air-entrained) wall directly exposed to cryogenic temperature at  $x=0$  m. The concrete wall is liquid tight and insulated with perlite layer on the reverse side.**

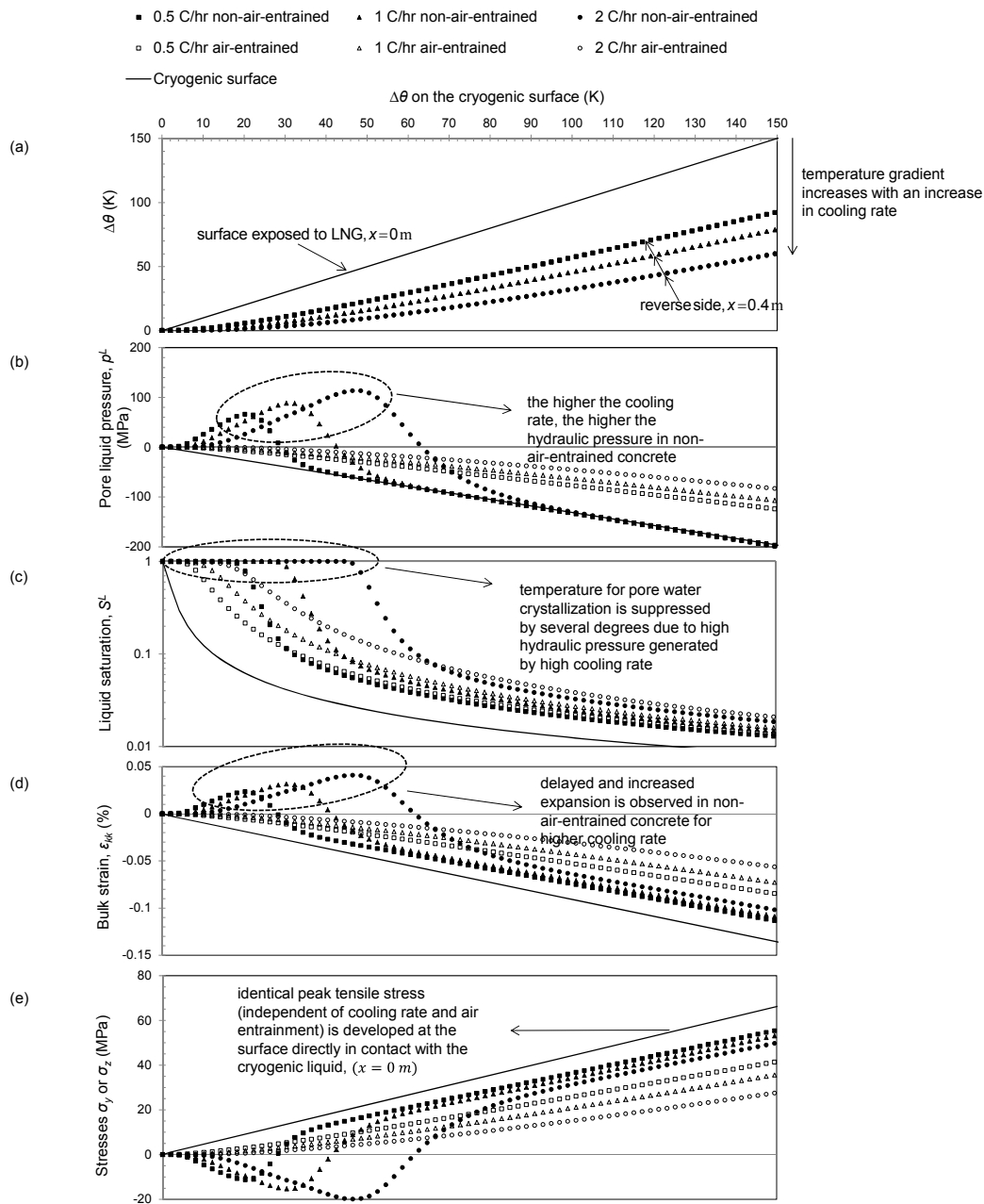


**Figure 23. Effect of cooling rate on (a) temperature profile, (b) pore liquid pressure, (c) liquid saturation, (d) bulk strain, and (e) stresses for non-air-entrained and air-entrained primary containment concrete wall. Plots with markers (solid and empty triangular, circular and square) represent variables at the reverse side of the wall ( $x=0.4\text{m}$ ). Solid line shows values at the innermost surface directly in contact with the LNG ( $x=0\text{m}$ ).**

### 6.3.2 Effect of moisture content

In the preceding section a completely saturated concrete wall is considered, which seldom represents the field condition. In reality, when exposed to the surrounding environment, a fully saturated concrete body dries out on the surface through evaporation of the pore liquid due to the decrease in relative humidity. In order to simulate this internal moisture gradient that arises through surface drying, a fully saturated concrete strip ( $S_L=1$ ) is considered to be bounded by unsaturated strips with  $S_L=0.8$  on both sides (as shown in Figure 24) such that the initial spatial mean liquid saturation is calculated to be 0.90. Furthermore, we assume the same concrete properties as before so that  $R_* = 0.05 \mu\text{m}$ ,  $m = 0.5$ ,  $\phi_0 = 0.15$ ,  $k = 1.7 \times 10^{-19} \text{ m}^2$ ,  $K_s = 45 \times 10^3 \text{ MPa}$ ,  $\alpha = 6 \times 10^{-6} \text{ }^\circ\text{C}^{-1}$  and  $\nu = 0.2$ . For the unsaturated strips, pore pressure is determined as prescribed in section 6.2.2, and for the middle saturated strip, pore pressure is determined the same way described in section 6.2.1 with the boundary values obtained from that calculated for the adjacent unsaturated strip. The resulting plots are shown in Figure 25. At the unsaturated zones, no hydraulic pore pressure is developed since the excess water is accommodated by the bigger pores emptied by drying. The saturated strip in the middle, however, showed slight increase in the pore pressure due to hydraulic expansion. Once this pore pressure is dissipated, and almost all pore water freezes, similar pore pressure profile, strain, and stresses to that for air-entrained concrete are observed. The comparative results for the mean (spatial average) pore liquid pressure, liquid saturation, bulk strain, and stresses (along the  $Y$  and  $Z$

directions) of the partially and fully saturated non-air-entrained concrete and fully saturated air-entrained concrete are shown in Figure 26. The mean of a function,  $f$ , is obtained through

$$\langle f \rangle = \frac{1}{d} \int_0^{x=d} f dx . \quad (6.27)$$

Here,  $d$  represents the thickness of the wall. As we can see, the mean peak hydraulic pore pressure is partially alleviated by the unsaturated concrete strips on both sides, and fully alleviated by the entrained air-bubbles in the air-entrained concrete. Also, air-entrained concrete shows less mean contraction than the fully saturated non-air-entrained concrete developing less mean stress along  $Y$  and  $Z$  directions. The predicted trend of constant rate of contraction for the air entrained concrete follows the same trend as experimental data (down to about  $-55$  °C) presented by [113]. However, Sun and Scherer [123] observed a significant deviation of the predicted results from the experimental data for air entrained mortar cooled below  $-25$  °C. Below this temperature, the measured strain was observed to plateau, whereas the calculated strain kept increasing as shown in Figure 26 (c). The authors [123] ascribed this discrepancy to rupturing of liquid water pockets, reduced suction of the air voids caused by blockage of the surface pores on the air voids and/or to the high hydraulic pressure triggered by the gradual propagation of macroscopic ice into the mesopores. However, as previously mentioned, the modeled strain qualitatively agrees with the measured strain reported by [113], indicating that the poroelastic theory adopted in this work is adequate in modeling the deformation of saturated air-entrained concrete cooled to cryogenic temperatures.

Nevertheless, in light of the conflicting data in the literature, it is evident that further investigation must be done to determine the significance and influence of the aforementioned mechanisms on the rate of contraction of air-entrained concrete at low temperatures (i.e., below about  $-25\text{ }^{\circ}\text{C}$ ).

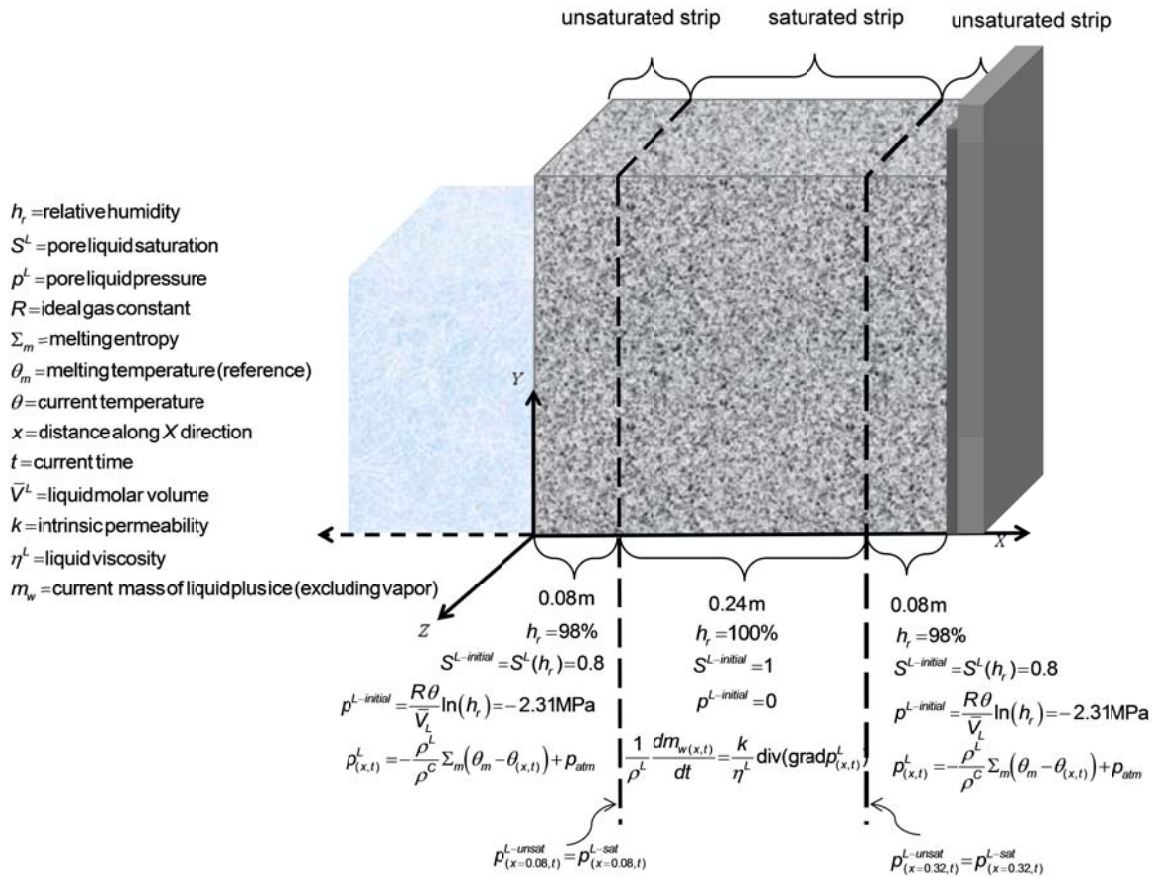


**Figure 24. Initial humidity and saturation profile for partially saturated concrete. The concrete wall cross-section consists of a fully saturated strip in the middle bounded by unsaturated strips on the boundaries.**

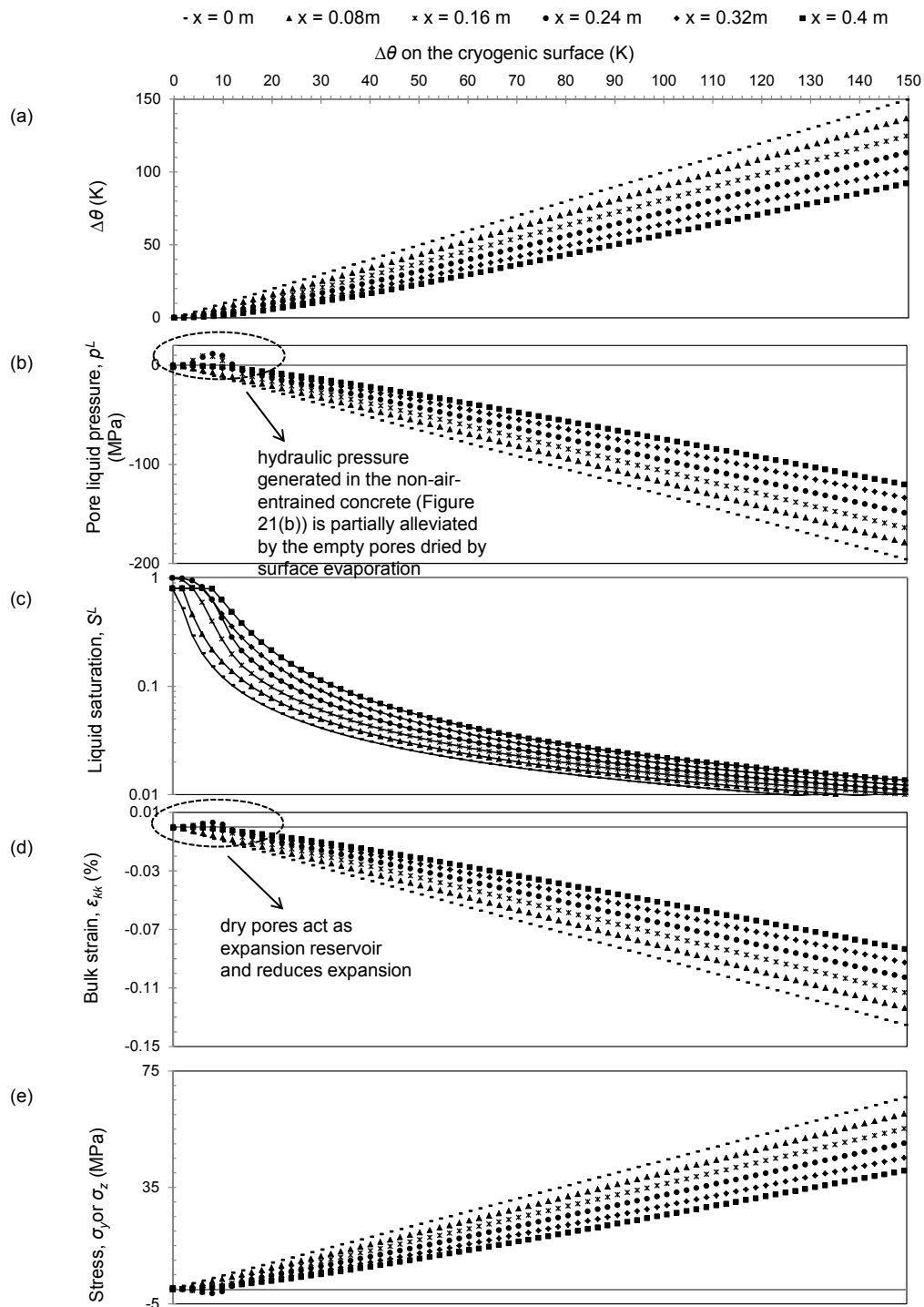


**Figure 25. (a) Temperature, (b) pore liquid pressure, (c) liquid saturation, (d) bulk strain, and (e) stresses in the Y and Z directions in a 0.4 m thick partially saturated non-air-entrained concrete wall.**

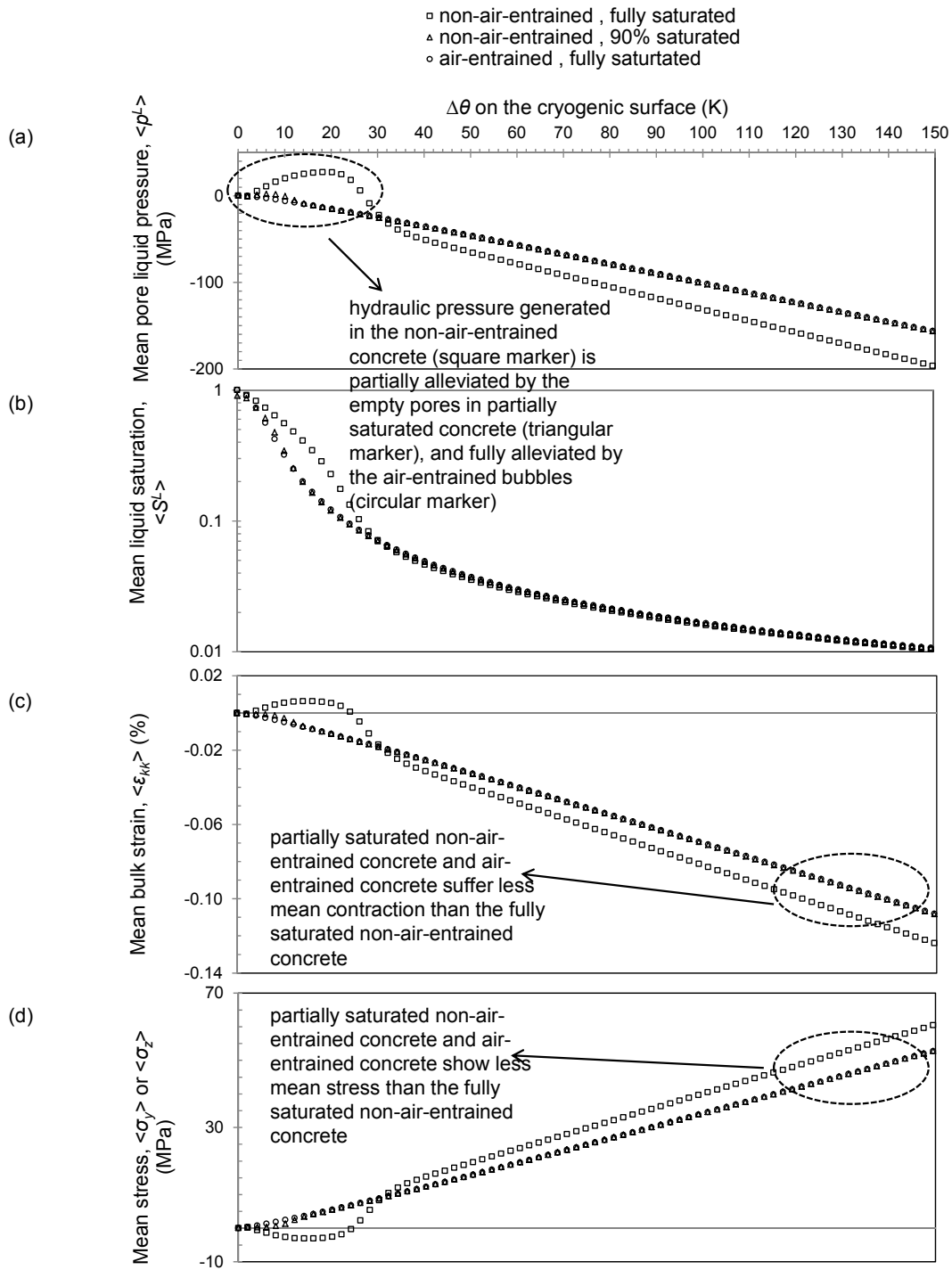


**Figure 26. (a) Spatial mean pore liquid pressure, (b) spatial mean liquid saturation, (c) spatial mean bulk strain, and (d) spatial mean stresses for fully and partially saturated non-air-entrained, and air-entrained primary containment concrete wall.**

### 6.3.3 *Effect of cryogenic swelling*

Several researchers have suggested that there has to be a liquid film separating the solid crystal and solid matrix wall to establish the thermodynamic equilibrium governed by the Thomson's equation (3.36) [77, 124-127]. For a continuous drop in temperature, equilibrium condition (3.36) requires the pressure difference  $p^C - \frac{\rho^C}{\rho^L} p^L$  ( $p_{atm}$  being taken as zero reference pressure) to increase, which is attained by drawing some extra liquid from the surrounding. In the already solidified pores at a temperature well below the bulk melting point, where there is no source of bulk liquid water or the entry channels are blocked by the frozen ice, this extra liquid is supplied by a premelted liquid film obtained from the solidified crystal itself [77, 127, 128]. This phenomenon, where liquid water is driven towards the already frozen pores, is known as cryo-suction, and the successive increase in the pressure difference results in cryogenic swelling of the porous body. Consequently, liquid saturation is constantly adjusted by this cryo-suction process to sustain the premelted liquid film around the solid crystal [42]. It has been proposed that the pressure associated with this liquid film is greater than the pressure of the bulk fluid located a long distance away from the interface [77]. The extra pressure associated with this thin film is referred to as disjoining pressure. The mobility of this thin film is reported to be significantly lower than the diffusion of the bulk water [32, 33]. Furthermore, due to the short travel distance, tortuous pore network, and mass of transported liquid being very limited, the assumption that the film remains static is fairly justifiable.

The poromechanical approach, as outlined by Coussy and applied in this work, hypothesizes that the pressure on the pore wall of the solid skeleton can safely be adopted as the crystal pressure,  $p^C$ , thus neglecting the effect of the disjoining pressure [77]. However, as pointed out by Scherer and shown later in section 7.2, this disjoining pressure provides an upper bound on the crystallization pressure [15], introducing discrepancies between the modeled results (that do not include the effect of disjoining pressure) and experimental data.

For a low-porosity porous material, cryoswelling and thermal expansion of the supercooled water may be offset by the thermal contraction of the solid matrix and the solid crystal as presented in Figure 21 (d). However, the opposite phenomenon can be observed if higher porosity material is considered (which is shown in Figure 27). For this simulation, we let  $R_* = 0.05 \mu\text{m}$ ,  $m = 0.5$ ,  $\phi_0 = 0.35$ ,  $k = 1.7 \times 10^{-19} \text{m}^2$ ,  $K_s = 45 \times 10^3 \text{MPa}$ ,  $\alpha = 6 \times 10^{-6} \text{C}^{-1}$ , and  $\nu = 0.2$ . Unlike the strain profile in Figure 21 (d), when temperature is dropped below  $-40^\circ\text{C}$ , and the pore pressure is uniform everywhere, the interior surface contracts less in spite of exhibiting lower temperature than the outer boundary. In this case, the effect of cryo-swelling is intensified by the high porosity, surpassing thermal contraction of the solid matrix and ice crystal. As a result, peak tensile stress is observed at the outer boundary of the concrete wall, which is contrary to what we find for a low porosity material. It is worth noting that a maximum hydraulic pore pressure of about 118 MPa and a thermal contraction of about  $-0.2\%$  are developed at the outer boundary for the high porosity ( $\phi_0 = 0.35$ ) concrete (Figure 27

(b)), which is much higher than that (about 65 MPa and  $-0.135\%$ ) obtained for the low porosity ( $\phi_0 = 0.15$ ) concrete (Figure 21 (b)). On the other hand, at  $-150^\circ\text{C}$ , a maximum tensile stress of around 67 MPa (Figure 21 (e)) is observed at the interior surface of the wall directly exposed to the cryogenic liquid for the low porosity ( $\phi_0 = 0.15$ ) concrete, while a tensile stress of about 38 MPa (Figure 27 (e)) is calculated for the high porosity ( $\phi_0 = 0.35$ ) concrete with a peak tensile stress of 56 MPa at the outermost surface. This reduced stress coupled with high deformation can be linked to the reduction in bulk modulus of the porous body ( $K$ ) due to the increase in porosity. The high stress values reported in this work may be due to the fact that the current model does not include the viscoelastic relaxation and therefore over predicts the actual values encountered in the field. Furthermore, the creation of new macropores induced by the freezing damage may increase permeability and may considerably diminish the destructive tensile stresses at cryogenic temperatures.

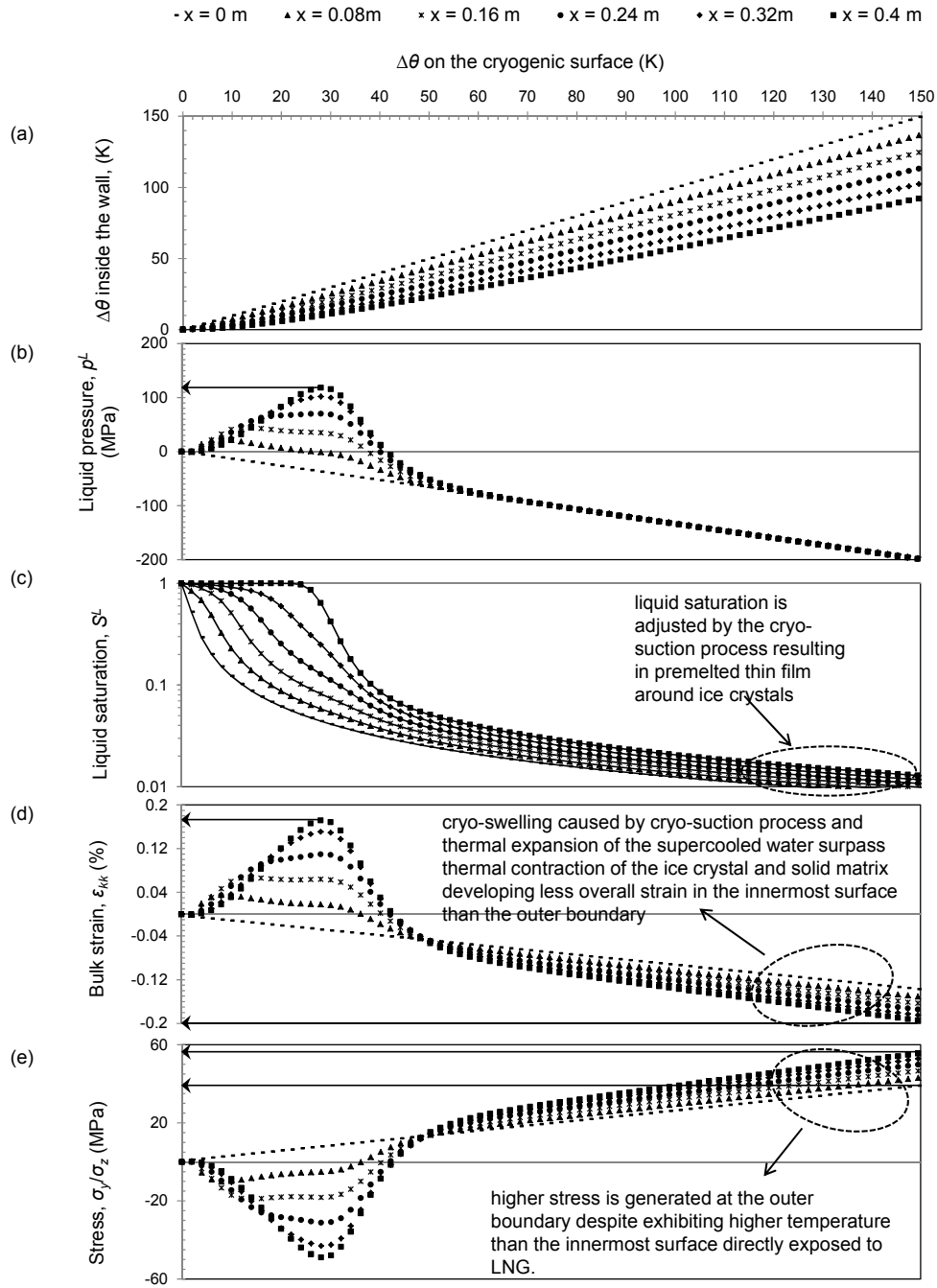


**Figure 27. Effect of cryo-swelling on the deformation of cryogenic concrete. The wall surface in contact with the cryogenic fluid contracts less than the outer boundary (d) because of the cryo-swelling induced by the thermodynamic equilibrium and the subsequent cryo-suction.**

## 6.4 Summary

The theory of poroelasticity is extended to simulate the thermal expansion and stresses at the bottom of the concrete wall in the LNG storage tank. The simulated results are analyzed for fully and partially saturated non-air-entrained concrete and fully saturated air-entrained concrete. Effect of cooling rate is also demonstrated. It is found that high cooling rate results in high expansion provoked by high hydraulic pore pressure and the corresponding suppression of pore liquid freezing temperature. It is also revealed that air-entrained concrete, by allowing quick dissipation of the displaced pore water and accommodating the ensuing ice formation, shows less contraction and subsequently less crack initiating stresses than the high-porosity, non-air-entrained concrete. Similar outcomes are observed near the concrete surfaces subjected to evaporation prior to cryogenic freezing. High hydraulic pressure, induced by the delayed dissipation of excess pore water, is likely to generate at the center of surface dried concrete walls.

## 7 PREDICTING SHIFTS IN FREEZING POINT DUE TO LIQUID CONFINEMENT AND PORE SOLUTION SPECIATION

The solid-liquid thermodynamic equilibrium equation, extended in section 3.1, is applied here to evaluate the influence of both the disjoining pressure and dissolved ions on the freezing point. Effect of dissolved ions on the shifting of pore liquid freezing and the subsequent effect on the deformation in concrete due to freezing are presented in section 7.1. Section 7.2 presents the influence of the disjoining pressure on the shifting of pore fluid and the deformation of freezing porous concrete. Comparison with the literature data is provided in section 7.3.

### 7.1 Effect of dissolved species

For simulations, we adopted the following values related to the porous body:

$\phi_0 = 0.26$ ,  $K_s = 31.8 \text{ GPa}$ ,  $\alpha = 14.5 \times 10^{-6} \text{ }^\circ\text{C}^{-1}$  and  $\nu = 0.2$ . Furthermore, we let  $K^L = 1.79 \text{ GPa}$  and  $\alpha^L = -98.77 \times 10^{-6} \text{ }^\circ\text{C}^{-1}$  at  $-10^\circ\text{C}$  for supercooled water, and  $K^C = 7.81 \text{ GPa}$  and  $\alpha^C = 51.67 \times 10^{-6} \text{ }^\circ\text{C}^{-1}$  at  $-10^\circ\text{C}$  for ice crystals [1].  $\bar{S}_0^L$  is determined using the formula

$$\bar{S}_0^L = \sum_{i=1}^n \bar{N}^{L-i} \bar{S}_{0*}^{L-i} - R \sum_{i=1}^n \bar{N}^{L-i} \ln \bar{N}^{L-i}, \quad (7.1)$$

where  $i$  includes all the species in the liquid phase including water. For calculating  $\bar{S}_0^L$ , we assume  $\bar{S}_{0*}^{L-\text{H}_2\text{O}} = 69.9 \text{ J/mol/K}$  and  $\bar{S}_{0*}^{L-S} = \bar{S}_{0*}^{\text{solute}} = 72.11 \text{ J/mol/K}$  for the pure components. In addition, we use  $\bar{S}_0^C = \bar{S}_0^{C-\text{H}_2\text{O}} = 44.8 \text{ J/mol/K}$  and  $R = 8.3144 \text{ J/mol/K}$ .

The resulting saturation degree, pore pressure, and the strain diagrams are shown in Figure 28. It can be seen that an increase in the salt concentration decreases pore water freezing temperature and limits the crystal saturation,  $S_c$ . However, high pore pressure still builds up resulting in high expansion for concrete specimens saturated with high concentration NaCl solutions. This contradicting phenomenon, where higher expansion is observed for lower ice volume fraction, can be attributed to the reduction in liquid volume due to the increase in salt concentration. For this particular problem, this dependency of volume on the salt concentration is defined by the following function fitted to the experimental data [28]

$$\bar{V}_0^L = \bar{V}_0^{L-H_2O} + \frac{m_1 x}{1 + m_2 x}, \quad (7.2)$$

where  $m_1 = -20.618$  and  $m_2 = 4.215$  for NaCl solution. Furthermore, we assume,

$$\bar{V}_0^{L-H_2O} = 18.07 \text{ cm}^3/\text{mol} \text{ and } \bar{V}_0^{C-H_2O} = 19.73 \text{ cm}^3/\text{mol}.$$

According to this relation, an increase in molar fraction of the dissolved ions,  $x$ , results in a net decrease in the molar volume of the pore solution. The dependency of the molar fraction on the liquid saturation is obtained using the formula

$$x = \frac{\sum_{i=1}^n N^i}{\sum_{i=1}^n \beta^i \left( \sum_{i=1}^n N^i + N^{H_2O} S_L \right)}. \quad (7.3)$$

As ice crystallizes in the pore network, more solvent (i.e. liquid water) is taken away from the solution, and thus the molar fraction of the salt increases with the diminishing liquid saturation. For modeling purposes, we determined  $S_L$  using an

empirical constitutive relation proposed by van Genuchten, [83]. Figure 29 graphically illustrates how the decreasing molar volume of the solution contributes to the hydraulic pressure as the temperature drops below the melting point. The ratio,  $\frac{\bar{V}_0^C}{\bar{V}_0^L}$  defines the density differences between the pore solution and the crystal. Due to this density discrepancy, expansive hydraulic pressure builds up in the pore network. When  $\frac{\bar{V}_0^L}{\bar{V}_0^C} = 1$  is unity, no hydraulic pressure is generated (note that (3.45) becomes null). For pure liquid water and pure ice crystals,  $\frac{\bar{V}_0^L}{\bar{V}_0^C} \approx 1.09$ . In contrast, for a mixture of saltwater and pure ice,  $\frac{\bar{V}_0^L}{\bar{V}_0^C} > 1.09$ , with the magnitude increasing as more pure ice precipitates out of the salt solution, which increases the molar concentration of salt (and thus the overall liquid density) in the remaining solution. The more  $\frac{\bar{V}_0^L}{\bar{V}_0^C}$  deviates from unity, the higher the magnitude of hydraulic pore pressure. As a result, as the salt concentration increases with decreasing liquid volume, elevated expansion is observed making the material more susceptible to freezing damage. In a very recent study, acoustic emission activities were detected for mortar specimens saturated with high concentration NaCl solutions [129]. The expansive hydraulic pressure might be the reason why even with the suppressed ice growth, higher concentration NaCl solutions cause more damage than the pure water. It is also interesting to note that the magnitude of the maximum strain and pore pressure not only depends on the solute concentration but also on the lowest temperature to which

the specimen is exposed. Figure 28 shows that concrete filled with pure water exhibits the maximum expansion below  $-15^{\circ}\text{C}$ , whereas between  $-15^{\circ}\text{C}$  to  $-20^{\circ}\text{C}$ , 3% or 6% salt solution seem to be the most detrimental. Concrete saturated with 15% NaCl solution, on the other hand, develops the maximum damaging expansion when the temperature is dropped further below  $-20^{\circ}\text{C}$ . It is therefore possible to obtain an optimum salt concentration for which the maximum damaging expansion can occur for saturated concrete exposed to a certain minimum temperature.

Another set of data are plotted in Figure 30 where all the parameters used to model Figure 28 were utilized, except a finer pore size distribution is simulated in this case. Here we see that because of the finer pore sizes, the crystal saturation is suppressed so much that the influence of the hydraulic pressure is overcome resulting in less expansion for concrete specimens with high salt concentration than for those with pure water. Thence, whether the specimen saturated with salt concentration will expand more or less than that filled with pure water depends on multiple factors: hydraulic pressure due to the density differences between the pore solution and ice crystals, amount of ice in the pore volume, thermal expansion and contraction of the various constituents, suction of pore liquid to the already frozen pores, and the interfacial interactions between the various phases. Which of these mechanisms will dominate is dictated by the constituent properties, the pore characteristics of the porous body, solute concentration in the pore solution, and the lowest temperature applied to the concrete. An example of the significance of properties of material constituents on the deformation of the porous body is presented in Figure 31. Figure 31 shows that despite generation of the same pore

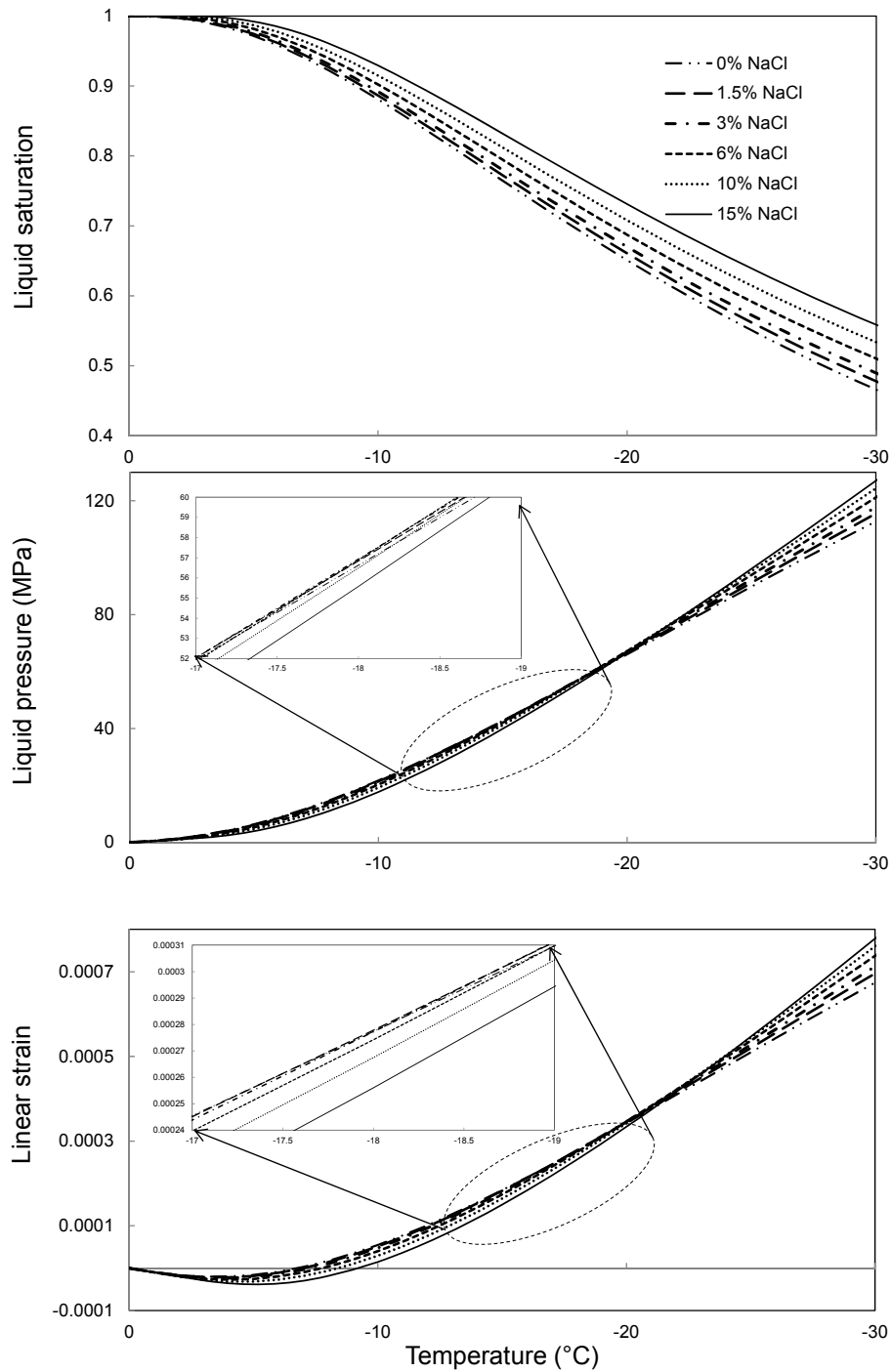


**Figure 28. Effect of salt concentrations in pore solution on the liquid saturation, pore pressure, and strain of a sealed concrete specimen. Depending on the minimum temperature to which concrete is exposed, an optimum salt concentration is possible to achieve that causes maximum strains.**

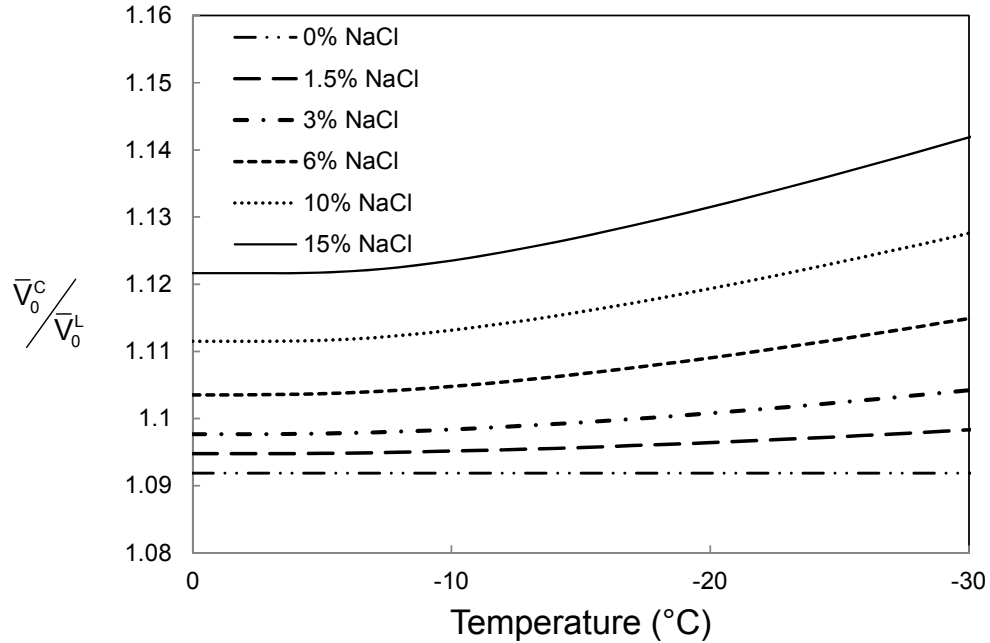


**Figure 29. Change in volume of the pore solution with temperature for varying salt concentrations.**

pressure for materials with two different porosities ( $\phi_0 = 0.26$  and  $\phi_0 = 0.13$ ), reducing the porosity by half can reduce the effect of hydraulic pressure and cause contraction rather than expansion of the porous body. Hence, reduction in porosity by lowering the water to cement mass ratio or by using supplementary cementitious materials will not only safeguard concrete from harmful substances invading the pore network, but also reduce the damage susceptibility by lowering the expansion. One should note here that both Figure 30 and Figure 31 consider the influence of disjoining pressure (which is discussed in the following section) in addition to the effects of pore solution speciation in determining the liquid-crystal phase transition.

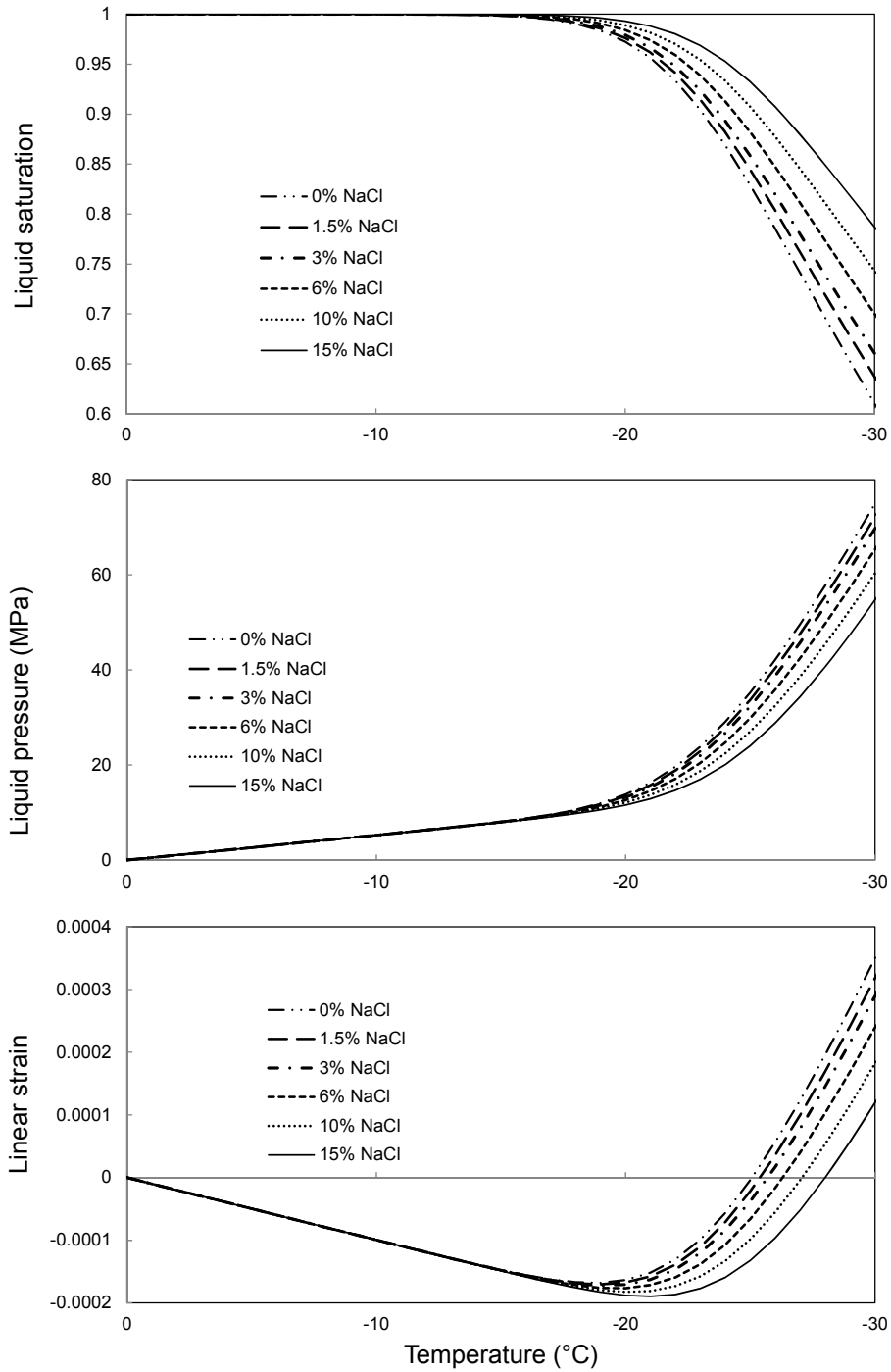


**Figure 30. Effect of salt concentrations in pore solution on the liquid saturation, pore pressure, and strain of a sealed concrete specimen with fine pore structures.**

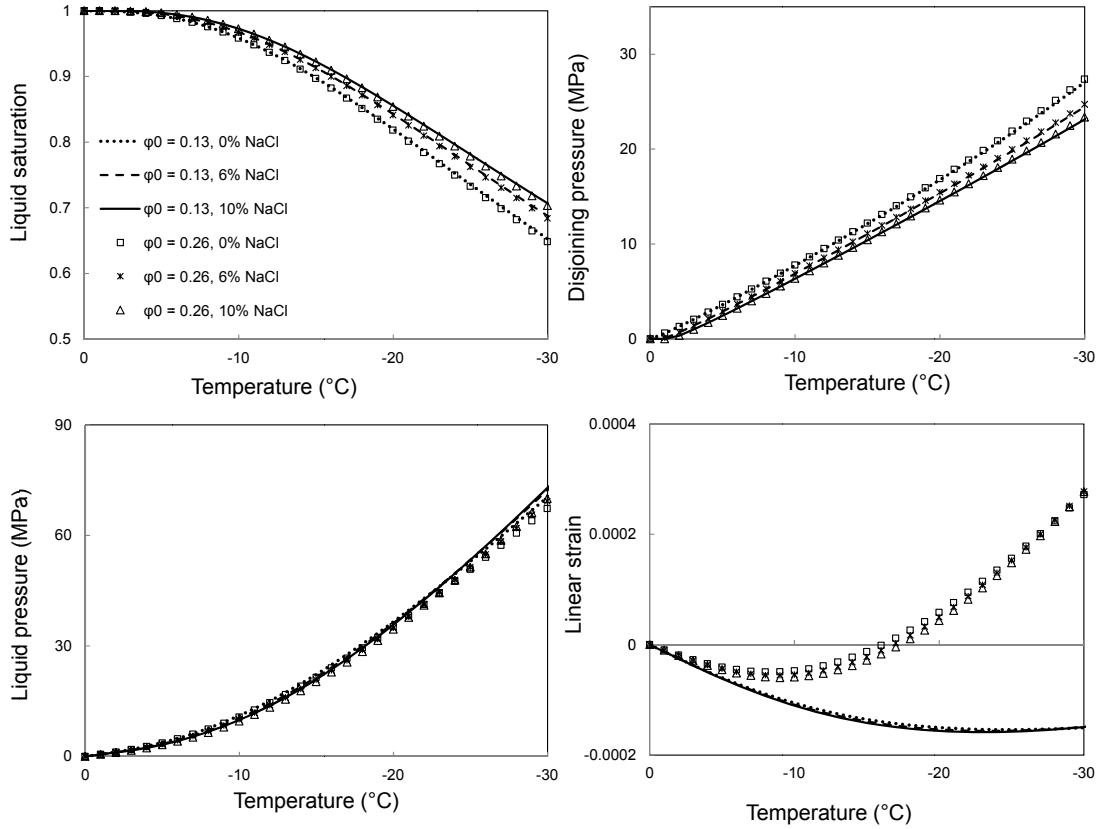


**Figure 31. Effect of porosity on the liquid saturation, disjoining pressure, pore liquid pressure, and strain of concrete specimens. Reduction in porosity can reduce the expansion significantly by reducing the effect of hydraulic pressure.**

## 7.2 Disjoining pressure and its contribution to crystal growth

If we neglect the presence of dissolved ions in the pore solution, equation (3.29) can be rearranged to read

$$\Sigma_m (\theta_m - \theta) = -(\sigma^C - \sigma_0) + \frac{\bar{V}_0^L}{\bar{V}_0^C} (\sigma^L - \sigma_0) + \frac{\bar{V}_0^L}{\bar{V}_0^C} \frac{s^L \cdot s^L}{4G^L}. \quad (7.4)$$

Equation (7.4) implies that the freezing point depression is not only a function of the pressure in the crystal, but also the stress states in the liquid.

Scherer [15] presented a comprehensive study of crystal growth and the associated crystallization pressure in porous materials. He stressed that the crystallization pressure is extensive when crystals grow in small pores. When a spherical crystal approaches the inner surface of the pore wall, the crystal-pore wall interface energy will prohibit it from making direct contact with the solid pore surface. It is this energy incompatibility between the solid wall and ice crystal interface that contributes to crystallization pressure and extracts liquid into the gap between them. As a result, crystals can continuously push the pore wall across the thin liquid film and grow. This liquid film, when a few nanometers thick, can amplify the magnitude of repulsion by generating hydration forces related to the electrostatic repulsion or ordered layering of solvent molecules. Big pores, on the other hand, can accommodate this crystal growth without generating such damaging stress. If the energy mismatch between the pore wall and the crystal is surmounted, direct contact occurs between the pore wall and the crystal, and the crystal ceases to grow.

Because of this repulsive force, (often referred to as disjoining pressure [15, 28]) the liquid film exhibits higher pressure than that in the bulk liquid (e.g. the point E in Figure 32(a)). As a result, this pressure gradient will expel liquid from the gap between the pore-wall and crystal to the bulk liquid. Since the mobility of this thin film is orders of magnitude lower than the bulk liquid, the liquid has to respond as a shear resistant material rather than a Newtonian or Navier-Stokes liquid. The resulting stress components  $T_{ij}^L$  in the liquid film thus can be presented as (Figure 32(b))

$$T_{rr} = -p^L - p^d \text{ and } T_{\theta\theta} = T_{zz} = -p^L \quad . \quad (7.5)$$

The mean stress,  $\sigma^L$ , and the deviatoric stress components,  $s_{ij}^L$ , respectively, can be written as

$$\sigma^L = -p^L - \frac{p^d}{3}, \quad s_{rr}^L = -\frac{2}{3}p^d, \quad \text{and} \quad s_{\theta\theta}^L = s_{zz}^L = \frac{1}{3}p^d \quad (7.6)$$

As uniform pressure is approximated to exist everywhere in the crystal, the mean stress in the crystal can be given as

$$\sigma^C = -p^C \quad \text{with} \quad s_{ij}^C = 0. \quad (7.7)$$

Substitution of (7.6) and (7.7) in (7.4) gives

$$\Sigma_m (\theta_m - \theta) = (p^C - p^L) + \left(1 - \frac{\bar{V}_0^L}{\bar{V}_0^C}\right) (p^L - p_0) - \frac{\bar{V}_0^L}{\bar{V}_0^C} \frac{p^d}{3} + \frac{\bar{V}_0^L}{\bar{V}_0^C} \frac{(p^d)^2}{6G^L} \quad (7.8)$$

Thus the repulsive force across the liquid film plays an important role in shifting the freezing point of pore liquid. Earlier in the derivation of equation (3.29) we neglected the elastic energy associated with higher order stress terms. Here, however we cannot do the same as studies showed that the elastic shear modulus of nanoconfined water can be at least three orders of magnitude smaller than the shear modulus of silicon (50 GPa) [130]. The third term on the right hand side of (7.8) stimulates crystal growth whereas the fourth term subdues the freezing point. As a net effect, disjoining pressure would always promote crystal propagation as long as the condition,  $2G^L p^d > (p^d)^2$  is satisfied.

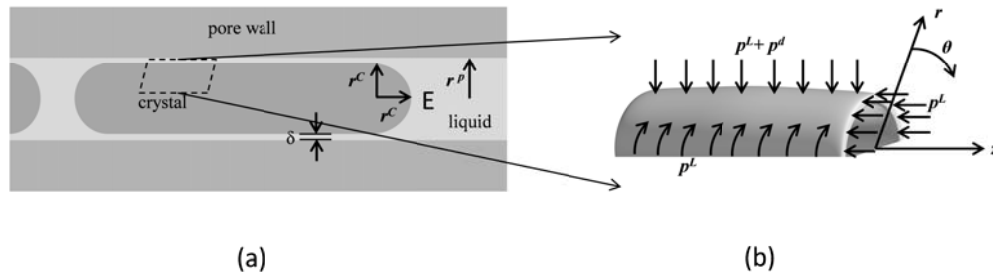


**Figure 32. Schematics of stress distribution in liquid film due to repulsive force acting within the film.**

Scherer (1999) correlated  $p^d$  to the ratio of the surface energy of the crystal surface and the distance from the centroid to the surface, i.e.  $\frac{\gamma_i^{CL}}{r_i}$ , where  $i$  denotes the  $i$ th family of the crystal planes. This correlation is pertinent for all polyhedral crystals in equilibrium. Thus, for a crystal growing in a cylindrical pore, the disjoining pressure,  $p^d$ , can be derived as [15, 28]

$$p^d = \frac{\gamma^{CL}}{r^p - \delta}. \quad (7.9)$$

Here,  $\delta$  is the thickness of the thin layer of the unfrozen pore solution between the crystal and the pore wall. Fagerlund [131] suggested an empirical relation to roughly estimate  $\delta$  as a function of temperature suppression given by

$$\delta = 19.7 \sqrt[3]{\frac{1}{\Delta\theta}} \text{ in } (\text{\AA}). \quad (7.10)$$

Figure 33 compares liquid saturation, pore liquid pressure and strain for two scenarios: 1) disjoining pressure calculated according to (7.9) and 2)  $p^d = 0$ . Data were

plotted for the same material constituents with three different pore solution concentrations, 0%, 6% and 10% NaCl. It has been found that the repulsive force across the liquid film enhances crystal growth as explained above and hypothesized by Scherer [15]. Consequently, an upper bound was obtained for both the liquid pressure and strains in concrete. Omission of disjoining pressure from the liquid-crystal thermodynamic relation will under predict the expansion and the hydraulic pressure in the porous body.

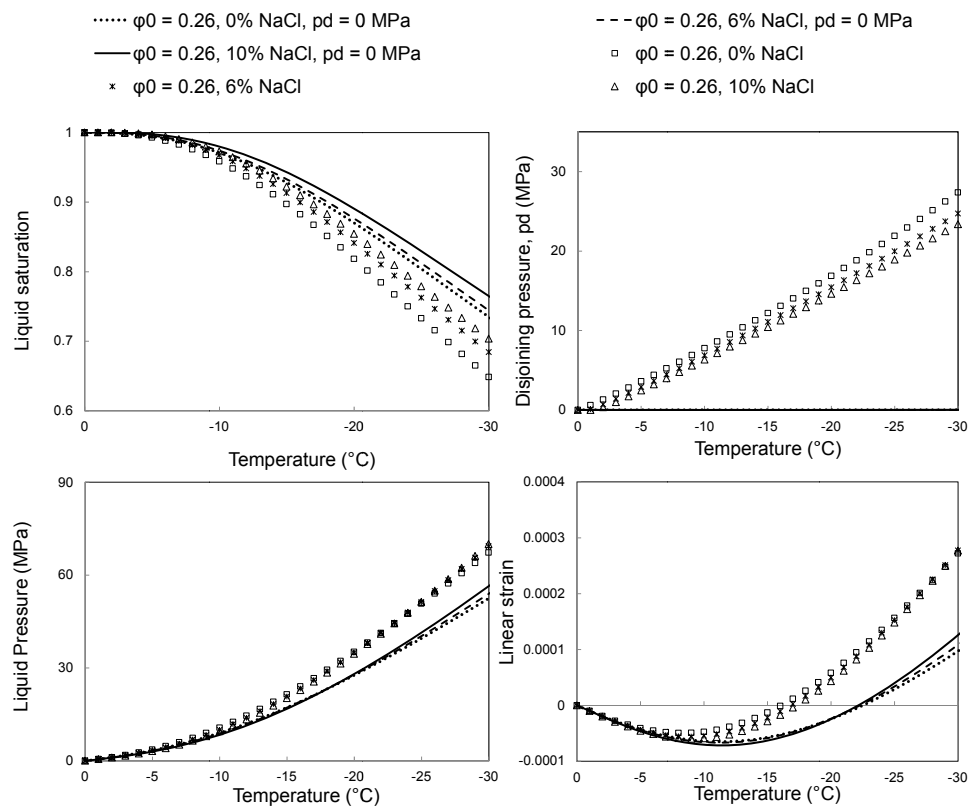


**Figure 33. Effect of disjoining pressure on ice propagation, pore pressure, and strain. Disjoining pressure favors crystal growth and increases the magnitude of the hydraulic pressure and strain.**

### 7.3 Comparison with literature data

The model veracity is assessed by comparison with experimental data found in the literature [132]. The primary reason for choosing these particular data is that the

authors used poroelasticity to determine deformation of concrete specimens, and documented the relevant input parameters that are also employed by our analysis. Liquid saturation data were also presented as function of temperature. We used the same liquid saturation profile to simulate the results. The resulting simulations are plotted in Figure 34 and Figure 35. Parameters used to plot Figure 34 are  $\phi_0 = 0.26$ ,  $K_s = 31.8 \times 10^3$  MPa,  $\alpha = 14.5 \times 10^{-6} \text{ } ^\circ\text{C}^{-1}$  and  $\nu = 0.2$ . For Figure 35,  $\phi_0 = 0.13$ ,  $K_s = 31.8 \times 10^3$  MPa,  $\alpha = 17.7 \times 10^{-6} \text{ } ^\circ\text{C}^{-1}$  and  $\nu = 0.2$  are adopted. It has been found that the model deviates from the experimental results for the high porosity material (Figure 34) but matches well with that for the low porosity, fine pore structured specimen (Figure 35). One plausible reason that the model predictions deviate from the experimental data is that the model is very sensitive to the liquid saturation and pore characteristics. For both sets of data, liquid saturation was estimated from the pore size distribution obtained from the mercury intrusion porosimetry (MIP) test. MIP falsely estimates macropores by characterizing them by the size of their largest entry radius [133], and therefore could cause the discrepancies between the modeled strains and strains obtained from experimentation. Overall, however, the model predictions herein – which consider the simultaneous effects of pore solution speciation and disjoining pressure – improve upon past modeling efforts that do not fully consider such effects.

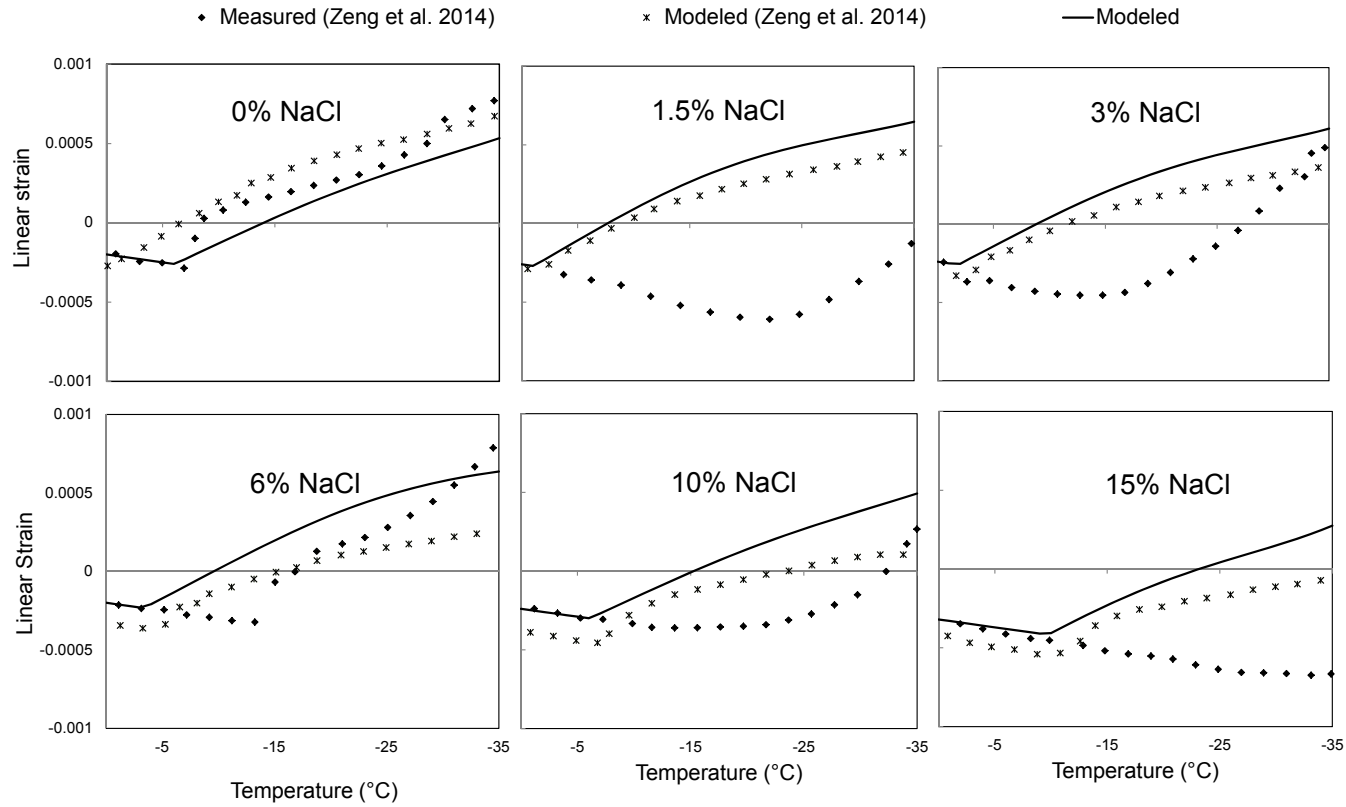


**Figure 34. Comparison of the modeled results with the experimental data found in [132]. Material properties used for simulation are  $\phi_0 = 0.26$ ,  $K_s = 31.8 \times 10^3 \text{ MPa}$ ,  $\alpha = 14.5 \times 10^{-6} \text{ }^\circ\text{C}^{-1}$  and  $\nu = 0.2$ .**

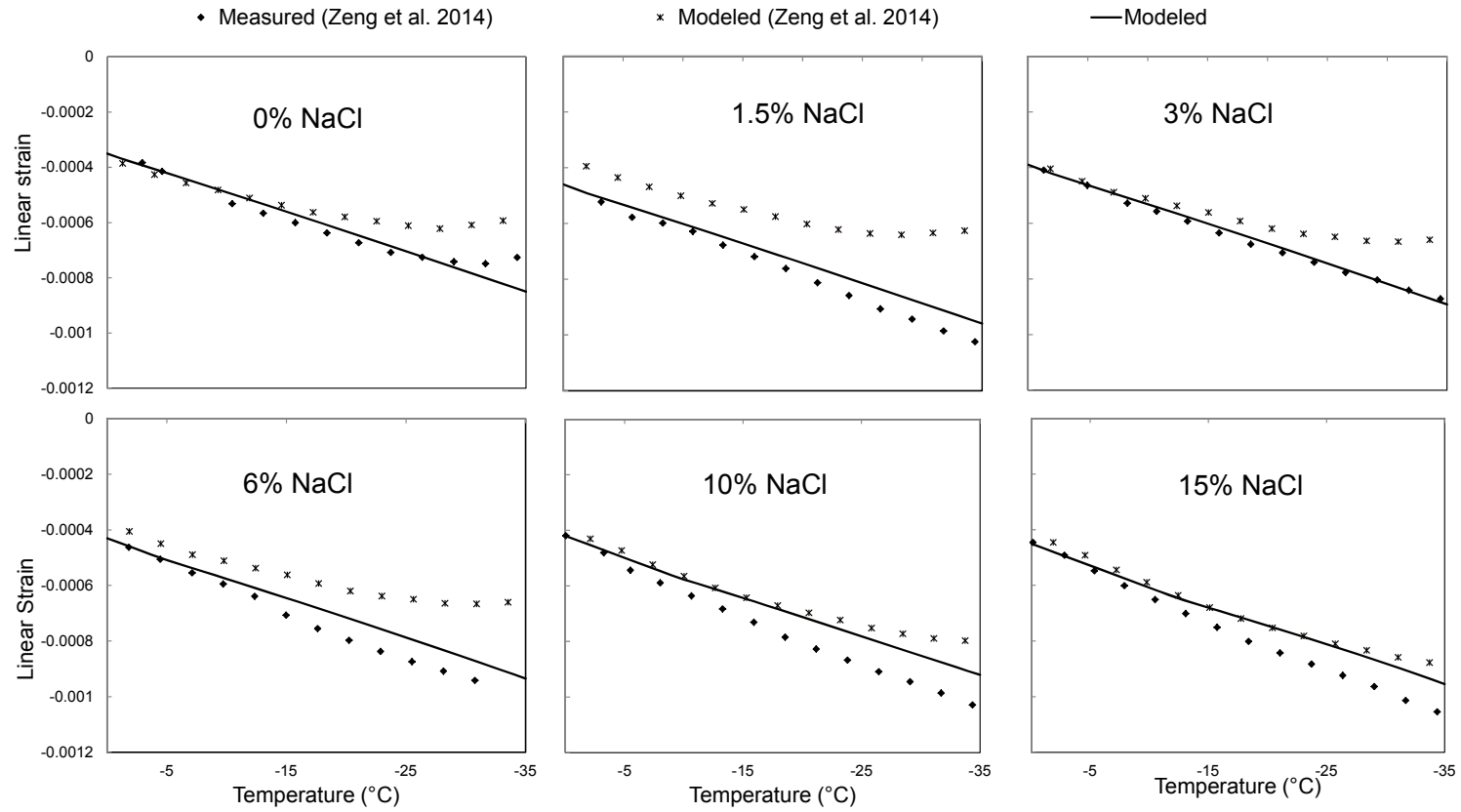


**Figure 35. Comparison of the modeled results with the experimental data found in [132]. Simulation was performed for  $\phi_0 = 0.13$ ,  $K_s = 31.8 \times 10^3$  MPa,  $\alpha = 17.7 \times 10^{-6} \text{ } ^\circ\text{C}^{-1}$  and  $\nu = 0.2$ .**

## 7.4 Summary

A simple pore solution containing dissolved NaCl is adopted here to demonstrate the effect of dissolved ions and disjoining pressure on the pore liquid freezing and deformation of porous concrete. We show that the repulsive, disjoining force that acts across the thin film between the crystal and pore wall favors crystal growth, while the dissolved ions suppress the freezing point. We also show that, even with the suppressed freezing temperatures, concrete saturated with solution may still exhibit expansion due to high hydraulic pressure build up in the pore network. The magnitude of the maximum pore pressure and the resulting expansion depends on the concrete constituent properties, pore characteristics, solute concentration, and the lowest temperature to which concrete is exposed.

## 8 CONCLUSIONS

Concrete, due to its widespread availability, casting simplicity, and economy, is the most used construction material in the world. Because of its very diverse constituents, concrete responses to environmental stimuli are also very versatile. As a result, when concrete is cooled from room temperature to cryogenic temperatures, depending on the constituent properties and environmental exposure, different forms of deformation and damage can be manifested. Testing of concrete responses to freezing temperatures is expensive, time consuming, and requires rigorous maintenance. A model capable of simulating stresses and strains in concrete cooled to freezing temperatures, that can incorporate concrete constituent properties and pore solution characteristics to mimic the experimental findings, is attractive. Thus, poroelasticity is utilized to model concrete for two purposes: 1) concrete pavement exposed to freezing and thawing actions and 2) concrete used for building containment tanks for storing cryogenic liquids such as LNG. Furthermore, the solid-liquid thermodynamic equation has been developed to incorporate the effect of pore solution speciation and disjoining pressure on the pore liquid freezing and the subsequent deformation of freezing concrete. Sensitivity analysis has been performed to identify the key constituents and factors that affect the magnitude of the damage initiating tensile stresses and strain induced in concrete by freezing actions. The most important conclusions derived from this study can be categorized into the following divisions:

- Identifying deleterious aggregates susceptible to frost damage

- Determining optimum air void spacing specific to a concrete mixture design and environmental exposure
- Analyzing the effect of pore solution speciation and liquid confinement on the solid-liquid phase transition
- Evaluating concrete compatibility for the construction of LNG tanks

### **8.1 Identifying deleterious aggregates susceptible to frost damage**

A poromechanical model was developed that can predict stress and strain distributions (and thus ostensibly damage likelihood) in concrete incorporating aggregates with undesirable combinations of geometry and constitutive properties while the concrete is cooled below freezing. Based on the results of the model simulations, the most important findings of this study are:

- High-porosity, low-permeability aggregates with fine pore structure are the most vulnerable to D-cracking in concrete. High tensile stress is generated in the aggregate near the aggregate-matrix interface and made more severe by over-pressurization caused by the Mandel-Cryer effect.
- High-porosity, high-permeability (e.g., lightweight) aggregates are beneficial for reducing tensile stress in freezing concrete.
- A high-porosity, low-permeability matrix with fine pore structure may reduce concrete resistance to freezing temperatures by increasing the strain differential and resulting tangential stress at the aggregate-matrix boundary.

- Reduction in aggregate size was found to be effective in quickly relaxing the tensile tangential stress, which would likely reduce the probability of D-cracking of concrete under freezing temperatures.
- Although air-entrainment reduces concrete expansion upon cooling, excessive thermal contraction of the matrix compared to the aggregate may generate tensile stress in the matrix, and create cracks over successive freeze-thaw cycles.
- Difference between CTEs of coarse aggregate and matrix in which they are embedded should not be too high since it may cause tensile stress at the aggregate boundary or ITZ.
- Increase in cooling rate likely leads to increased cracking propensity through the reduction in time available to relax pore pressure buildup and the related tangential stresses in the aggregate and matrix.

The model developed in this work predicts the transient stress and strain fields within concrete containing substandard aggregates exposed to freezing conditions. All the aforementioned results confirm with experimental findings previously done in this area. Such affirmation of the simulated results gives confidence to the model, and hence this model can be used as a tool to provide optimum concrete mixture design facilitating the use of substandard aggregates that would otherwise be deemed as waste materials. It is expected that consideration of the model results will help with selecting appropriate materials, which in turn will improve the durability of concrete infrastructure. The model is appropriate for saturated air-entrained and non-air-entrained concrete, and therefore may over predict the stress in real concrete infrastructure because concrete is seldom in

fully saturated condition. The model likewise does not account for viscoelastic relaxation, which would reduce the stresses from that predicted by the model. On the other hand, it was shown that the reduction in permeability with temperature owing to ice blocking pores results in higher stresses and higher rate of stress increase. As this effect was not accounted for in the sensitivity analysis, the actual peak stresses may be greater than those predicted by the model. It is also expected that the pore blocking due to ice penetration may be offset by microcracking initiated by the successive freeze thaw cycles, and therefore may lead to much more complicated permeability functions than the existing simplistic models. In order to accurately predict the change in permeability due to pore blocking and microcracking, better models relating effective pore size distribution and microcracking induced macropores to intrinsic permeability must first be developed.

## **8.2 Determining optimum air void spacing specific to a concrete mixture design and environmental exposure**

Most previous research dealing with the frost damage of concrete pavements studied the role of air void parameters in protecting the cement paste or mortar matrix while neglecting the conjoint effects of the aggregate and mortar characteristics, rate of cooling and the minimum temperature reached on the damage propensity. A poromechanical model is used to demonstrate the significance of concrete constituent properties and climate conditions on the requirement of the air void spacing factor for concrete exposed to freezing temperatures. The following conclusions are drawn from

the model-predicted pore liquid pressure, stress, and strain distributions of the various mixture designs evaluated:

- Requirement of maximum spacing factor depends on the concrete constituent properties, rate of cooling, and the minimum temperature reached and thus is specific to a specific concrete mixture design and the climatic region to which concrete pavement is exposed. This maximum spacing value can range from a fraction of a millimeter to several millimeters depending on the mixture design and environmental exposure.
- Reduction in the interconnected porosity by reducing volume fraction of coarse pores of mortar achieved with low w/c or addition of SCMs may increase the maximum spacing factor requirement. However, too much SCM may hamper the concrete durability by reducing the pore sizes drastically, yielding high crystallization pressure.
- Concrete containing high-porosity, high-permeability aggregates (typical of lightweight aggregates) may perform satisfactorily with or without entrained air for low amplitude freeze-thaw cycles, which is typical of Texas weather. Such concrete, if exposed to harsh winters with very low temperatures (for instance, if used for paving highways in Minnesota) requires entrained air with the lowest maximum spacing factor to reduce the tensile tangential stress developed in the aggregate center.

The model utilized here takes into account the concrete constituent properties, air void spacing factor, the lowest temperature to which pavement is exposed, and cooling

rate to predict damage initiating tensile stresses in concrete during freezing. Hence, the model can specify the optimum air void spacing factor for any given concrete mixture design depending on the geographic location of the construction site. It is apparent that use of this model in building durable pavement will help practitioners control multiple factors including selection and proportion of concrete mixture components instead of regulating one single parameter, the air content. Since this model does not account for the time dependent behavior of materials, specifically the effect of ice blocking and damage accretion on permeability, the model may under/over predict the peak value of tangential stresses without altering the projection trend. We assume that modeled results represent the fully reacted concrete microstructure such that evolution of pore properties (pore size and permeability) and air void system parameters with age due to the hydration and pozzolanic reactions can be reasonably ignored. The model also hypothesizes that there is minimal effect of chemical, autogenous, and drying shrinkage on the shrinking of spacing factor to maintain its simplistic nature. Despite the inherent limitations and assumptions of the modelling approach, we believe, if the model utilized in this work were implemented as a design tool, concrete could be designed more efficiently for freeze/thaw damage protection, thus improving concrete sustainability by reduced cement usage, admixture usage, and enhanced durability.

### **8.3 Analyzing the effect of pore solution speciation and liquid confinement on the solid-liquid phase transition**

The solid-liquid thermodynamic equilibrium relationship has been redeveloped to include the energy term associated with pore fluid shear stresses capable of

developing in the nanoconfined liquid that separates ice crystals from the pore walls in freezing, porous media. Furthermore, the effect of the pore solution speciation on pore water chemical potential was simultaneously considered. The following conclusions are drawn from the model simulations and analysis:

- The presence of dissolved species suppresses the freezing temperature of the pore solution. The higher the concentration of the solute, the greater the suppression of the freezing point.
- The magnitude of the damage-inducing pore pressure and expansion depends on the salt concentration, material properties, pore characteristics, and the minimum temperature attained. Depending on the lowest temperature and pore characteristics, an optimum salt concentration can be attained that can cause the most damaging strain.
- We have shown that, thermodynamically, it is favorable for disjoining pressure to promote ice propagation. An upper bound was obtained for liquid pressure and strain in a freezing porous body.
- Poroelasticity can demonstrate why the destructive expansion and hydraulic pore pressure develop in concrete even when the freezing point is suppressed by the dissolved ions. This expansion is due to the fact that when ice forms, more solvent is removed from the solution causing an increase in the solute concentration which in turn enhances density differences between the pore solution and the pure ice crystals.

- Accuracy of the simulated results is highly dependent on the accurate measurement of the properties, e.g. liquid saturation, pore size distribution, molar properties of the pore solution and crystals.

#### **8.4 Evaluating concrete compatibility for the construction of LNG tanks**

The theory of partially saturated concrete is proposed to elucidate deformation, stress, and pore pressure in concrete whose internal walls are pressurized by vapor, water, and ice crystals simultaneously. In addition, the theory of saturated freezing concrete presented by Coussy [1] is applied to simulate the effect of complete saturation during cooling to cryogenic temperatures. A thermo-poro-elastic model comprising energy balance, mass balance, and linear momentum balance has been presented for a freezing porous media. As an example solution scheme, appropriate boundary conditions pertaining to a concrete containment tank serving as primary containment to LNG are applied to demonstrate temperature gradient, liquid saturation, pore pressure, stress, and strain distribution associated with cryogenic temperatures. From the analysis, it has been revealed that

- High hydraulic pressure can be developed in the concrete wall if non-air-entrained concrete is used. This high pressure suppresses in-pore crystallization and causes expansion making concrete vulnerable to compressive failure. The magnitude of the hydraulic pore pressure depends on the pore properties such as porosity, permeability, and pore size distribution.

- Air-entrainment can relieve the hydraulic pore pressure caused by the volume expansion of the pore liquid during phase transition. Consequently, air-entrained concrete contracts with a continuous drop in temperature.
- Air-entrained concrete ultimately shows less contraction than the high-porosity, non-air-entrained concrete, and thus exhibits less stress than the high-porosity, non-air-entrained concrete.
- High cooling rate can escalate pore pressure build up by reducing time for the expelled water to escape from the freezing site increasing expansion and the subsequent compressive stress in the direction transverse to the wall thickness.
- Reducing moisture content by drying helps alleviate the pore pressure, but may not prove as efficient as the air-entrained concrete.

It is believed that the proposed model can be applied to tailor concrete mixture design towards successful construction of primary concrete LNG containment wall with minimal deformation and crack initiating internal stresses. Simulated results imply that air-entrainment can favorably be used to mitigate compressive failure by relieving the high pore pressure exerted by the high porosity concrete along with high cooling rate. Likewise, low porosity concrete that can be attained by adopting low water cement ratio, adding supplementary cementitious materials, and/or using low porosity aggregate (such as trap rock), can also prove beneficial in reducing the ultimate movement of the primary containment wall upon cryogenic cooling.

While the modeled strain results obtained from this study are in qualitative agreement with the experimental data published in the literature, experimental validation

must be carried out to investigate the effect of excess pressure in the supercooled liquid film that wraps around the solid crystals on the deformation of porous solid, especially when cooled to cryogenic temperatures. The effect of microcracking on permeability and viscoelastic stress relaxation should also be incorporated to accurately predict tensile stresses developed at very low temperatures. Other limitations associated with this model include use of constant material properties and highly simplified energy balance equation for heat transfer. This model can be further improved to include the presence of dissolved salts in pore liquid and its effect on the concrete deformation subjected to cryogenic cooling. Furthermore, if the temperature was dropped below  $-200^{\circ}\text{C}$ , change in air pressure (assumed atmospheric in this study) due to the liquefaction of nitrogen gas present in the air would need to be considered in the analysis. This theory does not account for the effect of the air bubble size on the deformation of air-entrained concrete and assumes that the air bubbles can accommodate indefinite growth of crystal. However, this limitation can be reasonably overlooked [42], as the air void spacing is established to be the most important air void system parameter [2, 7] regarding the frost resistance of concrete.

## REFERENCES

1. Coussy, O., *Poromechanics of freezing materials*. Journal of the Mechanics and Physics of Solids, 2005. **53**(8): p. 1689-718.
2. Powers, T.C. and T.F. Willis. *The air requirement of frost-resistant concrete*. in *Proceedings of the Highway Research Board*. 1949. Washington, D.C.: Highway Research Board.
3. Powers, T.C. and R.A. Helmuth. *Theory of volume changes in hardened Portland cement paste during freezing*. in *Proceedings of the Thirty-Second Annual Meeting of the Highway Research Board*. 1953. Washington, D.C.: Highway Research Board.
4. Powers, T.C., *Void spacing as a basis for producing air entrained concrete*. Journal of the American Concrete Institute, 1954. **26**: p. 7601-2.
5. Litvan, G.G. *The mechanism of frost action in concrete-theory and practical implications*. in *Proceedings of Workshop on Low Temperature Effects on Concrete*. 1988. Sapporo, Hokkaido, Japan: National Research Council Canada.
6. Michel Piaeon. Jacaues, P., ost, and S. Jean-Marc, *Freeze-thaw durability versus freezing rates*. Journal Proceedings, 1985. **82**(5): p. 684-692.
7. Pigeon, M., J. Marchand, and R. Pleau, *Frost resistant concrete*. Construction and Building Materials, 1996. **10**(5): p. 339-348.
8. Powers, T.C., *Working hypothesis for further studies of frost resistance of concrete*. Journal of the American Concrete Institute, 1945. **16**: p. 245-272.
9. Klieger, P. *Effect of entrained air on strength and durability of concrete made with various maximum sizes of aggregate*. in *Proceedings of the Thirty-First Annual Meeting of the Highway Research Board*. 1952. Washington, D.C.: Highway Research Board.
10. Paul, K. *Further studies on the effect of entrained air on strength and durability of concrete with various sizes of aggregates*. in *Concrete International*. 1955. Research and Development Laboratory, Portland Cement Association.
11. Verbeck, G. and R. Landgren. *Influence of physical characteristics of aggregates on frost resistance of concrete*. in *Proceedings of American Society for Testing Materials*. 1960. Conshohocken, Philadelphia: American Society for Testing and Materials.

12. Kaneuji, M., D.N. Winslow, and W.L. Dolch, *The relationship between an aggregate's pore size distribution and its freeze thaw durability in concrete*. Cement and Concrete Research, 1980. **10**(3): p. 433-441.
13. Mehta, P.K. and P.J.M. Monteiro, *Concrete: microstructure, properties, and materials*. 2006, New York: McGraw-Hill.
14. Stark, D. *Characteristics and utilization of coarse aggregates associated with d-cracking*. in *Research and Development Bulletin*. 1976. Portland Cement Association.
15. Scherer, G.W., *Crystallization in Pores*. Cement and Concrete Research, 1999. **29**(8): p. 1347-1358.
16. Scherer, G.W. and J.J. Valenza, *Mechanisms of frost damage*. Materials Science of Concrete, 2005. **7**: p. 209-246.
17. Stark, D. and P. Klieger. *Effect of maximum size of coarse aggregate on d-cracking in concrete pavements*. in *52nd Annual Meeting of the Highway Research Board*. 1973. Washington, D.C. .
18. Alexander, M. and S. Mindess, *Aggregates in concrete*. 2005, New York Taylor & Francis.
19. Callan, E.J. *Thermal expansion of aggregates and concrete durability*. in *ACI Journal Proceedings*. 1952. ACI.
20. Mindess, S., J.F. Young, and D. Darwin, *Concrete*. 2003, New Jersey: Prentice Hall.
21. Pigeon, M. and R. Pleau, *Durability of concrete in cold climates*. 1995, Suffolk: E&FN Spon.
22. Farnam, Y., et al., *Acoustic Emission and Low-Temperature Calorimetry Study of Freeze and Thaw Behavior in Cementitious Materials Exposed to Sodium Chloride Salt*. Transportation Research Record, 2014. **2441**: p. 81-90.
23. Sutter, L., et al., *Petrographic evidence of calcium oxychloride formation in mortars exposed to magnesium chloride solution*. Cement and Concrete Research, 2006. **36**: p. 1533-1541.
24. Valenza, J.J. and G.W. Scherer, *Mechanism for Salt Scaling*. Journal of the American Ceramic Society, 2006. **89**(4): p. 1161-1179.

25. Valenza II, J.J. and G.W. Scherer, *A review of salt scaling: II. Mechanisms*. Cement and Concrete Research, 2007. **37**(7): p. 1022-1034.
26. Liu, Z., et al., *Cryogenic Suction-A Major Salt Scaling Mechanism in Highway Concrete*, in *10th International Conference on Concrete Pavements*. 2012: Québec City Québec, Canada. p. 891-900.
27. Kang, Y., W. Hansen, and C. Borgnakke, *Effect of air-void system on frost expansion of highway concrete exposed to deicer salt*. International Journal of Pavement Engineering, 2012. **13**(3): p. 259-266.
28. Flatt, R.J., *Salt damage in porous materials: how high supersaturations are generated*. Journal of Crystal Growth, 2002. **242**(3-4): p. 435-454.
29. Chan, D.Y.C. and R.G. Horn, *The drainage of thin liquid films between solid surfaces*. The Journal of Chemical Physics, 1985. **83**(10): p. 5311-5324.
30. Israelachvili, J.N., P.M. McGuiggan, and A.M. Homola, *Dynamic Properties of Molecularly Thin Liquid Films*. Science, 1988. **240**(4849): p. 189-191.
31. Gee, M.L., et al., *Liquid to solidlike transitions of molecularly thin films under shear*. The Journal of Chemical Physics, 1990. **93**(3): p. 1895-1906.
32. Korb, J.P., et al., *Comparison of proton field-cycling relaxometry and molecular dynamics simulations for proton-water surface dynamics in cement-based materials*. Cement and Concrete Research, 2007. **37**(3): p. 348-350.
33. Xu, S., et al., *Transport of Water in Small Pores*. Langmuir, 2009. **25**(9): p. 5084-5090.
34. Biot, M.A., *Theory of Propagation of Elastic Waves in a Fluid-Saturated Porous Solid. I. Low-Frequency Range*. Journal of the Acoustical Society of America, 1956. **28**(2): p. 168-178.
35. Coussy, O., *Poromechanics*. 2004, West Sussex: John Wiley & Sons, Ltd.
36. Grasley, Z.C., et al., *Dynamic Pressurization Method for Measuring Permeability and Modulus: II. Cementitious Materials*. Materials and Structures, 2006. **40**(7): p. 711-721.
37. Jones, C.A. and Z.C. Grasley, *Correlation of Hollow and Solid Cylinder Dynamic Pressurization Tests for Measuring Permeability*. Cement and Concrete Research, 2009. **39**(4): p. 345-352.

38. Scherer, G.W., *Characterization of saturated porous bodies*. 2004. **37**(February): p. 21-30.
39. Scherer, G.W., *Poromechanics Analysis of a Flow-Through Permeameter with Entrapped Air*. Cement and Concrete Research, 2008. **38**(3): p. 368-378.
40. Scherer, G.W., *Thermal Expansion Kinetics: Method to Measure Permeability of Cementitious Materials: I. Theory*. Journal of the American Ceramic Society, 2000. **83**(11): p. 2753-2761.
41. Coussy, O. and P.J.M. Monteiro, *Poroelastic model for concrete exposed to freezing temperatures*. Cement and Concrete Research, 2008. **38**(1): p. 40-48.
42. Coussy, O. and P. Monteiro, *Unsaturated poroelasticity for crystallization in pores*. Computers and Geotechnics, 2007. **34**(4): p. 279-290.
43. Zuber, B. and J. Marchand, *Predicting the Volume Instability of Hydrated Cement Systems upon Freezing Using Poro-Mechanics and Local Phase Equilibria*. Materials and Structures, 2004. **37**(4): p. 257-270.
44. Grasley, Z.C. and K.R. Rajagopal, *Revisiting total, matric, and osmotic suction in partially saturated geomaterials*. Zeitschrift für angewandte Mathematik und Physik, 2011. **63**(2): p. 373-394.
45. Koubaa, A., M.B. Snyder, and K.R. Peterson, *Mitigating Concrete Aggregate Problems in Minnesota*. 1997, Minnesota Department of Transportation, Research Services Section: St. Paul, MN.
46. Thompson, S.R., M.P.J. Olsen, and B.J. Dempsey, *D-cracking in Portland Cement Concrete Pavements*. 1980, Urbana, IL: Illinois Department of Transportation.
47. Wang, K., et al., *Microscopic study of ice propagation in concrete*. ACI Materials Journal, 1996. **93**(4): p. 370-377.
48. Li, S., et al., *Quantitative damage evaluation of concrete suffered freezing-thawing by DIP technique*. Construction and Building Materials, 2014. **69**: p. 177-185.
49. Tanesi, J. and R. Meininger, *Freeze-thaw resistance of concrete with marginal air content*. 2006, FHWA Turner-Fairbank Highway Research Center.
50. Philleo, R.E., *Frost susceptibility of high-strength concrete*. Special Publication, 1987. **100**.

51. Aïtcin, P.C. *The influence of the spacing factor on the freeze-thaw durability of high-performance concrete*. in *International Symposium on High-Performance and Reactive Powder Concretes*. 1998. Sherbrooke (Quebec) Canada: University of Sherbrooke.
52. Pigeon, M., et al., *Freezing and thawing tests of high-strength concretes*. Cement and Concrete Research, 1991. **21**(5): p. 844-852.
53. Pigeon, M., et al., *Frost resistance of high-performance concrete [La durabilité au gel des bétons à haute performance]*. Canadian Journal of Civil Engineering, 1992. **19**(6): p. 975-980.
54. Li, Y., B.W. Langan, and M.A. Ward. *Freezing and thawing: comparison between non air-entrained and air-entrained high-strength concrete*. in *ACI International Conference High-Performance Concrete*. 1994. ACI Special Publication SP-149.
55. Pinto, R.C.A. and K.C. Hover, *Frost and scaling resistance of high-strength concrete*. RD122. 2001, Skokie, Illinois: Portland Cement Association. 75.
56. Micah Hale, W., S.F. Freyne, and B.W. Russell, *Examining the frost resistance of high performance concrete*. Construction and Building Materials, 2009. **23**(2): p. 878-888.
57. Beaudoin, J.J. and C. MacInnis, *The mechanism of frost damage in hardened cement paste*. Cement and Concrete Research, 1974. **4**(2): p. 139-147.
58. Kaneuji, M., D.N. Winslow, and W.L. Dolch, *The relationship between an aggregate's pore size distribution and its freeze thaw in concrete*. Cement and Concrete Composites, 1980. **10**: p. 433-441.
59. Scherer, G.W., *Freezing gels*. Journal of Non-Crystalline Solids, 1993. **155**(1): p. 1-25.
60. Krstulovic-Opara, N., *Liquefied natural gas storage: Material behavior of concrete at cryogenic temperatures*. ACI Materials Journal, 2007. **104**(3): p. 297-306.
61. Kogbara, R.B., et al., *A review of concrete properties at cryogenic temperatures: Towards direct LNG containment*. Construction and Building Materials, 2013. **47**: p. 760-770.
62. Rostásy, F.S., U. Schneider, and G. Wiedemann, *Behaviour of mortar and concrete at extremely low temperatures*. Cement and Concrete Research, 1979. **9**(3): p. 365-376.

63. Planas, J., et al., *Thermal deformation of loaded concrete during thermal cycles from 20 °C to -165 °C*. Cement and Concrete Research, 1984. **14**: p. 639-644.
64. Corres, H., M. Elices, and J. Planas, *Thermal deformation of loaded concrete at low temperatures. 3: Lightweight concrete*. Cement and Concrete Composites, 1986. **16**: p. 845-852.
65. Elices, M., J. Planas, and H. Corres, *Thermal deformation of loaded concrete at low temperatures, 2: Transverse deformation*. Cement and Concrete Research, 1986. **16**: p. 741-748.
66. Rostásy, F.S. and U. Pusch, *Strength and deformation of lightweight concrete of variable moisture content at very low temperatures*. International Journal of Cement Composites and Lightweight Concrete, 1987. **9**(1): p. 3-17.
67. Miura, T., *Properties of concrete at very low temperatures*. Materials and Structures, 1989. **22**(130): p. 243-254.
68. Marshall, A.L., *Cryogenic concrete*. Cryogenics, 1982. **22**(11): p. 555-565.
69. v.d. Veen, C., *Properties of concrete at very low temperatures: A survey of the literature*. 1987, Delft University of Technology.
70. Tognon, G., *Behaviour of mortars and concrete in the temperature range from +20 °C to -196 °C*, in *Fifth International Symposium on the Chemistry of Cement*. 1968: Tokyo. p. 229-249.
71. Kogbara, R.B., et al., *Relating damage evolution of concrete cooled to cryogenic temperatures to permeability*. Cryogenics, 2014. **64**: p. 21-28.
72. Setzer, M.J., *Einfluss des Wassergehaltes auf die Eigenschaften des erhärteten Betons*. Deutscher Ausschuss für Stahlbeton, 1977. **280**: p. 103-103.
73. v.d. Veen, C., *Theoretical and experimental determination of the crack width in reinforced concrete at very low temperatures*. 1990, Delft University of Technology.
74. Hjortset, K., et al., *Development of Large-Scale Precast, Prestressed Concrete Liquefied Natural Gas Storage Tanks*. Precast/Prestressed Concrete Institute, 2013. **58**(4): p. 40-54.
75. Wiedemann, G., *Zum Einfluss tiefer Temperaturen auf Festigkeit und Verformung von Beton*. 1982: Institut für Baustoffe, Massivbau und Brandschutz der Technischen Universität Braunschweig.

76. Coussy, O., *Deformation and stress from in-pore drying-induced crystallization of salt*. Journal of the Mechanics and Physics of Solids, 2006. **54**(8): p. 1517-1547.
77. Coussy, O., *Mechanics and Physics of Porous Solids*. 2010, West Sussex: John Wiley & Sons, Ltd.
78. Pitzer, K.S. and G. Mayorga, *Thermodynamics of electrolytes. II. Activity and osmotic coefficients for strong electrolytes with one or both ions univalent*. The Journal of Physical Chemistry, 1973. **77**(19): p. 2300-2308.
79. Pitzer, K.S. and J.J. Kim, *Thermodynamics of electrolytes. IV. Activity and osmotic coefficients for mixed electrolytes*. Journal of the American Chemical Society, 1974. **96**(18): p. 5701-5707.
80. Grasley, Z.C. and C.K. Leung, *Desiccation shrinkage of cementitious materials as an aging, poroviscoelastic response*. Cement and Concrete Research, 2011. **41**(1): p. 77-89.
81. McTigue, D.F., *Thermoelastic response of fluid-saturated porous rock*. Journal of Geophysical Research, 1986. **91**(B9): p. 9533-9542.
82. Timoshenko, S. and J.N. Goodier, *Theory of Elasticity*. 1951, New York: McGraw-Hill. 416-420.
83. van Genuchten, M.T., *A closed-form equation for predicting the hydraulic conductivity of unsaturated soils*. Soil Science Society of America Journal, 1980. **44**(5): p. 892-898.
84. Stehfest, H., *Numerical Inversion of Laplace Transforms*. Communications of the ACM, 1970. **13**: p. 47-49 and 624.
85. Mallet, A., *Numerical Inversion of Laplace Transform*. 2000.
86. Coussy, O. and P.J.M. Monteiro, *Errata to "Poroelastic model for concrete exposed to freezing temperatures" [Cement and Concrete Research 38 (2008) 40-48]*. Cement and Concrete Research, 2009. **39**(4): p. 371-372.
87. Crank, J. and P. Nicolson, *A Practical Method for Numerical Evaluation of Solutions of Partial Differential Equations of the Heat-Conduction Type*. Mathematical Proceedings of the Cambridge Philosophical Society, 1947. **43**(01): p. 50-67.
88. Carman, P.C., *Fluid flow through granular beds*. Transactions-Intitution of Chemical Engineers, 1937. **15**: p. 150-166.

89. Brutsaert, W., *Some Methods of Calculating Unsaturated Permeability*. Transactions of American Society of Agricultural Engineers, 1967. **10**: p. 400-404.
90. Marshall, T.J., *A Relation between Permeability and Size Distribution of Pores*. Journal of Soil Science, 1958. **9**(1): p. 1-8.
91. Berryman, J. and S. Blair, *Kozeny-Carman Relations and Image Processing Methods for Estimating Darcy's Constant*. Journal of Applied Physics, 1987. **62**(6): p. 2221-2228.
92. Valdes-Parada, F.J., J.A. Ochoa-Tapia, and J. Alvarez-Ramirez, *Validity of the permeability Carman–Kozeny equation: A volume averaging approach*. Physica A: Statistical Mechanics and its Applications, 2009. **388**(6): p. 789-798.
93. Mualem, Y., *A New Model for Predicting the Hydraulic Conductivity of Unsaturated Porous Media*. Water Resources Research, 1976. **12**(3): p. 513-522.
94. Luckner, L., M.T. van Genuchten, and D.R. Nielsen, *A Consistent Set of Parametric Models for the Two-Phase Flow of Immiscible Fluids in the Subsurface*. Water Resources Research, 1989. **25**(10): p. 2187-2193.
95. Vogel, T. and M. Cislerova, *On the reliability of unsaturated hydraulic conductivity calculated from the moisture retention curve*. Transport in Porous Media, 1988. **3**(1): p. 1-15.
96. Ippisch, O., H.J. Vogel, and P. Bastian, *Validity limits for the van Genuchten–Mualem model and implications for parameter estimation and numerical simulation*. Advances in Water Resources, 2006. **29**(12): p. 1780-1789.
97. Chiu, T.-F. and C. Shackelford, *Unsaturated Hydraulic Conductivity of Compacted Sand-Kaolin Mixtures*. Journal of Geotechnical and Geoenvironmental Engineering, 1998. **124**(2): p. 160-170.
98. Powers, T.C., *Structure and Physical Properties of Hardened Portland Cement Paste*. Journal of the American Ceramic Society, 1958. **41**(1): p. 1-6.
99. Christensen, B.J., T.O. Mason, and H.M. Jennings, *Comparison of Measured and Calculated Permeabilities for Hardened Cement Pastes*. Cement and Concrete Composites, 1996. **26**(9): p. 1325-1334.
100. Abell, A., K. Willis, and D.A. Lange, *Mercury Intrusion Porosimetry and Image Analysis of Cement-Based Materials*. Journal of colloid and interface science, 1999. **211**(1): p. 39-44.

101. Grasley, Z.C. and D.A. Lange, *Constitutive Modeling of the Aging Aisocoelastic Properties of Portland Cement Paste*. *Mechanics of Time-Dependent Materials*, 2007. **11**(3-4): p. 175-198.
102. Cruz, C.R. and M. Gilien, *Thermal Expansion of Portland Cement Paste, Mortar and Concrete at High Temperatures*. *Fire and Materials*, 1980. **4**(2): p. 66-70.
103. Vichit-Vadakan, W. and G.W. Scherer, *Measuring Permeability of Rigid Materials by a Beam-Bending Method: III, Cement Paste*. *Journal of the American Ceramic Society*, 2002. **85**(6): p. 1537-1544.
104. Wang, H., *Theory of linear poroelasticity with applications to geomechanics and hydrogeology*. 2000, New Jersey: Princeton University Press.
105. Janssen, D.J., et al., *Predicting the Progression of D-Cracking*. 1986, Illinois Department of Transportation.
106. Chaplin, M., *Water Structure and Science*. 2012, Available at: <http://www.lsbu.ac.uk/water/anmlies.html>, Last accessed on Nov.
107. Janssen, D. and M. Snyder, *Resistance of concrete to freezing and thawing, SHRP-C-391*. 1994, Strategic Highway Research Program, National Research Council: Washington, DC.
108. Clarke, J.L., *Structural Lightweight Aggregate Concrete*. 1993, Glasgow: Blackie Academic & Professional, an imprint of Chapman & Hall. 19-19.
109. Neville, A.M. and J.J. Brooks, *Concrete Technology*. second ed ed. 2010, Essex, England: Pearson Education Limited.
110. Jackson, K.A. and B. Chalmers, *Freezing of Liquids in Porous Media with Special Reference to Frost Heave in Soils*. *Journal of Applied Physics*, 1958. **29**(8): p. 1178-1181.
111. Krstulovic-opara, N., *Liquefied Natural Gas Storage : Material Behavior of Concrete at Cryogenic Temperatures*. *ACI Materials Journal*, 2007. **104**(3): p. 297-306.
112. Pigeon, M., J. Prevost, and J. Simard, *Freeze-Thaw Durability Versus Freezing Rate*. *ACI Materials Journal*, 1985: p. 684-692.
113. Johannesson, B., *Dimensional and ice content changes of hardened concrete at different freezing and thawing temperatures*. *Cement and Concrete Composites*, 2010. **32**(1): p. 73-83.

114. Grasley, Z. and D. Lange, *Thermal dilation and internal relative humidity of hardened cement paste*. Materials and Structures, 2007. **40**(3): p. 311-317.
115. Ozyildirim, C. *Durability of structural lightweight concrete*. in *Concrete Bridge Conference*. 2008. St. Louis, MO.
116. Mao, J., et al., *Experimental study on freeze-thaw damage mechanism of lightweight aggregate concrete*. Journal of ASTM International, 2009. **7**(1): p. 103-118.
117. Sabir, B.B. and K. Kouyiali, *Freeze-thaw durability of air-entrained CSF concrete*. Cement and Concrete Composites, 1991. **13**(3): p. 203-208.
118. Hoyle, K., et al. *Composite Concrete Cryogenic Tank (C3T): A Precast Concrete Alternative for LNG Storage*. in *The 17th International Conference & Exhibition on Liquefied Natural Gas*. 2013. Houston, TX.
119. Kralj, B. and G.N. Pande, *A stochastic model for the permeability characteristics of saturated cemented porous media undergoing freezing*. Transport in Porous Media, 1996. **22**(3): p. 345-357.
120. Couture, F., W. Jomaa, and J.R. Puiggali, *Relative permeability relations: A key factor for a drying model*. Transport in Porous Media, 1996. **23**(3): p. 303-335.
121. Baroghel-Bouny, V., et al., *Characterization and identification of equilibrium and transfer moisture properties for ordinary and high-performance cementitious materials*. Cement and Concrete Research, 1999. **29**(8): p. 1225-1238.
122. Crank, J. and P. Nicolson, *A practical method for numerical evaluation of solutions of partial differential equations of the heat-conduction type*. Advances in Computational Mathematics, 1996. **6**(1): p. 207-226.
123. Sun, Z. and G.W. Scherer, *Effect of air voids on salt scaling and internal freezing*. Cement and Concrete Research, 2010. **40**(2): p. 260-270.
124. Brun, M., et al., *A new method for the simultaneous determination of the size and shape of pores: the thermoporometry*. Thermochimica Acta, 1977. **21**(1): p. 59-88.
125. Cahn, J.W., J.G. Dash, and F. Haiying, *Theory of ice premelting in monosized powders*. Journal of Crystal Growth, 1992. **123**: p. 101-108.

126. Rempel, A.W., J.S. Wettlaufer, and M.G. Worster, *Premelting dynamics in a continuum model of frost heave*. Journal of Fluid Mechanics, 2004. **498**: p. 227-244.
127. Dash, J., A. Rempel, and J. Wettlaufer, *The physics of premelted ice and its geophysical consequences*. Reviews of Modern Physics, 2006. **78**(3): p. 695-741.
128. Wettlaufer, J. and M. Worster, *Dynamics of premelted films: Frost heave in a capillary*. Physical Review E, 1995. **51**(5): p. 4679-4689.
129. Farnam, Y., et al., *Measuring Freeze and Thaw Damage in Mortars Containing Deicing Salt Using a Low-Temperature Longitudinal Guarded Comparative Calorimeter and Acoustic Emission*. Advances in Civil Engineering Materials, 2014. **3**(1): p. 1-22.
130. Li, T.-D. and E. Riedo, *Nonlinear Viscoelastic Dynamics of Nanoconfined Wetting Liquids*. Physical Review Letters, 2008. **100**(10): p. 106102.
131. Fagerlund, G., *Determination of pore-size distribution from freezing-point depression*. Materials & Structures, 1973: p. 215-225.
132. Zeng, Q., T. Fen-Chong, and K. Li, *Freezing behavior of cement pastes saturated with NaCl solution*. Construction and Building Materials, 2014. **59**: p. 99-110.
133. Diamond, S., *Review: Mercury porosimetry. An inappropriate method for the measurement of pore size distributions in cement-based materials*. Cement and Concrete Research, 2000. **30**: p. 1517-1525.
134. Dormieux, L., A. Molinari, and D. Kondo, *Micromechanical approach to the behavior of poroelastic materials*. Journal of the Mechanics and Physics of Solids, 2002. **50**(10): p. 2203-2231.

## APPENDIX A

Coefficients  $A$ ,  $C$ ,  $U$ ,  $V$ ,  $W$ ,  $X$ , and  $Z$  are given by

$$A = Z \left( M^{a-L} (K^a + b^a b^{a-c} M^{a-c} \beta^a) \rho^c + M^{a-c} (K^a + b^a b^{a-L} M^{a-L} \beta^a) \rho^L \right), \quad (\text{A1})$$

$$C = Z \left( M^{p-L} (K^p + b^p b^{p-c} M^{p-c} \beta^p) \rho^c + M^{p-c} (K^p + b^p b^{p-L} M^{p-L} \beta^p) \rho^L \right), \quad (\text{A2})$$

$$U = \frac{2K^a R_i^3 (3\beta^a + 2\lambda^a) \chi^p}{Z}, \quad (\text{A3})$$

$$V = -\frac{2(K^a + 2K^p \chi^p) (R_i^3 - R_o^3) \varpi^p}{Z}, \quad (\text{A4})$$

$$W = -\frac{2K^p (R_i^3 - R_o^3) \lambda^p (1 + 2\chi^p)}{Z}, \quad (\text{A5})$$

$$X = \frac{2(3K^p (R_i^3 - R_o^3) \beta^a \chi^p + K^a \lambda^a (R_o^3 + 2R_i^3 \chi^p))}{Z}, \quad (\text{A6})$$

and

$$Z = K^a R_o^3 + 2 \left( (K^a - K^p) R_i^3 + K^p R_o^3 \right) \chi^p, \quad (\text{A7})$$

where

$$\beta = \frac{1+\nu}{3(1-\nu)}, \quad (\text{A8})$$

$$\chi = \frac{1-2\nu}{1+\nu}, \quad (\text{A9})$$

and

$$\lambda = \frac{1-2\nu}{1-\nu}. \quad (\text{A10})$$

## APPENDIX B

### Thermodynamics of partially saturated freezing concrete

The theory presented here is an application of the model proposed by Coussy [76] for isothermal drying induced crystallization, allowing for the thermal expansion induced by the temperature change. Let us consider a porous material whose pore space is occupied by three phases: a gas referred to by index  $J = G$ , a liquid referred to by index  $J = L$ , and a solid crystal referred to by index  $J = C$ . If  $dV_0$  is the initial volume of an infinitesimal representative element from the porous solid,  $\phi_0$  and  $\phi$  are the initial and current porosity, respectively, the reference porous volume of the element is given by  $\phi_0 dV_0$  and the current porous volume is  $\phi dV_0$ . The porous solid and any of its phases are capable of exhibiting infinitesimal deformation gradients. Furthermore,  $\phi^J$  if the current volume occupied by the phase  $J$ , the current overall porosity,  $\phi$  can be written as

$$\phi = \phi^C + \phi^G + \phi^L \quad (\text{B1})$$

If the current number of moles of phase  $J$  per unit initial volume is  $N^J$ , temperature  $T$ , the current molar entropy is  $s^J$ , and the current molar chemical potential  $\mu_J$ , the Gibbs-Duhem equality for each phase  $J$  can be written in the form

$$\phi^J dp^J - N^J s^J dT - N^J d\mu^J = 0 \quad (\text{B2})$$

such that

$$\begin{aligned}
\phi^G dp^G &= N^a s^a d\theta + n^a d\mu^a + N^v s^v d\theta + N^v d\mu^v, \\
\phi^C dp^C &= N^C s^C d\theta + N^C d\mu^C, \text{ and} \\
\phi^L dp^L &= N^L s^L d\theta + N^L d\mu^L.
\end{aligned} \tag{B3}$$

When no dissipation occurs, the first and second laws of thermodynamics combine to provide a Clausius-Duhem equality (for equilibrium) for a poroelastic material as given by

$$T_{ij} d\varepsilon_{ij} + \mu^C dN^C + \mu^a dN^a + \mu^v dN^v + \mu^L dN^L - \Sigma_M d\theta - dF = 0, \tag{B4}$$

where  $\sigma_{ij}$  is the current overall stress components,  $\varepsilon_{ij}$  is the current overall strain component,  $\Sigma_m$  is the entropy of the open element per unit of its initial volume, and  $F$  is the overall Helmholtz free energy. Superscripts  $a$  and  $v$  represent air and vapor, respectively.

Let  $F_{sk}$  and  $\Sigma_{sk}$  be the Helmholtz free energy and entropy per unit initial volume of the skeleton. The term skeleton includes interfaces between the solid matrix and the phases present in the pore network, and excludes the bulk phases in the pores. Due to the additive characteristics of free energy,  $F_{sk}$  and  $\Sigma_{sk}$  can be written as

$$\begin{aligned}
\Sigma_{sk} &= \Sigma - N^C s^C - N^a s^a - N^v s^v - N^L s^L \text{ and} \\
F_{sk} &= F - (N^C s^C - \phi^C p^C + N^v s^v + N^a s^a - \phi^G p^G + N^L s^L - \phi^L p^L).
\end{aligned} \tag{B5}$$

With the help of (B5), (B4) gives us the free energy balance related to the poroelastic skeleton as

$$T_{ij} d\varepsilon_{ij} + p^C d\phi^C + p^G d\phi^G + p^L d\phi^L - \Sigma_{sk} d\theta - dF_{sk} = 0. \tag{B6}$$

Therefore, the unsaturated poroelastic state equations can be written as

$$\begin{aligned}
F_{sk} &= F_{sk}(\varepsilon_{ij}, \phi^J, \theta), \\
T_{ij} &= \frac{\partial F_{sk}}{\partial \varepsilon_{ij}}, \\
p^J &= \frac{\partial F_{sk}}{\partial \phi^J}, \text{ and} \\
\Sigma_{sk} &= -\frac{\partial F_{sk}}{\partial \theta}.
\end{aligned} \tag{B7}$$

Change in partial porosities  $\phi^J$  results from the change in saturation,  $S^J$  and skeletal deformation,  $\varphi^J$  resulting from the action of pressure on phases,  $p_J$ . Therefore,

$\phi^J$  can be given in the form

$$\phi^J = \phi_0 S^J + \varphi^J \tag{B8}$$

with the constraint

$$S^C + S^G + S^L = 1. \tag{B9}$$

Therefore, the current overall porosity is

$$\phi = \phi_0 + \varphi^C + \varphi^G + \varphi^L. \tag{B10}$$

State equations (B7) account for both the energy required for skeletal deformation and energy required to create new interfaces. Using (B8) with (B7), these two energy variables are separated as

$$F_{sk}(\varepsilon_{ij}, \phi^J, \theta) = \psi_{sk}(\varepsilon_{ij}, \varphi^J, S^C, S^G, \theta). \tag{B11}$$

Substituting (B8) and (B11) into (B6) and applying the constraint (B9), we find

$$\begin{aligned}
T_{ij} d\varepsilon_{ij} + p^C d\varphi^C + p^G d\varphi^G + p^L d\varphi^L + \\
\phi_0 (p^C - p^L) dS^C + \phi_0 (p^G - p^L) dS^G - \Sigma_{sk} d\theta - d\psi_{sk} = 0,
\end{aligned} \tag{B12}$$

which leads to the following- equations

$$\begin{aligned}
T_{ij} &= \frac{\partial \psi_{sk}}{\partial \varepsilon_{ij}}, \\
p^J &= \frac{\partial \psi_{sk}}{\partial \varphi^J}, \\
\phi_0 (p^C - p^L) &= \frac{\partial \psi_{sk}}{\partial S^C}, \\
\phi_0 (p^G - p^L) &= \frac{\partial \psi_{sk}}{\partial S^G}, \text{ and} \\
\Sigma_{sk} &= -\frac{\partial \psi_{sk}}{\partial \theta}.
\end{aligned} \tag{B13}$$

$F_{sk}$  can be divided into two parts: elastic free energy,  $W$  of the porous solid excluding the interfaces, and the interface energy,  $U$  per unit of initial porous volume  $\phi_0 dV_0$ . Assuming that  $U$  does not significantly vary with the skeletal deformation for constant saturation  $S_j$ , we find

$$\psi_{sk} = p_0 \phi + W(\varepsilon_{ij}, \varphi^J, S^C, S^G, \theta) + \phi_0 U(S^C, S^G). \tag{B14}$$

Substituting (B14) into state equations (B13), we obtain

$$\begin{aligned}
T_{ij} &= \frac{\partial W}{\partial \varepsilon_{ij}}, \\
p^J - p_0 &= \frac{\partial W}{\partial \varphi^J}, \\
\phi_0 (p^C - p^L) &= \frac{\partial W}{\partial S^C} + \phi_0 \frac{\partial U}{\partial S^C}, \\
\phi_0 (p^G - p^L) &= \frac{\partial W}{\partial S^G} + \phi_0 \frac{\partial U}{\partial S^G}, \text{ and} \\
\Sigma_{sk} &= -\frac{\partial W}{\partial \theta}.
\end{aligned} \tag{B15}$$

Introducing the Legendre-Frenchel transform  $W^*$  of  $W$  with respect to  $\varphi^J$  such that

$$W^* = W - \sum_{J=C,G,L} (p^J - p_0) \phi^J \quad (\text{B16})$$

results in

$$\begin{aligned} T_{ij} &= \frac{\partial W^*}{\partial \varepsilon_{ij}}, \\ \phi^J &= - \frac{\partial W^*}{\partial (p^J - p_0)}, \text{ and} \\ \Sigma_{sk} &= - \frac{\partial W^*}{\partial \theta}. \end{aligned} \quad (\text{B17})$$

Equations (B17) are the generalized state equations of unsaturated thermoporoelasticity. For a linear, isotropic thermoporoelastic material

$$\begin{aligned} T_{ij} &= \left( K - \frac{2G}{3} \right) \varepsilon_{kk} \delta_{ij} + 2G \varepsilon_{ij} - 3\alpha_s K (\theta - \theta_0) \delta_{ij} \\ &\quad - b^C (p^C - p_0) \delta_{ij} - b^L (p^L - p_0) \delta_{ij} - b^G (p^G - p_0) \delta_{ij} \end{aligned} \quad (\text{B18})$$

and

$$\begin{aligned} \phi^C &= b^C \varepsilon_{kk} + \frac{p^C - p_0}{N_{CC}} + \frac{p^G - p_0}{N_{CG}} + \frac{p^L - p_0}{N_{CL}} - 3\varpi^C (\theta - \theta_0), \\ \phi^G &= b^G \varepsilon_{kk} + \frac{p^C - p_0}{N_{GC}} + \frac{p^G - p_0}{N_{GG}} + \frac{p^L - p_0}{N_{GL}} - 3\varpi^G (\theta - \theta_0), \text{ and} \\ \phi^L &= b^L \varepsilon_{kk} + \frac{p^C - p_0}{N_{LC}} + \frac{p^G - p_0}{N_{LG}} + \frac{p^L - p_0}{N_{LL}} - 3\varpi^L (\theta - \theta_0). \end{aligned} \quad (\text{B19})$$

Here,  $\varpi^J$  is the linear coefficient of thermal expansion of the pore volume occupied by the phase  $J$ , and  $N_{JK}$  is the generalized Biot coupling moduli, with  $N_{JK} = N_{KJ}$  owing to the Maxwell's symmetry relations, such that,

$$\sum_{K=C,G,L} \frac{1}{N_{JK}} = \frac{b^J - \phi_0 S^J}{K_s} \text{ and} \quad (\text{B20})$$

$$b = b^C + b^G + b^L = 1 - \frac{K}{K_s}. \quad (\text{B21})$$

Here a link between the macroscopic and the microscopic properties needs to be established to determine  $b^J$  separately. This link can be set based on the microporomechanics considerations presented by [134], and applied by [76]. As at any stage of the freezing process, the gaseous phase and the ice crystals occupy the largest pores, and the remaining smaller pores are still filled up by the liquid water, the crystal and gas filled pores can presumably act roughly the same as if they were enclosed in a porous body whose pore network was only constituted of liquid filled pores. Accordingly,

$$b^C + b^G = 1 - \frac{K}{K'_s}, \quad (\text{B22})$$

where  $K'$  is the bulk modulus of the newly defined porous body such that,

$$K'_s = \frac{4G_s K_s (1 - \phi'_0)}{3\phi'_0 K_s + 4G_s}. \quad (\text{B23})$$

The matrix bulk and shear moduli,  $K_s$  and  $G_s$  are intrinsic properties and do not depend on the properties of the pore network. The porosity  $\phi'_0$  of this porous solid is given by

$$\phi'_0 = \frac{\phi_0 S^L}{1 - \phi_0 (S^C + S^G)}. \quad (\text{B24})$$

Similarly, since the largest pores are occupied by the gas only, and the remaining smaller pores are filled with ice crystals and liquid water, it is therefore reasonable to assume that the wet air filled pores are embedded in a porous matrix whose porous

volume includes both the liquid filled pores and the ice filled pores. Accordingly, analogous to (B22) to (B24),

$$b^G = 1 - \frac{K}{K_s}, \quad (\text{B25})$$

where

$$K_s = \frac{4G_s K_s (1 - \phi_0'')}{3\phi_0'' K_s + 4G_s} \quad (\text{B26})$$

and

$$\phi_0'' = \frac{\phi_0 (S^C + S^L)}{1 - \phi_0 S^G}. \quad (\text{B27})$$